APERTURE SYNTHESIS OBSERVATIONS OF OH ABSORPTION IN THE GALACTIC CENTER

Thesis by

John Harold Bieging

In Partial Fulfillment of the Requirements

for the Degree of

Doctor of Philosophy

California Institute of Technology

Pasadena, California

1974

(Submitted December 17, 1973)

ACKNOWLEDGMENTS

The completion of this thesis was made possible by the generous assistance of many people, to whom I express my gratitude. Without naming them all, there are several individuals whose help to me deserves a special mention.

First, Gordon Stanley, Director of the Owens Valley Radio Observatory, provided both observing time and funds for computation in ample supply, and also support through a research assistantship.

Prof. Alan T. Moffet's careful reading of, and helpful comments on, major portions of the text are especially appreciated.

Dr. David Rogstad was a frequent source of advice on the problems of aperture synthesis.

My fellow graduate students were helpful in many ways. Seth Shostak gave sage advice on all aspects of this work. I am especially indebted to Eric Greisen for the use of computer programs for the Fourier inversion and cleaning process. Bill Wright, Kwong Chu, and Bob Kirshner helped out with expert observing assistance and useful discussions.

I am indebted to Dick Crutcher for the 100-channel autocorrelator observations of Sgr B2. Dick Read gave me a number of valuable suggestions about instrumental calibration. I thank Nick Scoville for providing results prior to publication.

The program could not have been done without the assistance of the staff of the OVRO.

The National Science Foundation provided financial support through a Graduate Fellowship.

Finally, I thank my adviser, Dr. George Seielstad, for initially suggesting this project and guiding me through to its completion.

This thesis is dedicated to my wife, Lou Ann, for her patience and understanding during those two- and three-week observing runs.

ABSTRACT

The galactic center radio sources Sgr A and Sgr B2 have been mapped, by an aperture synthesis technique, in the 1667 MHz absorption line of the OH molecule. The angular resolution of the maps is 3'.25, and the velocity resolution is 1.44 km s^{-1}. The range of velocities covered by the maps is from -200 to +100 km s^{-1} in the local standard of rest. The data are presented in two forms: (i) spectra of brightness temperature as a function of velocity, for fixed positions in right ascension and declination; and (ii) maps of the optical depth distribution in the spatial coordinates, for fixed velocity.

The deep absorption line at +40 km s^{-1} in Sgr A is produced by two separate components. Both components appear to be very massive, dense clouds undergoing rapid rotation about axes perpendicular to the galactic plane. If the clouds are gravitationally bound, then their total masses must exceed $4.6 \times 10^6 M_\odot$ and $2 \times 10^5 M_\odot$.

Fifteen discrete molecular clouds are seen in absorption against Sgr B2 over a velocity range from -120 km s^{-1} to +100 km s^{-1}. The strong absorption feature at +60 km/s^{-1} is resolved into four separate clouds, which are closely associated with the HII region G0.7-0.0. It is suggested that the ionized gas and the dense molecular clouds may be interacting dynamically to produce the observed difference in velocity between the H109α recombination line and the OH absorption lines.

The implications of these observations for various kinematical models of the galactic center are discussed. Simple models with one or two expanding and rotating rings are not adequate to explain the data.

The excitation temperature of the OH 1667 MHz transition is less than 10 K , based on the maximum line temperature away from the continuum sources. However, one anomalous region north of G0.7-0.0 shows apparently thermal line emission, which implies an excitation temperature between 30 K and 80 K if the gas is optically thick. The thermal emission has a maximum angular extent of 12 arcminutes.

The molecular clouds fall into two groups. Those with positive radial velocities have linewidths which are, on the average, twice as large as those for clouds with negative radial velocities. The positive-velocity clouds tend to have larger optical depths and column densities of OH. The mean value of N_{OH}/T_s for the positive-velocity clouds is $1.6 \times 10^{16} cm^{-2} K^{-1}$, while for negative-velocity clouds, the mean is $4.4 \times 10^{15} cm^{-2} K^{-1}$. For an assumed excitation temperature of 10 K , the space densities of OH molecules exceed by at least an order of magnitude the expected densities based on a theoretical model for the reaction rates of molecule formation. The parameters of the theoretical model may be inappropriate for the galactic center region.

TABLE OF CONTENTS

Chapter 1

INTRODUCTION

The hydroxyl, or OH, molecule was first discovered in interstellar space by Weinreb, et al. (1963), who detected its absorption spectrum against the continuum source Cassiopeia A. Shortly after this discovery, Bolton, et al. (1964) detected the molecule in absorption in the spectrum of Sagittarius A, the strong non-thermal radio source which is generally believed to be associated with the center of our galaxy. Bolton, et al. reported absorption in both of the main lines of the lambda-doublet in the ground rotational state*. Their first observations showed a fairly narrow feature ($\Delta\nu$ = 65 kHz) centered at approximately 0 km/s in the local standard of rest. The line was superimposed on a steeply-sloping baseline, first thought to be an instrumental effect. Subsequent observations at Parkes, reported by Robinson, et al. (1964) showed that the "sloping baseline" was actually the low-velocity side of a very broad and deep absorption line centered at +40 km/s. The Parkes group also noted that this absorption had no marked counterpart in the neutral hydrogen spectrum, that its high positive velocity implied large radial motions in the gas near the galactic nucleus, and that the large linewidths might be

*The rotational states of OH are split by lambda-doubling, and further split into four levels by hyperfine interaction of the nuclear spins. The ground-state hyperfine transitions occur at these frequencies: 1612.231 MHz ($F = 1^+ \rightarrow 2^-$); 1665.401 MHz ($F = 1^+ \rightarrow 1^-$); 1667.358 MHz ($F = 2^+ \rightarrow 2^-$); 1720.533 MHz ($F = 2^+ \rightarrow 1^-$), where F is the total angular momentum, quantum number, including nuclear spin, and "+" or "-" denote the state parity. The "main lines" are those at 1665 and 1667 MHz; those at 1612 and 1720 MHz are called "satellite lines". Frequencies are from Radford (1964).

due to rapid rotation of the gas cloud.

Soon after publication of the Parkes result, the deep absorption line centered near -130 km/s in the Sgr A spectrum was discovered by Goldstein, et al. (1964), who reported that this feature was comparable both in optical depth and linewidth, to the one at +40 km/s. Thus, it appeared that there existed dense molecular concentrations in rapid motion both toward and away from the galactic nucleus. These early observations were the first evidence that the kinematic and physical conditions of the gas in that region might be different from the situation deduced by Rougoor (1964) from neutral hydrogen spectra.

Since these earliest observations of OH were made, a large number of interstellar molecules have been detected at radio frequencies. Most of these molecules are observed in the spectra of Sgr A or of the nearby complex of thermal sources called Sgr B2. (For an extensive review of interstellar molecules, see the article by Rank, Townes, and Welch (1971).) The galactic center region possesses an abundance of molecular species, most of which show strong spectral features in specific velocity ranges. In particular, the molecular cloud near +60 km/s in the spectrum of Sgr B2 is well known. The observations have established two important facts: (i) the galactic center region must be the site of intense chemical activity in the interstellar medium; (ii) there are very large noncircular motions associated with the molecular clouds which are weak or absent in the spectrum of neutral hydrogen. Observations of molecular lines at the

galactic center, then, should yield evidence related not only to the physical and chemical conditions within the molecular clouds, but also to the kinematics of the gaseous matter near the nucleus of the galaxy.

The existence of the molecules poses important questions about the chemistry of their formation and destruction. The molecules appear to be intimately associated with dust grains, which provide shielding from dissociation by visible and UV photons. One of the probable mechanisms by which molecules are formed is through reaction of atoms adsorbed on the surface of grains (Hollenbach and Salpeter 1971) although, more recently, gas-phase reactions between neutrals and positive ions have been suggested as an important mechanism (Herbst and Klemperer 1973). The temperature and physical composition of the dust are crucial parameters for adsorption on grains, while the ionization and elemental abundances of the gas are most important for the gas-phase reactions. The spectra of the various molecular species should give information about the density and temperature of the gas, the nature of dust grains, elemental abundances in the clouds, and, perhaps, the degree of ionization in the gas (which, in turn, can be related to the flux of energetic particles and photons). Clearly, detailed observations of the molecular regions are of great importance in understanding the physics of the interstellar medium.

The kinematics of the gas in the nuclear region must be related to the nature and past history of the galactic nucleus itself. The large positive and negative velocities seen in the OH spectrum of

Sgr A show that radial motions are at least as important as rotational motions about the center. To explain this motion, Oort (1971) has suggested that the nucleus of our galaxy has undergone a series of explosive events, not unlike those seen in the nuclei of Seyfert galaxies, within the last 10^7 years. The molecular clouds, then, may be remnants of the explosions, and have either been propelled away from the nucleus, or are now falling back toward the center. Along similar lines, van der Kruit (1971) finds evidence for an expulsion of matter at an angle from the galactic plane, with the expelled gas eventually falling back into the galaxy. Kinematical models to describe the positions and velocities of the gas clouds have been proposed by Scoville (1972) and Kaifu, et al. (1972). Their models place the molecular condensations in rotating, expanding rings about the nucleus. More recently, alternative explanations for the observed gas motions have been proposed by Simonson and Mader (1973) and by Scoville (1973). Instead of invoking explosive events, Simonson and Mader propose a model based on a two-armed spiral density wave. Scoville suggests that the gas motions can be explained by a two-armed spiral structure which is undergoing both rotation and expansion.

In order to test these models, we require extensive mapping of the spatial and velocity distributions of the molecular regions. Since the galactic center contains a number of bright continuum sources with angular sizes on the order of 3 to 5 arcminutes, the angular resolution of the map should be at least that good. Otherwise the bright continuum sources will alias the spectra of nearby regions. For high-frequency

molecular lines, one could obtain adequate resolution with large antennas. The OH lines are at such low frequencies, however, that even the largest single-dish antennas have inadequate resolution, according to the criterion just mentioned. Adequate angular resolution is possible either by lunar occultation observations, which, however, are both limited in sensitivity and complicated to interpret, or by an interferometric aperture synthesis.

The kinematical models for the molecular clouds have been based primarily on observations of the 1667 MHz OH line and of the 4830 MHz line of formaldehyde. Of these two, the OH observations are the most complete. After the initial observations at Parkes, an extensive survey of the galactic center in the 1667 MHz line was carried out by Robinson and McGee (1970). Their observations covered a range of galactic longitude from $-2^{\circ}30'$ to $+3^{\circ}20'$, between latitudes $+0^{\circ}20'$ and $-0^{\circ}40'$. The beamwidth of the antenna was $12\farcm2$, and their velocity resolution was 6.7 km/s. In a subsequent analysis of the results, McGee (1970a) catalogued a total of 63 discrete OH clouds in the surveyed region. Many of the individual clouds were comparable in angular size to the antenna primary beam, which suggested that the molecular regions had not been resolved. If so, the optical depths, and hence the calculated column densities of OH would be underestimated.

Observations of the lunar occultations of the Sgr A region by Kerr and Sandqvist (1968, 1970) gave evidence that the dense molecular cloud at +40 km/s had a velocity gradient with position of about 8 km/s per arcminute. The gradient was interpreted in terms of a rotation of

the cloud. These lunar occultation measurements had the potential for very good angular resolution. They were seriously limited in sensitivity, because the integration time per spectrum was never more than 70 seconds. The circumstances of the occultations were such that the data did not allow the source structure to be recovered unambiguously. Moreover, the analysis is so formidable that the interpretation of the observations has not yet been completed (Sandqvist 1973).

At the time the present study was proposed, it seemed clear that a better understanding of the molecular clouds near the galactic center would require a considerable improvement in angular resolution, and perhaps somewhat better velocity resolution as well. One would like to be able to map as large a region of the sky as possible, in order to test the kinematical models for the molecular features. At the same time, the angular resolution should be sufficient to resolve the molecular clouds. Only if the telescope beam is comparable to, or smaller than, the cloud sizes can the true optical depth be determined. An important limitation on single-dish observations, especially in the 18 cm OH line, is the uncertainty in the filling factor for the cloud in the antenna beam. Since this factor is usually unknown, it has generally been set equal to unity (e.g., Turner 1972), an unwarranted assumption which can lead to serious errors in the determination of optical depths.

A multichannel aperture synthesis offers the best combination of good angular resolution and sensitivity for spectroscopic observations of molecular regions. The galactic center lies at such a low declination (-29^{o}) as to be inaccessible for a full two-dimensional

mapping by the existing earth-rotation synthesis arrays. However, the antenna configurations possible with the Owens Valley Radio Observatory (OVRO) twin-element interferometer allow high angular resolution in both right ascension and declination, even for a source at -29^{o}. The interferometer can be set up for baselines with north-south, east-west, or skewed orientations. By an appropriate choice of baselines one can measure the visibility function of a radio source over a fairly uniform sample of points in the so-called "u-v" plane (where u and v are the Fourier transform coordinates corresponding to right ascension and declination). The brightness distribution is then recovered by performing a Fourier transformation of the data. It will be seen that a circular beam can be synthesized even for declination -29^{o}. Thus, an aperture synthesis study of the galactic center is possible with this instrument.

Given the receivers available, the only practical possibilities were studies of either the λ18 cm OH lines or the λ6 cm formaldehyde line. Of these two, the OH line was chosen for several reasons: (1) The 1667 MHz OH line is stronger than the formaldehyde line, especially at negative velocities; (2) The λ6 cm receivers at the OVRO are a factor of two noisier than the λ18 cm receivers; (3) The OH line can be synthesized over a much larger region of sky than the formaldehyde line, because of the larger primary beamwidth at λ18 cm. The formaldehyde line provides higher angular resolution for the same set of baselines. However, it was decided that adequate angular resolution could be obtained for the OH line, so that the larger synthesized region was of greater importance. Since the galactic center radio

emission comes from a number of sources distributed over some two square degrees, the entire region could not be synthesized in a single map. (The primary beamwidth of the 90-foot antennas is 24' at λ18 cm). For this reason, two fields were selected, one containing Sgr A, and the other the Sgr B2 region.

Chapter 2

OBSERVATIONS

This chapter discusses the choice of parameters for the observations, the instrument and its calibration, the observational procedure, reduction of the data to calibrated visibilities, and the Fourier inversion method.

Choice of System Parameters

The choice of inteferometer baselines was dictated by the following requirements:

(1) The large angular dimensions of the galactic center sources required a synthesis of essentially a full primary beam area. The minimum sampling interval in the u-v plane should then be approximately the inverse of the primary beamwidth, which is 24 arcminutes (FWHM) for the antenna feeds used. Hence, the minimum sampling interval should be about 150 wavelengths, or 100 feet.

(2) The configuration of tracks in the u-v plane for sources at -29^{o} declination requires diagonal baselines to fill in gaps between east-west and north-south baselines.

(3) The low declination of the sources restricts observations to $\pm 3^{h}.2$ in hour angle.

(4) The observing program should be finite in length. In practice, a total of eight weeks' observation seemed a reasonable limit.

Given these constraints, a set of eight baselines was chosen. The sampling of the u-v plane which these provided is shown in the discussion

of the Fourier inversion. The baselines and chronology of observations are given in Table 2-1.

Table 2-1

Chronology of the Observations

Dates	Spacing
20-26 Aug 1971	300 ft. E/W
27 Aug - 1 Sept 1971	400 ft. E/W
24-30 Nov 1971	800 ft. N/S
2-5 Dec 1971	600 ft. N/S
22-28 Mar 1972	100 ft. E/W
7-12 May 1972	200 ft. E/W
19-24 July 1972	400 ft. N/200 ft. W
25 July - 1 Aug 1972	400 ft. N/200 ft. E

The choice of filter widths for the narrowband channels was determined by the available equipment. The set of forty-eight 50-kHz filters would have been sufficient to cover the full range of OH absorption velocities in the galactic center, as shown in observations at Parkes by Robinson and McGee (1970). However, the OH spectrum of Sgr A is known to have narrow-velocity features (Palmer and Zuckerman 1967), which would be badly smeared out with 50-kHz filters. Equally important, observations of lunar occultations in the OH and formaldehyde lines (Kerr and Sandqvist 1968; 1970) showed evidence for large gradients of the position of the absorbing clouds with velocity. Gradients on the order of 10 km/sec per arcmin were suggested. For a filter width of 50 kHz (9 km/sec) and a synthesized beam three arcminutes in diameter, these large gradients in velocity could blur the absorption

features in the maps and cause the optical depths to be underestimated. It was therefore decided to use the next narrowest set of filters, which have bandwidths of 4 kHz and center-frequency separations of 8 kHz. Although this velocity resolution was somewhat better than necessary, it seemed prudent to err on the side of too much data, rather than too little. Moreover, use of the 4-kHz filters provided some redundancy in the final results which proved useful in analyzing errors of measurement.

In order to cover the range of known OH absorption velocities, five settings of the local oscillator were required. The frequency offsets were chosen so that there was an overlap of three channels on the ends of the inner settings. This overlap provided a means of checking the continuity of the data and the internal consistency of the maps. The range of velocities covered was from +100 km/sec to -225 km/sec. (All velocities in this work are referred to the local standard of rest (Allen 1963).) For both Sgr A and B2, this range encompasses essentially all the absorption detected by Robinson and McGee (1970). During the observations, a single frequency shift was observed each day, so that a total of five days of observations were required per interferometer spacing. The frequency offsets and corresponding velocities, all referring to the center of the narrowband filter bank are given in Table 2-2.

Table 2-2

Frequency and Velocity Offsets for Sgr A and B2

Frequency Shift	Offset (kHz)	Velocity (km/sec)
1	-367	+65.92
2	- 15	+ 2.63
3	337	-60.67
4	689	-123.96
5	1041	-187.25

The Instrument and Its Calibration

The observations were conducted with the twin-element interferometer of the Owens Valley Observatory. The basic configuration of the antennas has been described by Moffet (1962). The local oscillator system was essentially the same as the one discussed by Read (1963) with some modern improvements to the equipment. In particular, the IF delay lines are controlled by a digital computer which calculates the geometric delay in arrival time for a wavefront coming from the source to the specified antenna positions. The delay cables may thus be set to any value between 0 and 8191 nanoseconds in 1 nanosecond increments. The delay was tracked to maintain the interferometer fringe amplitude at the peak of the delay response (the "sausage pattern"). To prevent changes in IF signal attenuation as the delaying cables are switched in and out, a compensating length of lossy cable (nichrome center-conductor) is inserted in the IF line when the corresponding section of delaying cable is switched out by the computer. The maximum change in IF attenuation due to tracking delay is estimated to be less than one percent for these observations (Read, private communication). This

point is significant because automatic gain control was not used for five of the eight spacings. Changes in IF attenuation would therefore have been reflected in systematic gain variations which would not be removed by the instrumental calibration procedure.

The other modernization of the interferometer involved the phase rotation of the 1 MHz reference signal to the local oscillators. The analog rate computer has been replaced by the digital computer, interfaced with an eight-bit phase shifter. The computer calculates the phase and fringe rate expected for the source position, local sidereal time, and interferometer baseline. It then servos the phase shifters to the calculated phase, driving them at a rate sufficient to offset the natural fringes and produce a fixed fringe period, which for these observations was always 60 seconds. Both the IF delay line settings and the phase shifter phases are recorded simultaneously with the data, for use in the post-observation reduction programs.

The two receivers used throughout these observations were identical; each consisted of a parametric amplifier followed by a tunnel diode amplifier (TDA). A cavity filter after the TDA eliminated the unwanted sideband. Following the sideband rejection filter were the mixer and IF amplifier. The noise temperature of the system was typically 85^{o}K on cold sky.

The two IF signals are brought from the antennas to the observing room, amplified, and each divided into five separate outputs. One, reduced by 20 dB, is the input for the wide-band correlator,

subsequently referred to as channel 1. The other four pairs of IF signals, each 6 dB down, are the inputs to the four sets of filter banks. Each filter bank consists of twelve matched pairs of crystal filters and twelve correlators. The half-power bandwidths of the filters are 4 kHz, and separation of center frequencies is 8 kHz for the filters used in the galactic center observations. Since the data recording system can handle a maximum of 48 inputs, the last filter pair of the fourth bank was deleted in favor of the wideband channel. Channels 2 through 48 thus provided a continuous sequence of center frequencies from 9.812 MHz to 10.180 MHz, in increments of 8 kHz.

Before beginning the program of observations, the filter banks were checked to determine whether the filters all met the specified bandwidth and center frequencies. Banks 1 and 2 were found to have widths of about 5 kHz, while banks 3 and 4 typically gave 3.5 kHz widths. One filter, at 10.020 kHz (channel 28), exhibited excessive insertion loss, a 3 dB bandwidth of 0.8 kHz, and an incorrect center frequency. All other filters had the correct center frequencies within ±0.1 kHz, corresponding to a velocity error at λ 18 cm of ±0.018 km/s.

To facilitate calibration of the multi-channel receiver, it was decided to employ a technique first developed by Greisen (1973), which uses a broadband solid-state noise diode to add coherent noise to the inputs of the two receivers. (The use of such noise sources as calibration standards has been discussed by Keen (1971), who found that the noise output is both constant with time and free of spectral features.) The output of the diode was divided equally and transmitted

by cables to the two antennas, where the noise was injected into the inputs of the parametric amplifiers through 20 dB directional couplers. The diode could be turned on or off by remote control from the observing room. To check for flatness of the noise spectrum, strong unabsorbed sources (Virgo A and Orion A) were compared with the noise source. There was no evidence of any small-scale spectral feature greater than the rms noise level. The noise diode thus provided a strong, readily accessible standard for comparison of the narrowband filter channels with the broadband channel. Details of this comparison are discussed in the section on calibration.

The OVRO interferometer is equipped with automatic gain control in the IF amplifiers, which maintains a constant power level to the correlator inputs. During the first three observing sessions (comprising five baselines) the AGC was not used, in the belief that the total system gain could be more accurately calibrated than could the AGC compression factor. If all amplifiers are linear (i.e., unsaturated) and the correlator is a square-law device, then the measured fringe amplitude will be proportional to the correlated flux density of the radio source, if AGC is not used. (This relation is implicitly assumed in the CIT data reduction programs.) If AGC is employed, the system gain is reduced by a factor, R , given by

$$R = \frac{T_{sys}}{T_{sys} + T_{source}} \simeq \frac{T_{sys}}{T_{sys} + 0.1 S_{total}}$$

where T_{sys} is the system noise temperature on cold sky, T_{source} is

the noise temperature due to the radio source, and S_{total} is the total flux density of the source. (The factor 0.1 is approximately correct for the 90-foot dishes of the interferometer, assuming an aperture efficiency of 50%.) With the low-noise receivers used in this program, the large flux density in the galactic center region increased the system temperatures by as much as 45%, so that R would be significantly different between the calibration source NRAO 530 and the Sagittarius sources. Early in the program, it was not clear that the system temperature would be sufficiently constant to allow the use of AGC. Instead it was decided to let the noise levels vary as they might, and calibrate the gain directly.

This procedure led to substantial difficulties with the narrow-band calibration, due to the dissimilarity of detector laws, as will be discussed below. The first set of observations (August 1971) were especially troublesome, as there was no temperature control on the receiver boxes at that time. The day-night temperature change of the receivers sometimes exceeded 20°C, with commensurate large changes in receiver gain. When temperature controllers were installed, the ambient temperature of the receivers was normally constant within 2°C, and gain variations were markedly reduced. As my experience with the equipment increased, the use of AGC became more attractive. Crutcher (private communication) indicated that the temperature-controlled 18-cm receivers had noise temperatures which varied by only about 2% or less in a day. If T_{sys} is constant, then the AGC compression factor for a particular radio source will be a constant which can be applied equally to all channels and all observations for one day. In fact it

was found that the same value of R could normally be applied to all observations of the same source for all five frequency shifts.

The value of the compression factor was measured by a straightforward technique. An observation with AGC was made, immediately followed by one with the AGC turned off, then another with AGC on. The calibrated flux density without AGC was compared with the average of the two bracketing observations, yielding the compression factor directly. The calibration was generally done when the visibility amplitude was not changing rapidly with hour angle, to reduce errors in the interpolated value. The uncertainty in the calculated compression factor should not be affected by errors in the instrumental gain function, which varies slowly with time. The uncertainty in the compression factor is less than five percent.

In an observing program such as this one, where a wide range of source intensities is encountered, the nature of the detector law of the receiver is crucially important in the calibration of flux densities. Greisen (1973) investigated the detector law for the broadband correlator of the OVRO interferometer. He concluded that the detector law was somewhere between linear and square-law. Since Greisen's observations, the old broadband correlator has been replaced by a new device. To determine the response of the new broadband correlator and compare it with those in the narrowband channels, a series of observations were made using the noise diode as an artificial source. It was particularly important to determine whether the relative amplitudes of the narrow and broadband channels depended on the IF input power levels. Because IF automatic gain control was not used for the first

five spacings, the power level of noise diode observations was generally different from the power levels on Sgr A and B2. Any change in relative fringe amplitudes with IF power level would introduce systematic errors in the flux calibration of the narrowband channels.

The results of these tests showed that the broadband fringe amplitude is linearly related to the input power level, so the new correlator is a proper square-law device. However, the ratio of broadband to narrowband amplitude depends on the input IF power levels. A calibration curve was derived as an average value for all the channels. The IF noise power is measured on two panel meters. The relative amplitude ratio is normalized to unity at a value of 10.0 on the meters. (The calibration was done with identical power levels in each input to the correlators. During observations these levels were not different by more than 10%.) The scatter of channel amplitude ratios about the mean was found to be about 1%. The correction factor was applied to all the calibrated narrowband fringe amplitudes in observations where AGC was not used. (When AGC was employed, the input power levels to the correlators were constant for all radio sources, so the effect did not occur.) It was also found that the relative phase of the broadband and narrowband channels are unaffected by input power levels. The calibration curve is shown in Figure 2-1. The abscissa is the meter reading, proportional to IF power level. The ordinate is the normalized ratio of narrowband to broadband fringe amplitude. For Sgr A the correction factor was as large as 9%, while for Sgr B2 it was generally less than 3%.

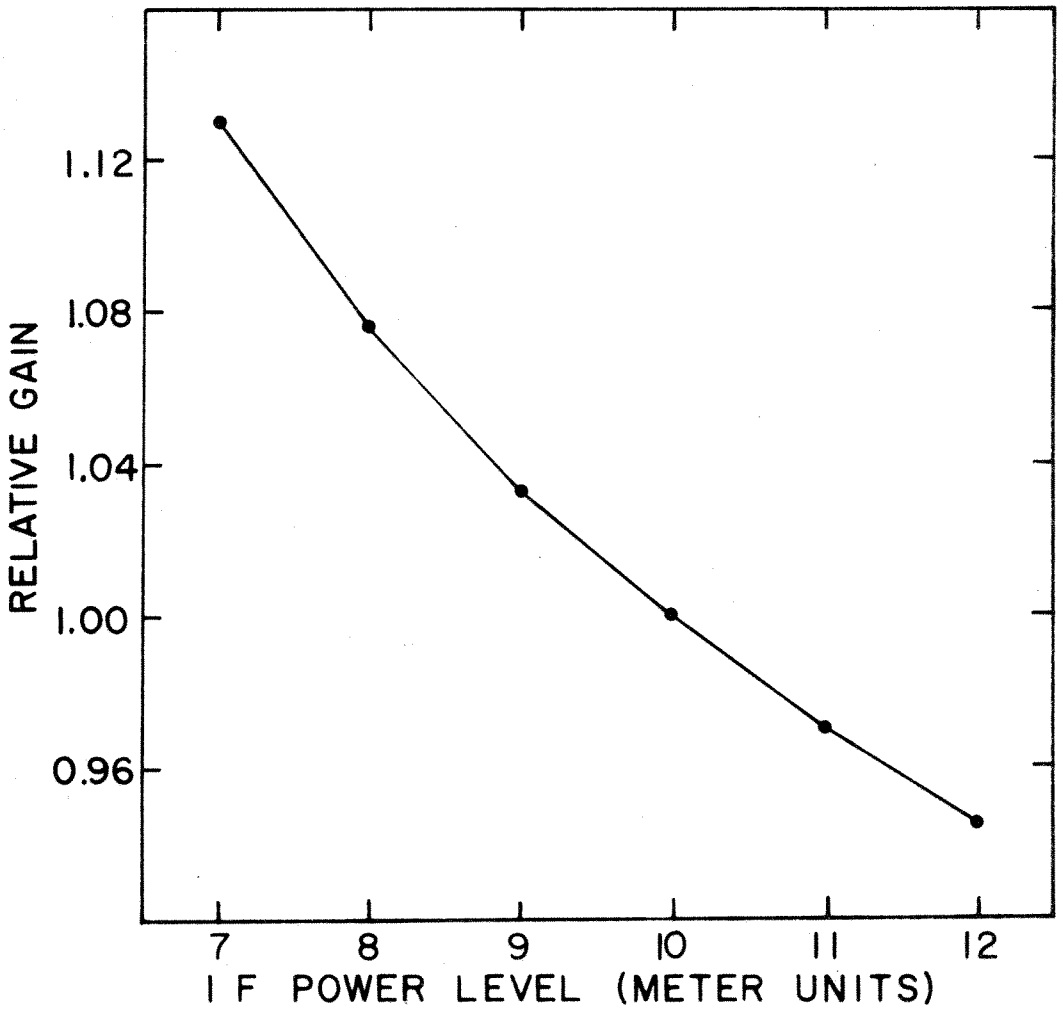

Fig. 2-1 Relative narrowband channel gain as a function of IF power level. Abscissa is in units of panel meter readings

The voltage output of a single-sideband interferometer may be written (Shostak 1972) as:

$$V(\tau_1,\tau_2) = GA(\tau_1+\tau_2)\cos[(\omega_{LO}+\omega_{IF})\tau_1+\omega_{IF}\tau_2+\phi] \qquad (2.1)$$

where τ_1 is the differential signal propagation delay before the mixers, τ_2 is the differential delay after the mixers, G is the overall gain of the system, and $A(\tau_1+\tau_2)$ is the Fourier transform of the product of the IF bandpass times the source power spectrum. The term ϕ includes the instrumental phase, which usually varies slowly with time of day; the phase due to radio source position and structure; and the phase produced by the computer-driven phase shifters. The value of ω_{LO}, the local oscillator frequency, is precisely determined, but that of ω_{IF}, the center frequency of the IF passband, may not be. For the narrowband channels, the value of ω_{IF} is known with an accuracy of better than 0.1 kHz, while for the broadband channel, ω_{IF} may be significantly different from 10 MHz, the nominal center frequency of the IF amplifiers. (Early in 1972, new wideband IF amplifiers were installed which would have altered the effective broadband IF frequency. To eliminate this effect, a pair of matched filters centered at 10.0 MHz and with 5 MHz bandwidths, were constructed and used in all subsequent observations.)

From equation (2.1) it is clear that the quantity $(\tau_1+\tau_2)$ must be held constant if the fringe amplitude is to be unaffected by the factor $A(\tau_1+\tau_2)$. In practice, the value of the function $A(\tau)$ was maximized by adjusting the delay center, which is the value of τ_2 for a source on the interferometer meridian. If the IF bandpass is

simple and symmetrical (e.g., gaussian) about some frequency ω_{IF}, then that delay for which A is maximum will also be the delay such that $\tau_1 + \tau_2 = 0$. It is easily shown (Read 1963) that if the IF passband is gaussian with bandwidth $\Delta\nu_{IF}$, $A(\tau)$ is also gaussian with a width given approximately by

$$\Delta\tau \simeq \frac{1}{\Delta\nu_{IF}}$$

For the broadband channel, $\Delta\nu_{IF} = 5$ MHz, so $\Delta\tau \simeq 200$ ns. Thus the function $A(\tau)$ has a broad peak; the value of the delay center determined by maximizing A may be in error by several nanoseconds. Such errors will introduce frequency dependent phase offsets which in some cases were sufficient to warrant an additional calibration procedure.

If the delay center and IF frequency are not known precisely, we can write

$$\tau_1 + \tau_2 = \Delta\tau$$

and

$$\omega_{IF} = \omega_{IF_o} + \Delta\omega_{IF}$$

where $\Delta\tau$ is the error in the delay center, $\Delta\omega_{IF}$ is the error in the value of the IF center frequency, and ω_{IF_o} is the assumed value of the IF center frequency, which is used in the computer reduction. Then the actual interferometer response has as the argument of the cosine in equation (2.1),

$$\omega_{LO}\tau_1 + \omega_{IF_o}\tau_1 + \Delta\omega_{IF}\tau_1 + \omega_{IF_o}\tau_2 + \Delta\omega_{IF}\tau_2 + \phi$$

from which the reduction program subtracts the computed value

$$\omega_{LO}\tau_1 + \omega_{IF_o}\tau_1 + \omega_{IF_o}\tau_2$$

The residual phase includes an error given by $\Delta\omega_{IF}\Delta\tau$. Thus, for example, a delay error of 10 nanoseconds and a broadband IF frequency error of 1 MHz will cause a phase offset of 10 millilobes (1 millilobe = $2\pi/1000$ radians). Since the computer tracked the delay during the observations, it can be assumed that the error $\Delta\tau$ is due only to an incorrect delay center, and so is constant throughout a set of observations. The broadband phase error will therefore be removed by the instrumental calibration. But for the narrowband channels, $\Delta\omega_{IF}$ is zero. As a result, there will be a systematic difference between the broadband and narrowband phases.

If the channel calibration relative to the broadband were done on celestial sources, the effect would be removed by the narrowband calibration procedure. But because the noise diode requires a separate determination of the correct delay, any error in that delay will result in a phase offset of $\Delta\tau_{ND}\Delta\omega_{IF}$ for the narrowband channels on all celestial sources, where $\Delta\tau_{ND}$ is the error in the noise diode delay setting, and $\Delta\omega_{IF}$ is the broadband IF frequency error.

Such an effect was detectable, though small, in most of the observations. As expected, the phase offset was constant, within the noise level, for a given interferometer spacing. The offset was determined by averaging the narrowband phases of the observations of calibration sources (other than the noise diode) and subtracting the broadband phase. This difference was then added to the narrowband channels of the galactic center observations. For three of the eight

spacings, the noise diode delay was sufficiently accurate that no correction was made. The other observations typically required corrections of 10 or 15 millilobes, though for the 300' E/W spacing, the correction was 40 millilobes.

Since the antennas cannot be set down in precisely repeatable positions, one or more baseline calibrations were done at each spacing to determine the true spacing and the coordinates of the interferometer pole. A set of unresolved sources with accurately known positions was observed. The baseline parameters were determined from the measured phases by an iterative procedure which alternately removes an instrumental phase and solves for the best-fit baseline. Convergence was always rapid, generally requiring only three iterations. Usually two or three separate calibrations were done at each spacing. The agreement between independently determined baselines was always within two standard deviations (as calculated from the least-squares fit) of the fitted parameters.

For the Galactic Center sources, the calibration standard was NRAO 530, which is completely unresolved at the longest spacing of this series of observations. The 1950.0 coordinates of NRAO 530 are (Wade 1970; Kristian and Sandage 1970): R.A. = $17^h30^m13\overset{s}{.}5$, Dec = $-13^o02'46"$. Since the source is some 16 degrees north of Sagittarius A, it could be observed both before the galactic center had risen and after it had set, providing a complete instrumental calibration on only one standard source. Unfortunately, NRAO 530 has a time-varying flux density (Kellerman and Pauliny-Toth 1968). While the percentage change would

not be expected to be large at 1.7 GHz, it was necessary to determine its flux density during each observing session by comparing NRAO 530 with other calibrators. Pairs of observations were made before or after the galactic center was up. The comparison sources were 3C286 and 3C409. Flux densities at 1667 MHz for these two sources were interpolated from data given by Kellerman, Pauliny-Toth, and Williams (1969). The values used were 13.1 f.u. for 3C286 and 11.6 f.u. for 3C409 (1 f.u. = 10^{-26}W $m^{-2}Hz^{-1}$). The adopted value for NRAO 530 is an average of several pairs of observations at each spacing. The results of the calibration for the various observing sessions are shown in Figure 2-2.

The pointing corrections of the two antennas were measured at the beginning of each observing run and whenever the antennas were moved to a new spacing. The correction curves were generally believed to be accurate to one arcminute. At 18 cm wavelength an offset of this amount from the beam center will reduce the antenna gain by slightly more than one percent. At the half-power points, an offset of one arcminute will change the gain by nine percent. During observations of the galactic center, the antennas were pointed up on Sgr A, then offset by fixed amounts in right ascension and declination to the Sgr B2 position.

The coordinates for Sgr A were taken from Maxwell and Taylor (1968), who give: R.A.(1950) = $17^h42^m30\overset{s}{.}7$; Dec (1950) = $-28^o59'12"$. For Sgr B2 it was decided for two reasons to point to a position offset from the continuum peak. First, McGee (1970a) shows that the largest concentration of OH in the vicinity of the Sgr B2 source,

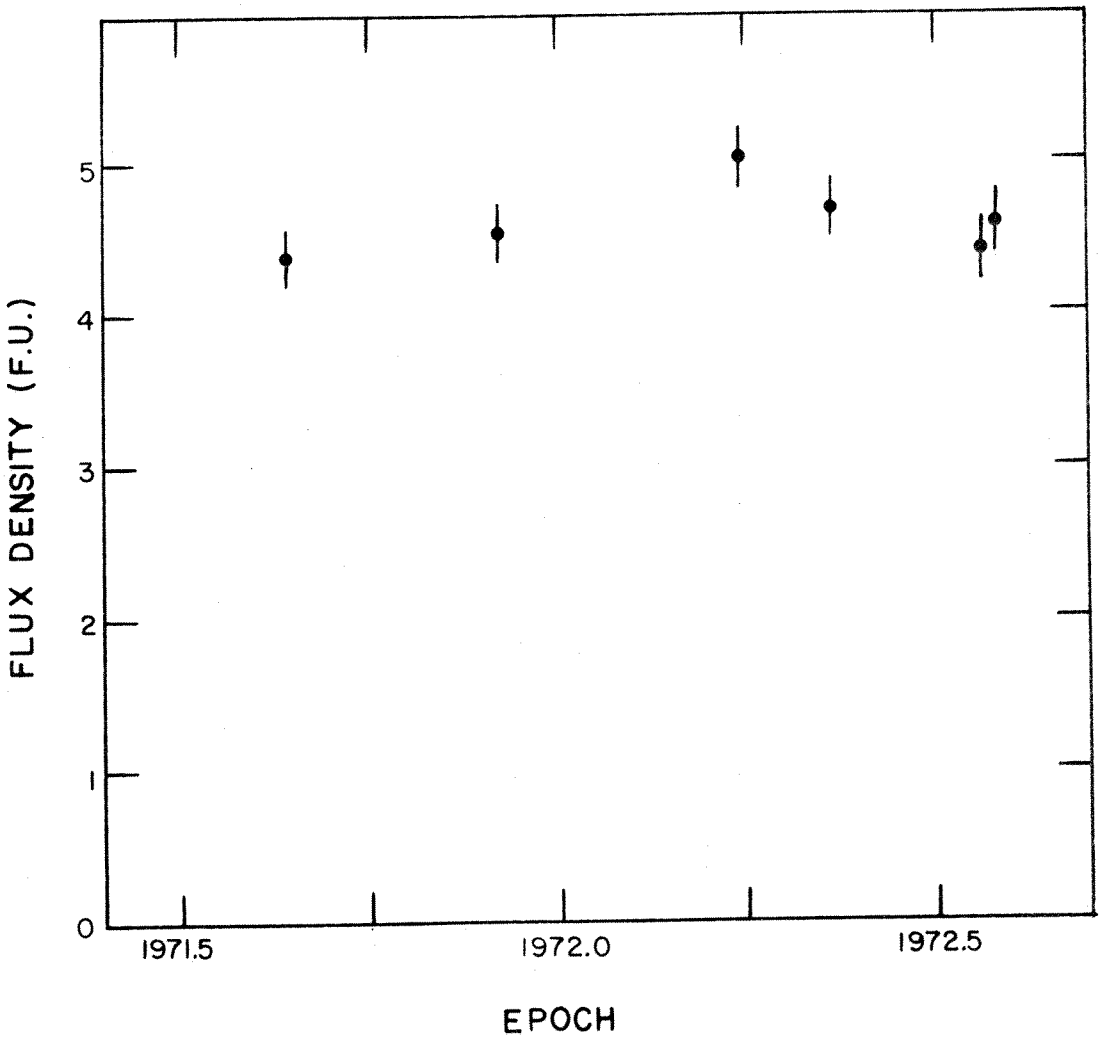

Fig. 2-2. Absolute flux calibration of NRAO 530.

G0.7-0.0, lies at galactic latitude b = -15' to b = -20' . To achieve maximum sensitivity in this region of the sky without an increase in the noise level at the position of G0.7-0.0, the telescopes were pointed east of the continuum peak by 10 arcminutes, so that the maximum antenna gain was at the position of the OH concentration. The antenna gain was reduced by about 2.5 dB at the peak of G0.7-0.0, which did not significantly degrade the signal-to-noise ratio on the continuum sources. The 1950.0 coordinates for the Sgr B2 observations were: R.A.(1950) = $17^h45^m04\overset{s}{.}0$; Dec.(1950) = $-28^o24'00''$. Examination of the broadband visibility amplitudes for Sgr B2 showed that the scatter of calibrated fluxes was not worse than 5%, indicating that this offset procedure did not introduce any significant errors due to mispointing of the antennas. Moreover, this offset had the added advantage of reducing the effect of confusion due to the Sgr A continuum by about 4 dB. The presence of a strong source near the region to be synthesized could produce spurious sidelobe responses in the maps. Since Sgr A is an order of magnitude more intense than the Sgr B2 sources, further reduction of the Sgr A flux entering the antenna sidelobes was desirable.

Observational Procedures and Data Reduction

The method by which the observations were made was as follows:

(a) The celestial calibrating source was observed to provide initial phase and gain information.

(b) The artificial noise source was used to calibrate the narrowband channels relative to the broadband.

(c) Pairs of observations of Sgr A and Sgr B2 were made, switching back and forth between the two sources. The integration time per observation was usually ten minutes. During this interval the projected baseline vector at the source position changed by much less than 150 wavelengths even at the longest spacings, so that angular resolution was not degraded by smoothing of the visibility function. The local oscillator frequency was set at the beginning of each record to compensate for the Doppler shift due to the earth's motion. The velocity correspondence of the filters was maintained to within 5% of the filter widths.

(d) After three or four such pairs of observations, calibration was repeated as in (a) and (b).

(e) When the galactic center had set, a final pair of calibration records was made.

The raw data tapes were reduced to fringe amplitudes and phases with the standard OVRO computer programs (Fomalont, Wyndham, and Bartlett 1967). Calibration of the measured visibilities involved three steps. First, the instrumental phase and gain variations are determined from observations of the celestial calibration sources. A polynomial is fitted to the weighted data points, where the weighting is done by convolving the data with a gaussian of half-width typically chosen as two hours. The convolution process reduces the effect of possible errors in any given datum. (Obviously wild points were deleted before the final calibration.) The resulting smooth functions are applied to the broadband observations only. In the second step, the phase difference and gain of each narrowband channel, relative to

the broadband, are determined from the observations of the noise diode. Usually the multichannel receiver was sufficiently stable that the average value for each channel over the day's span of observations was accurate enough. The relative phase difference and amplitude ratio of each narrowband channel are applied to the observations, completing the standard calibration procedure. The calibration program also computes an error for each amplitude and phase. The relative amplitude error is dependent on the correlated flux density. The phase error is constant for large amplitudes, but increases substantially as the correlated flux becomes small. Typical amplitude and flux errors as a function of the fringe amplitude are presented in Table 2-3:

Table 2-3

Narrowband Visibility Errors of a Single Measurement, After Calibration

Source	Ampl. (f.u.)	Ampl. Error Absolute (f.u.)	Ampl. Error Relative (%)	Phase Error (fringes)
Sgr A	215	2.4	1.1	0.0015
	180	1.9	1.1	0.002
	135	1.6	1.2	0.003
	40	1.0	2.5	0.006
Sgr B2	28	0.5	1.8	0.003
	12	0.7	6	0.012
	8	0.7	9	0.014
	5	0.7	14	0.025
	1.5	0.5	30	0.050

Finally, because of the instrumental effects discussed above, an additional set of corrections were made to the data. These include the amplitude correction due either to the AGC compression or to the nonlinearity of the correlators, and the phase correction due to errors in the setting of the noise diode delay.

The Fourier Inversion

The principles of aperture synthesis have been discussed by many authors (see, for example, Bracewell 1958; Moffet 1962; Swenson 1969; Christiansen and Högbom 1969). It may be shown that the response of a two-element interferometer to an extended source of radiation is determined by the complex visibility function of the brightness distribution. Thus, let $T(\alpha,\delta)$ be the brightness temperature at right ascension α and declination δ. Assuming the source is restricted to a small range in α and δ, we may approximate the spherical coordinates by Cartesian coordinates x and y, with the origin conveniently taken to be the centroid of the brightness distribution. The complex visibility, $V(u,v)$, is given by the Fourier transform of the brightness distribution:

$$V(u,v) = F(u,v)\, e^{i\phi(u,v)} = K \iint T(x,y)\, e^{2\pi i(ux+vy)} dxdy$$

Here F and ϕ are the fringe amplitude and phase of the interferometer response, and K is a numerical constant determined by the units of measurement. The Fourier transform coordinates u and v are the components of the interferometer baseline projected onto the x and y axes in the plane of the sky. The values of u and v, then, will

depend on the hour angle and declination of the source, on the spacing between antennas, and on the coordinates of the pole of the interferometer. (The interferometer pole is defined as the intersection of the celestial sphere and the line joining the vertices of the two paraboloidal antennas.) Solution of the spherical triangle yields the following relations for u and v :

$$u = S \cos \Delta \sin(h-H)$$

$$v = -S \cos \Delta \sin \delta \cos(h-H) + S \sin \Delta \cos \delta$$

where S is the distance between antennas, normally in wavelengths, h and δ are the hour angle and declination of the radio source (centroid), and H and Δ are the hour angle and declination of the interferometer pole.

To obtain the brightness distribution of a radio source, then, one must sample the visibility function in the (u,v) plane at a large number of points and perform a Fourier transformation on the data. The resulting map will be a representation of the true brightness distribution, the accuracy depending on the sampling of the (u,v) plane. A uniform sampling, without large gaps or holes, is most desirable to minimize the effects of sidelobes in the inverted maps. The number of sample points is necessarily finite, of course, and since the configuration of the antennas is limited to a set of fixed positions, some gaps are inevitable. A typical set of samples in the (u,v) plane is shown in Figure 2-3. In this example the data are for Sgr A at the velocity shift +65 km/sec. (The other velocity shifts for both Sgr A and B2 have essentially the same sampling coverage as this one, except for the

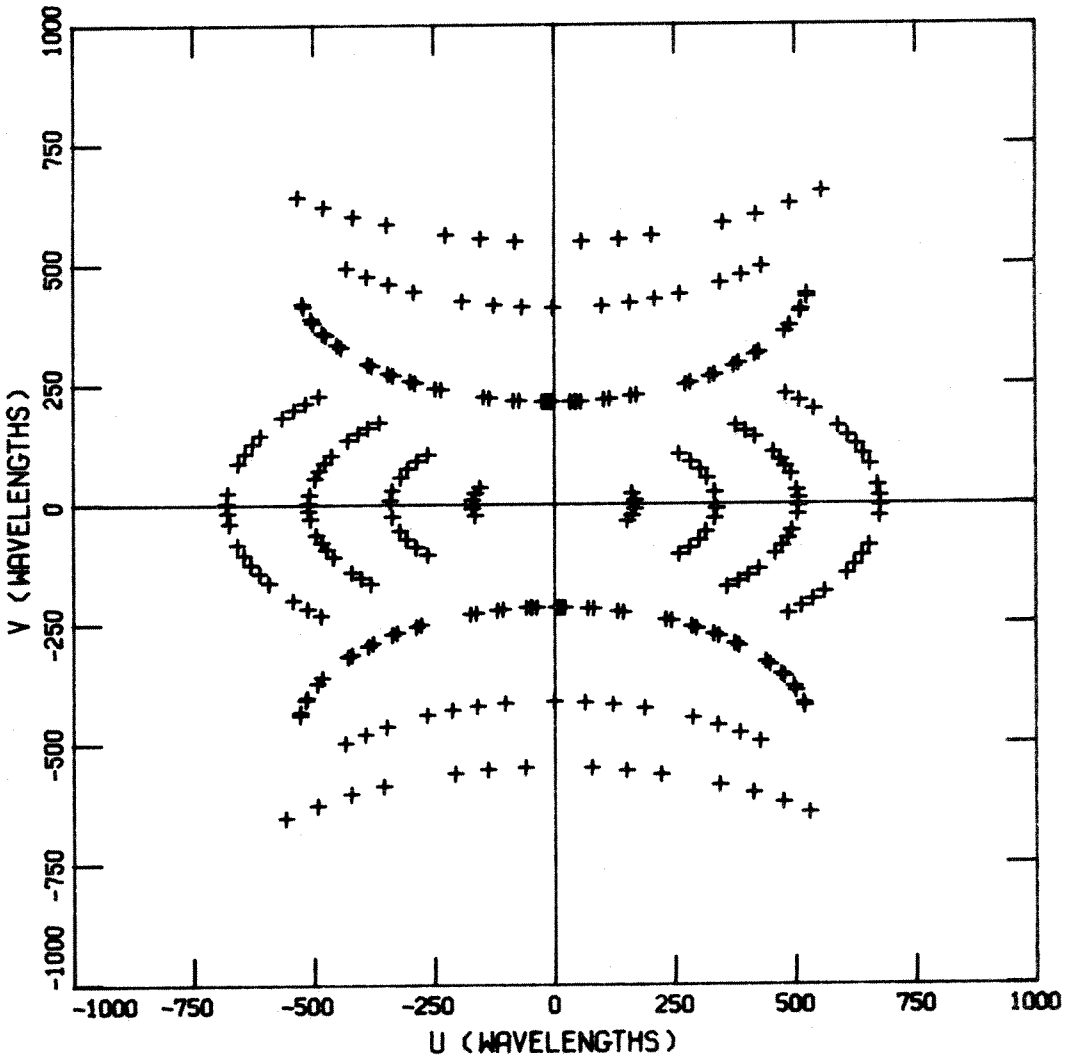

Fig. 2-3. Typical sampling in the (u,v)-plane.

shift at -187 km/sec, for which the 600 feet N/S spacing is missing, due to a mechanical breakdown during the observing run.) Note that each observation is represented by a pair of crosses, symmetric about the origin. This symmetry is due to the Hermitian property of the visibility function, which follows from the fact that the brightness distribution, T(x,y), must be a real-valued function. Physically, it means that transposing the two antennas will produce an interference fringe of identical amplitude but with the sign of the phase reversed.

To perform the Fourier transformation, it was decided to use a direct numerical integration, evaluating a weighted sum over the N data points (Greisen 1973):

$$T(x,y) = \frac{K}{2} \sum_{j=-N}^{N} w_j V_j \, e^{-2\pi i(u_j x + v_j y)}$$

where

$$V_j = F_j \, e^{i\phi_j}$$

The weights, w_j , are inversely proportional to the local density of data points. "Local" here refers to a square centered on the j^{th} point, with sides 120 wavelengths long, or about one minimum sampling interval. No zero-spacing data were included, so $w_o = 0$. Using the Hermitian property of the visibility function, we set:

$$w_{-j} = w_j \; ;$$

$$F_{-j} = F_j \; ; \qquad \phi_{-j} = -\phi_j \; ;$$

$$u_{-j} = -u_j \; ; \qquad v_{-j} = -v_j \; ;$$

so that, invoking Euler's formula, we may write

$$T(x,y) = K \sum_{j=1}^{N} w_j F_j \cos(\phi_j + 2\pi(u_j x + v_j y)) \qquad (2.2)$$

This is the basic equation used in the Fourier transformation of the visibility data. With it we can obtain the response of the synthetic aperture to a point source of unit flux density at the origin of coordinates (x=0, y=0). In this case $F_j = 1$ and $\phi_j = 0$ for all sample points. The result of the transformation for the set of (u,v) points shown above is presented in Figure 2-4. The dimensions of the synthesized region are 84' x 84', with contours at intervals of 10% of the maximum value. Negative contours are dashed, and the zero contour is omitted. This map of a point source, commonly called the "dirty" beam pattern, may be thought of as the aperture diffraction pattern for the synthesized telescope. Note that the sidelobe levels reach ±30%, with ridges mirroring the shape of the tracks in the (u,v) plane. (A direct numerical inversion is possible for these data because of the relatively small number of points in the (u,v) plane. Typically, N was about 130. For large synthesis arrays, such as the Westerbork Synthesis Telescope, the large number of data samples makes a direct numerical integration prohibitively time consuming. See the article by Fomalont (1973) for a comparison of different Fourier inversion methods.)

Given the relatively large sidelobe levels, particularly near the central response, it is desirable to use some means of reducing the effects of confusion due to sidelobes. The method employed here was that developed by Högbom (Högbom 1973) and Rogstad, as described by Greisen (1973). In brief, the true brightness distribution is represented as the sum of a set of gaussian components, each with a width

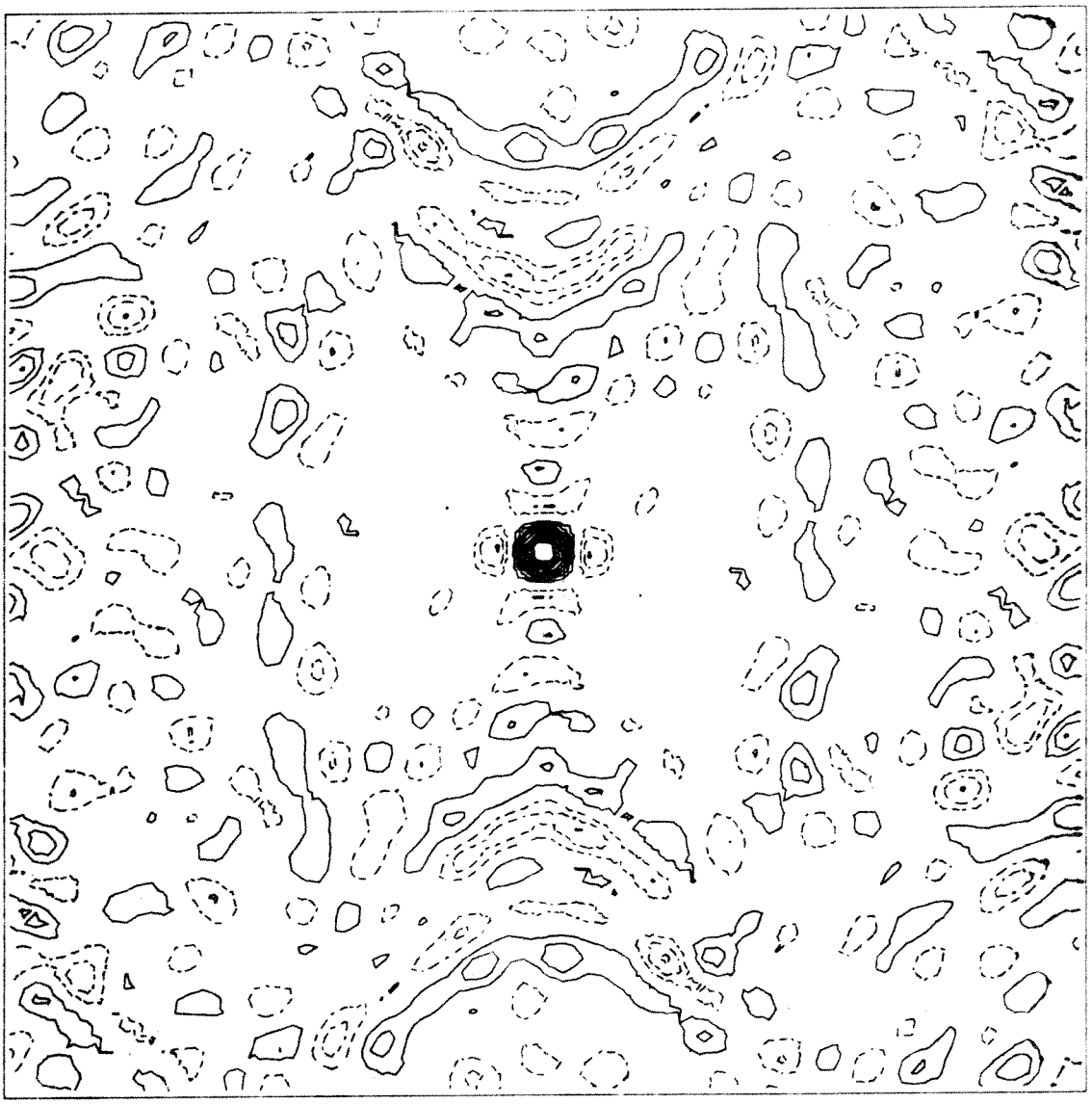

Fig. 2-4. Typical "dirty-beam" pattern. The outer square is 84' on a side. Contour interval is 10% of the maximum. Zero contour is omitted; negative contours are dashed.

equal to the width of the primary response in the so-called "dirty" beam (Figure 2-4). A computer program searches the synthesized map for the highest point, then subtracts over the whole map a dirty beam pattern centered on that point, of amplitude equal to half that maximum value. The coordinates and amplitude are stored, and the remaining map is again searched. The procedure is repeated until a designated level of brightness temperature is reached. The program then adds back to the residual map a set of gaussian components with coordinates and amplitudes given by the "dirty" components previously removed.

An implicit assumption in the procedure is that the sidelobe structure of the dirty beam is independent of the position of the point source in the synthesized field. That this is true is easily demonstrated. For a point source of unit flux density, located at (x_o,y_o), the fringe amplitude, F , is unity and the phase is

$$\phi = -2\pi(ux_o + vy_o)$$

Substituting into equation (2.2) we have

$$T(x,y) = K \sum_{j=1}^{N} w_j \cos(2\pi(u_j(x-x_o) + v_j(y-y_o))) ,$$

which is simply the expression for the response to a point source at the origin, but translated to a center (x_o,y_o). It should be noted that other inversion schemes, such as smoothing the data to a regular grid, involve a nonlinear transformation on the data which invalidates the assumption of identical beam patterns, independent of position in the map.

Chapter 3

RESULTS

The Cleaned Maps

The maps of brightness temperature, after inversion and cleaning, consist of 40×40 arrays of numbers, each value being the brightness temperature at the corresponding point in the sky. The 1600 points in the map lie on a square grid with a grid interval of one minute of arc between points. An inverted and cleaned map was produced for each channel of all five velocity shifts for the two sources Sgr A and Sgr B2. (One of the filter banks developed a severe instability, finally traced to a bad solder joint, late in the observational program. Although the bad data in these channels were thrown out, evidently there were enough undetected bad points in the data for the -187 km/s velocity range to make the last eleven channels useless. Fortunately, the other four velocity shifts were found to be satisfactory.) The total number of cleaned maps for the two sources, then, is 458, ranging in velocity from +100 km/s to -200 km/s (instead of -225 km/s as originally planned.)

Perhaps the most obvious method of examining the data is to compare contour maps of the various narrowband channels. It will quickly be obvious, however, that not much information can be obtained by this means. The Sgr A maps are completely dominated by the bright central source, since the interferometer does not respond to the extended component, even at the closest spacing. (The extended component of the galactic center complex has dimensions at half-maximum intensity

of about $0^{o}.4$ in galactic latitude and $1^{o}.0$ in longitude [Lequeux 1967]. At an antenna separation of 150 wavelengths, a gaussian of half-power diameter $0^{o}.4$ has a normalized visibility of less than 0.02.) Sample contour maps of brightness temperature for Sgr A are presented in Figure 3-1. The center of the map is at the coordinates for Sgr A given by Maxwell and Taylor (1968): R.A.(1950) = $17^{h}42^{m}30^{s}.7$, Decl.(1950) = $-28^{o}59'12"$. North is up and east is to the left. The velocity given is for the center of the narrowband channel; the contour interval for this figure is 10% of the maximum brightness. The zero-level contour is omitted. The diagonal line represents the galactic equator, with a tick mark at $l = 0^{o}.0$. Figure 3-1(a) is a map of the continuum source and was obtained by averaging the four highest-velocity channels of the +65 km/s shift. In the velocity range of these four channels, namely +96.12 km/s to +100.44 km/s, the Sgr A region is known to be clear of OH absorption (Robinson and McGee 1970). The circle on the continuum map shows the synthesized beam size at half-maximum.

On the continuum map, in addition to the main component, Sgr A, a weak feature 10' north is present. This is the discrete source G0.1+0.0 which also appears on high-resolution single-dish maps at 8.0 GHz (Downes and Maxwell 1966) and 15.4 GHz (Lequeux 1967). A second discrete source, G0.2-0.0, which lies at the edge of the map, is not visible because it lies too far down on the primary beam to have a brightness temperature above the lowest contour interval. The maps presented in this section have not been corrected for the primary

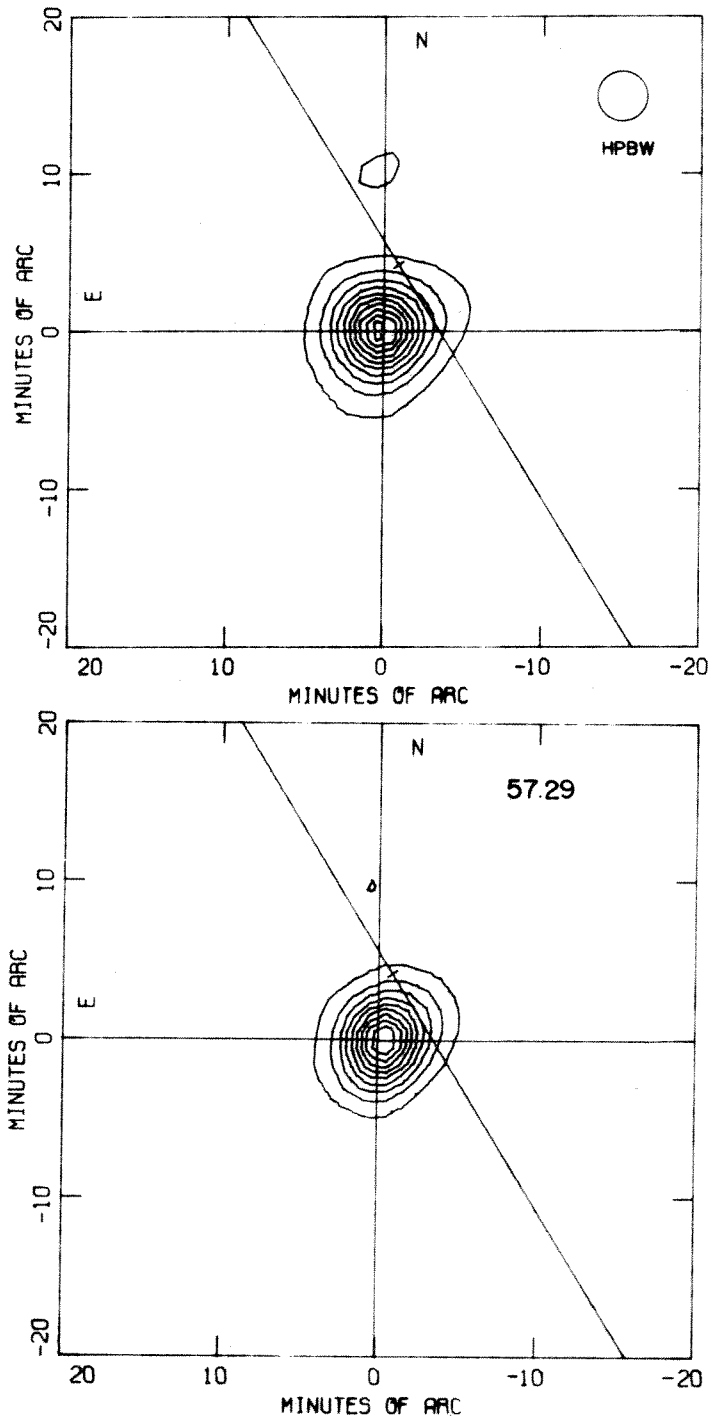

Fig. 3-1. Sample brightness distributions for Sgr A. Velocity in km/s in the upper right. Contour interval is 10%, zero omitted. Upper map: continuum, $T_B(max) = 1900K$; Lower map: $T_B(max) = 1380K$.

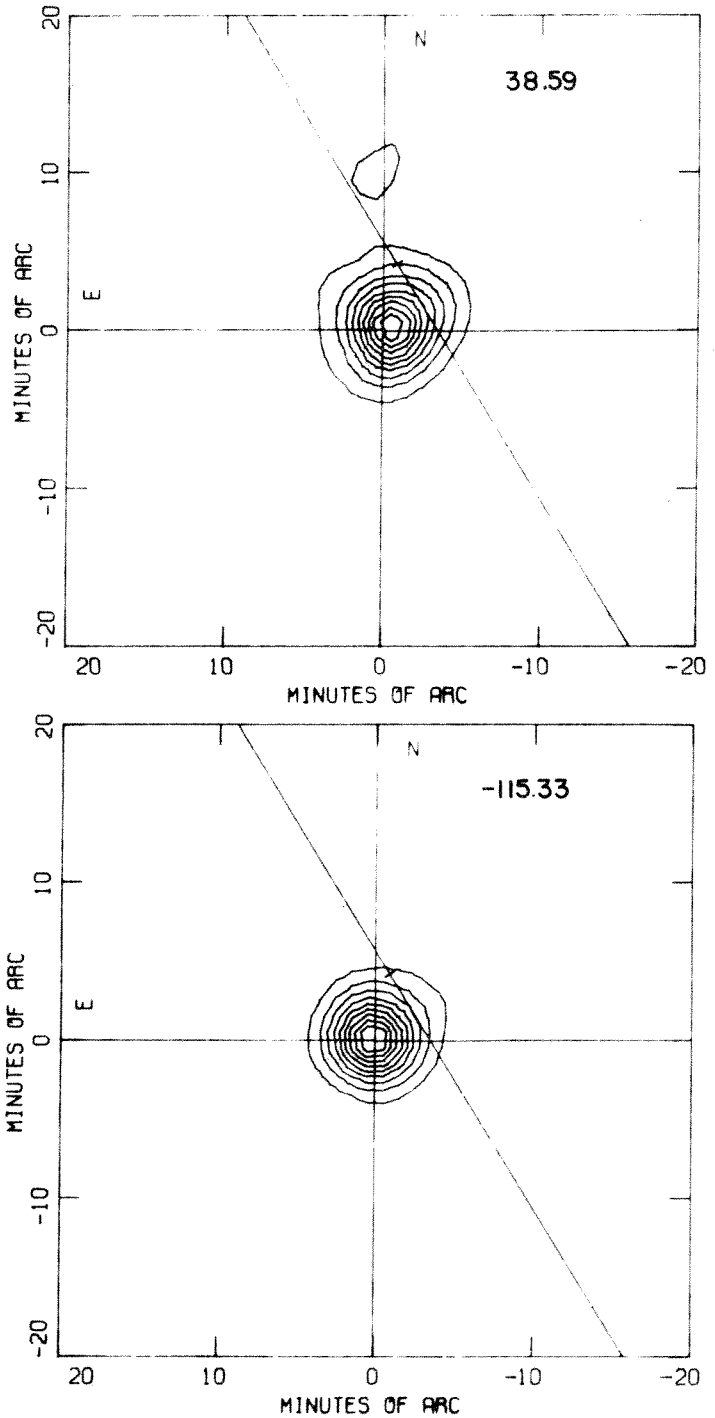

Fig. 3-1 (cont.) Upper map: $T_B(max)$ = 1090K. Lower map: $T_B(max)$ = 1795K.

beam response of the 90-foot antennas. Such a correction was applied to the Sgr A continuum map, which then showed the G0.2-0.0 source as a discrete feature. However, the noise at the edges of the maps is greatly magnified by the primary beam correction, so that the size and shape of this weak feature are distorted.

Examination of these maps shows how difficult it is to estimate the characteristics of the absorbing gas from the brightness temperature maps alone. Even in the deepest part of the most prominent absorption line, at a velocity of +38.59 km/s, where the peak brightness is reduced to 57% of the continuum value, there is little change in the appearance of the map. The peak has shifted slightly north and west, and the outer contours are slightly distorted, but there are no striking differences between the continuum and any of the other maps, aside from the changes in peak brightness temperature.

The maps of Sgr B2 show a good deal more structural changes with velocity, but even so, little detailed information on the absorbing clouds can be obtained from these maps alone. Figure 3-2 is a sample similar to that for Sgr A. The continuum map here is an average of five channels at the extreme low velocity end of the spectrum, from -197.31 km/s to -203.07 km/s. Robinson and McGee (1970) show that in the longitude range near $l = 0^{\circ}.7$ there is no detectable absorption for this range of velocities. For the Sgr B2 maps, the origin of coordinates is at R.A. = $17^{h}44^{m}18^{s}.5$, Decl.(1950) = $-28^{\circ}24'00''$. The tick mark in the galactic equator is at $l = 0^{\circ}.7$. These maps of the Sgr B2 region encompass three discrete sources known from high resolution

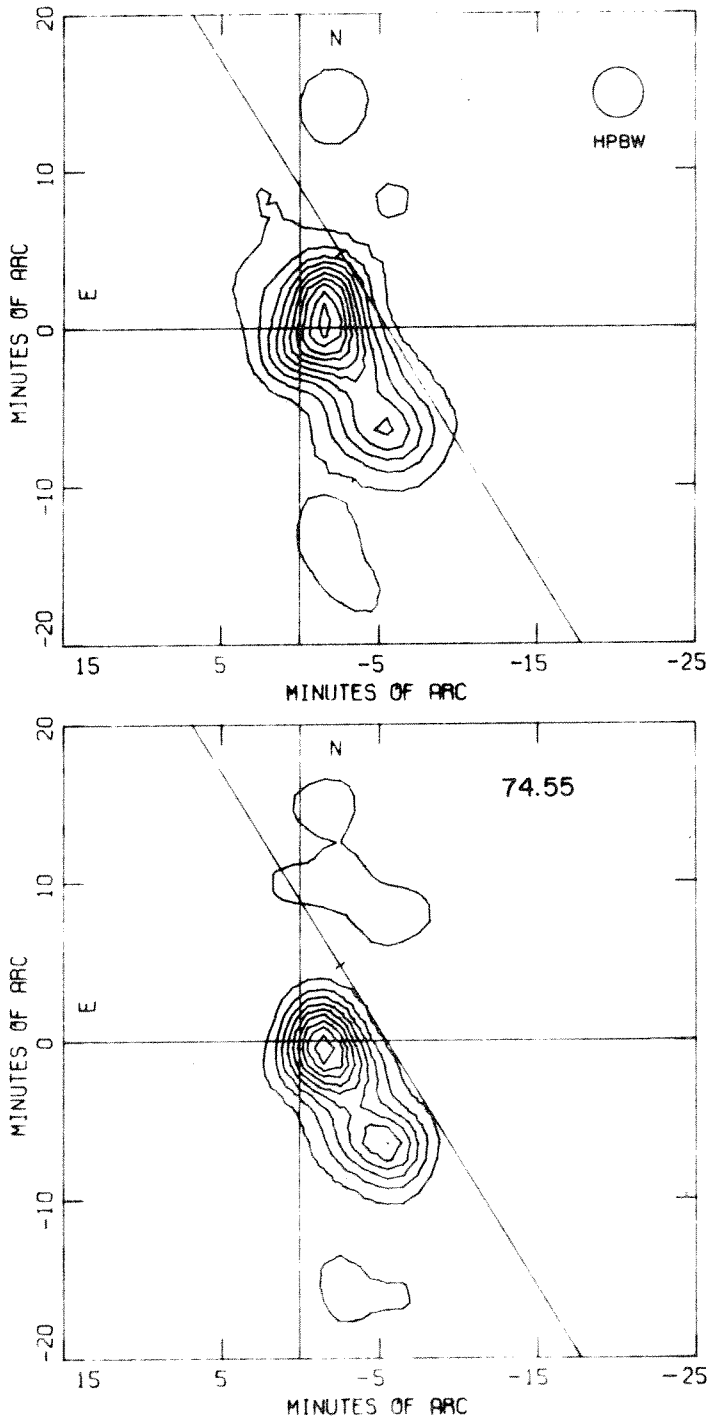

Fig. 3-2. Sample brightness distributions for Sgr B2. Velocity in km/s in the upper right. Contour interval is 10%, zero omitted. Upper map: continuum, $T_B(max)$ = 153K. Lower map: $T_B(max)$ = 114K.

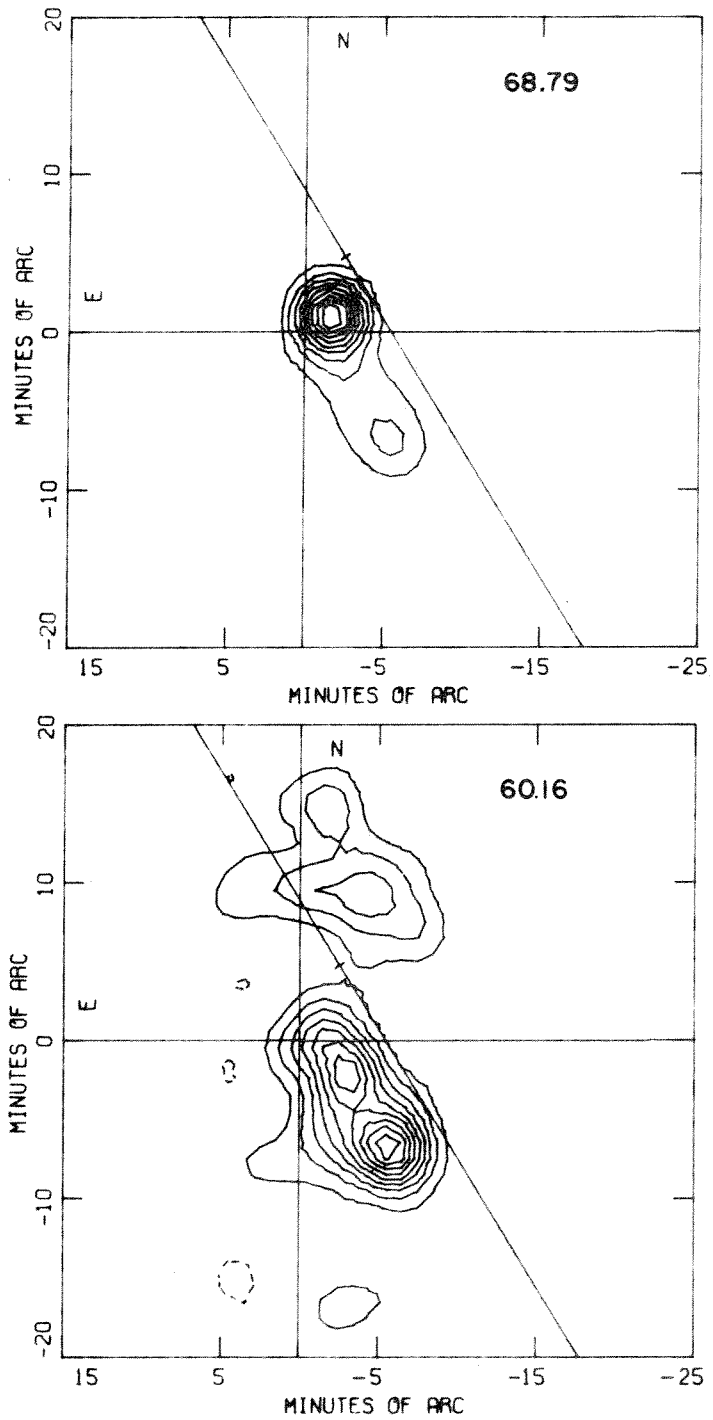

Fig. 3-2 (cont.) Upper map: $T_B(max)$ = 254K. Lower map: $T_B(max)$ = 63K.

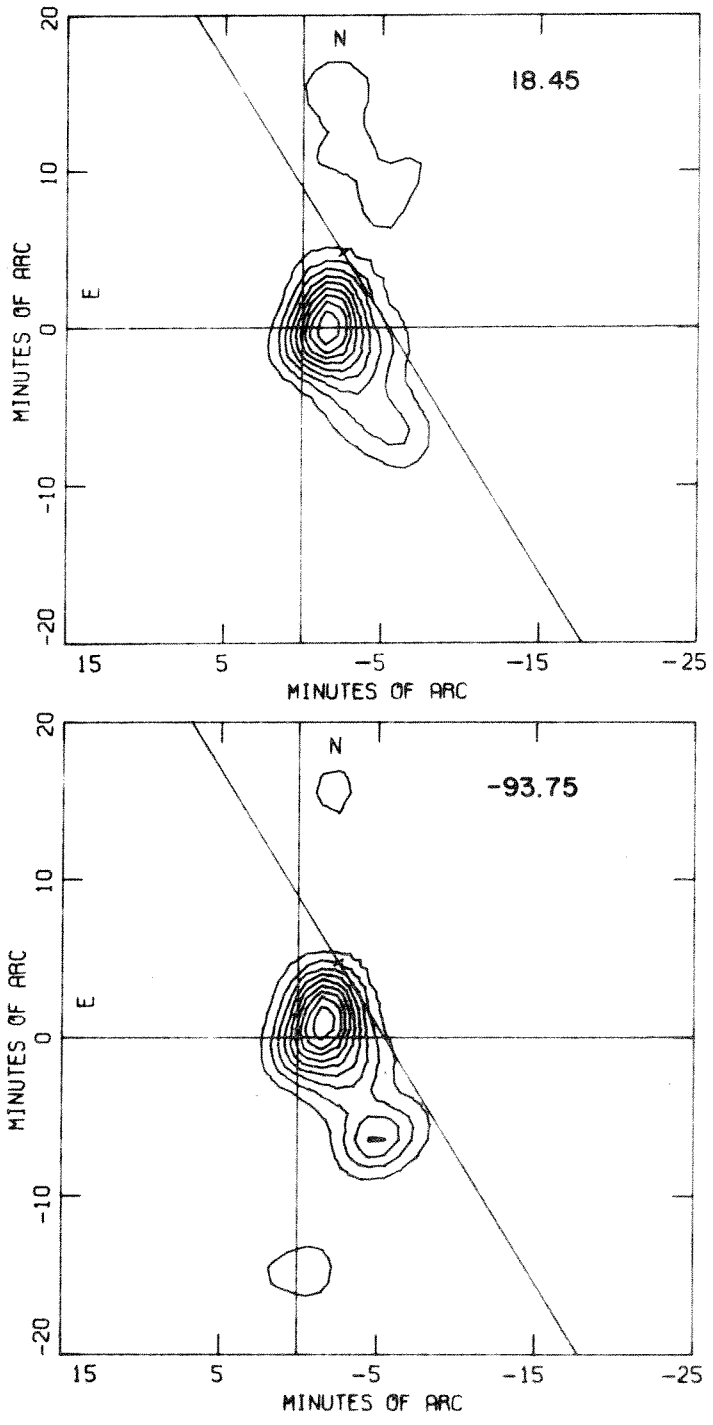

Fig. 3-2 (cont). Upper map: $T_B(max)$ = 129K. Lower map: $T_B(max)$ = 130K.

single dish maps. The stronger two sources, G0.5-0.0 and G0.7-0.0, are the prominent features near the center of the map, while the other, G0.9+0.1, lies some 14' north of G0.7-0.0 and is much weaker. The rather large, elongated contour at the 10% level to the south of the main sources does not correspond to any previously mapped radio source. It may be a spurious feature due to some systematic effect which was interpreted to be real by the cleaning procedure.

Comparison of the continuum and the narrowband brightness maps reveals some significant absorption effects. At +74.55 km/s, the source G0.5-0.0 shows relatively little absorption, while the brightness temperature of G0.7-0.0 is reduced by 25% of its continuum value. Also, the peak has shifted south and a little west, indicating a strong absorption in the north-east part of G0.7-0.0. What appears to be an extended region of emission at a temperature of about 12 to 15K lies just south of G0.9+0.1. At the velocity +68.79 km/s, the map is dominated by a point-like source slightly north of the peak of G0.7-0.0. This position and velocity coincide with the known maser emitter at 1667 MHz (Raimond and Eliasson 1969). At +60.16 km/s, the G0.5-0.0 source is stronger than G0.7-0.0, whose peak brightness has now shifted farther south and west, indicating even greater absorption. The extended emission south of G0.9+0.1 has a maximum brightness temperature of about 20K and an angular size of 7' × 14'. The +18.45 km/s map shows an absorption of 68% on the peak of G0.5-0.0, while G0.7-0.0 at this velocity has only about 15% absorption. The extended emission is reduced in size, and its greatest brightness is about 15K. Finally,

.he sample map at -93.75 km/s resembles the continuum except that the naximum brightness is 15% lower, the intensity of G0.5-0.0 is relatively lower than the continuum, and the lowest-level contours are somewhat distorted. But detailed conclusions cannot be made solely on the basis of a simple visual comparison of these maps, so we must turn to other means of analysis.

The basic data of this investigation are the brightness temperatures as a function of three independent variables: The two position coordinates and the velocity. Two methods of presenting the data are thus suggested. We may plot brightness temperature as a function of velocity for a fixed position in the sky, or we may plot contours of the brightness temperature in the position coordinates for a fixed velocity. The second of these has been shown to be fairly unenlightening. However, by normalizing the brightness in the line to that in the continuum, substantially more information can be obtained from contour maps at constant velocity. In fact, the method used will plot contours of optical depth against the position coordinates.

Plots of the spectra of brightness temperature against velocity, for selected positions in the map grid, are useful in determining the number, velocities, and velocity dispersions of the absorption components at those positions. The spectra also allow an accurate estimate of the noise level at the map position. The continuity of the spectra across the five frequency shifts is a means of checking for any systematic errors in the calibration of the narrowband channels from one shift to the next. Such systematic effects are important in

estimating the uncertainty in the optical depth maps, where the continuum level is in one frequency shift while the absorption lines may be in one of the others. Any systematic differences between frequency shifts may produce discontinuities in the calculated optical depths as a function of velocity. As will be seen, such discontinuities may become significant near the edge of the sources, where the continuum level is low. It is difficult to deduce the size and structure of the absorbing clouds solely on the basis of spectra at selected map points. The maps of optical depth are useful in this respect, since they delineate the size and structure of the absorption features at a given velocity. Comparison of the maps for different velocities shows how the absorption changes with velocity, hence providing some insight into the kinematics of the molecular clouds.

Spectra at Selected Grid Points--Sgr A

In this section we examine the OH absorption spectra for selected points in the map of Sgr A. It is useful to compare the results of the synthesis observations with the OH spectrum measured by a single antenna. The 130-foot paraboloid of the OVRO was used with the 100-channel autocorrelation receiver (described by Riegel 1966) to obtain low-noise spectra of the 1667 MHz line for both Sgr A and Sgr B2. The spectra were measured by a total power technique with the antenna pointed at the continuum peaks of G0.0-0.0 (Sgr A) and G0.7-0.0 (Sgr B2). The "off" observations were taken at a position 15 minutes east in right ascension of the "on's". The 2.5 MHz bandwidth was used,

for a frequency resolution of 25 kHz. The data were given uniform (rather than cosine) weighting, resulting in a velocity resolution of 5.4 km/s. The calibration of the flux density scale was done by measuring the antenna temperature of Virgo A, which was assumed to be a point source with a flux density of 185 f.u. The conversion from antenna temperature to flux density for the spectra used Crutcher's (1972) measured value of 3.9 f.u./K. The absolute accuracy of the flux calibration is believed to be better than 10%. The beamwidth of the 130-foot antenna is 18' at a frequency of 1667 MHz, so each spectrum represents the absorption line integrated over a region approximately 18' in diameter, weighted by the primary beam response.

Figure 3-3 is the resulting spectrum for Sgr A. It shows five major features. Centered at +38 km/s is the deepest component, with a width at half-maximum of 62 km/s. A second broad feature has its maximum absorption at -132 km/s and has a width of 64 km/s. Three smaller, narrower components are also obvious at -2, -30, and -53 km/s. The velocity widths of these features at half-maximum are 11, 5 and 6 km/s, respectively. A weak blended component is evident in the low velocity wing of the -135 km/s feature, extending at least from -170 to -230 km/s. The -135 km/s feature is also markedly asymmetrical, suggesting that it may itself be a blend of two components. Finally, the region from -60 km/s to -80 km/s shows evidence for weak absorption, although the proximity of the strong line at -135 km/s distorts the shape of the weaker feature.

From this spectrum we can calculate the apparent opacity of the five features, where the apparent opacity is defined as the ratio of

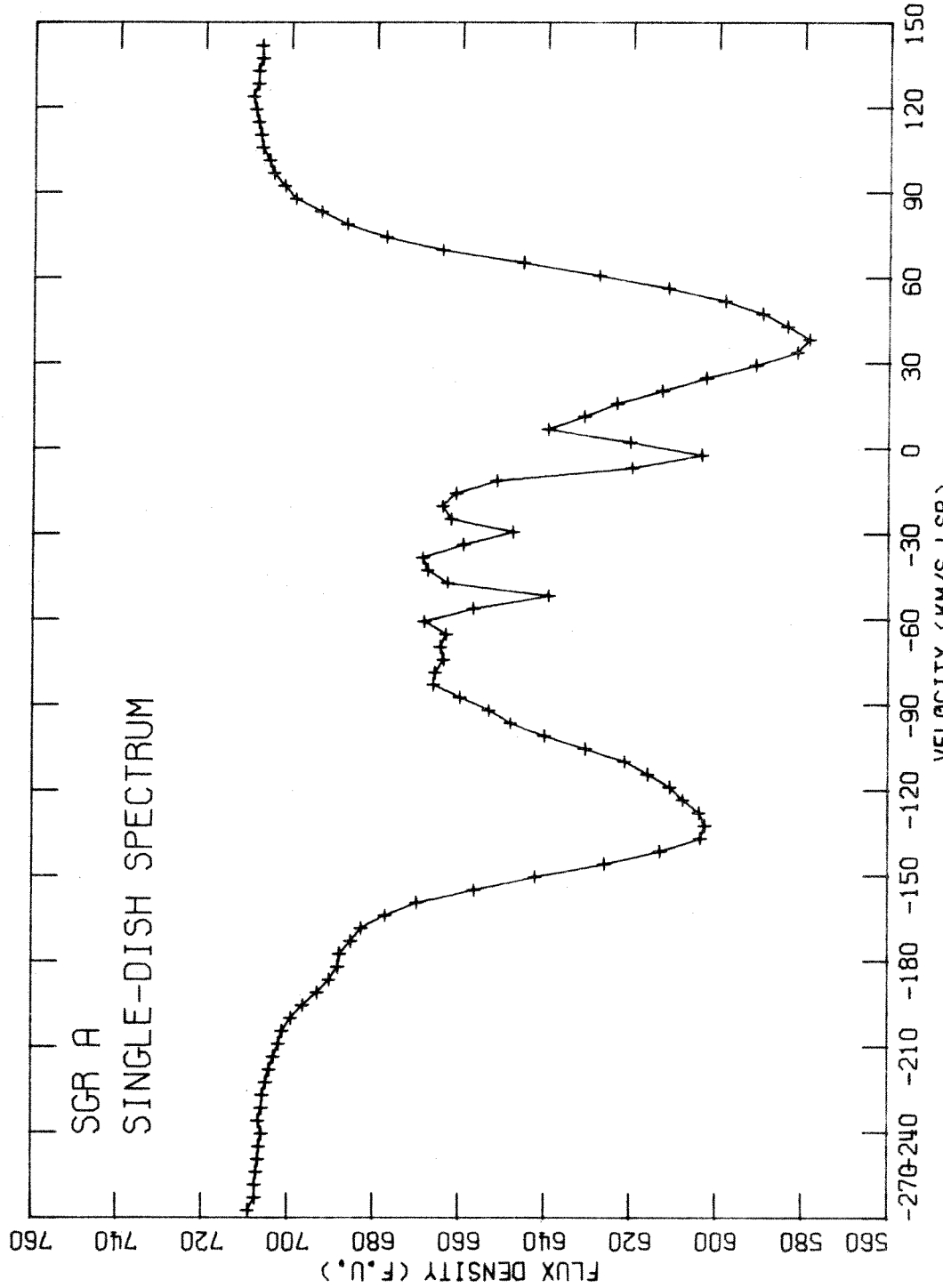

Fig. 3-3. Sgr A 1667 MHz absorption spectrum obtained with 130-foot telescope and 100-channel autocorrelator.

the maximum flux removed by the absorption line to the (estimated) flux of the continuum at that point. For the two broad features, the continuum flux is assumed to be that of the ends of the profile at 707 f.u. For the three narrow features, the assumed continuum level is the extrapolation of the wings of the broad, deep lines. (This extrapolation implies that the narrow features arise between the Sun and the clouds at +40 and -135 km/s.) Table 3-1 summarizes the data for the five main features of the single-dish spectrum. The first two columns give the velocity of maximum absorption and the width at half-maximum. The third and fourth columns give the maximum flux removed by the absorption line, and the assumed continuum flux level for that feature. The last column is the apparent opacity, which is the ratio of columns 3 and 4.

Table 3-1

Summary of Single-Dish Spectral Features--Sgr A

V_o (km/s)	$\Delta V_{1/2}$ (km/s)	S_{line} (f.u.)	S_{cont} (f.u.)	Opacity
38	62 ± 5	130 ± 3	707	0.184 ± 0.02
-2	11 ± 3	45 ± 5	647	0.070 ± 0.01
-30	5 ± 2	18 ± 2	666	0.027 ± 0.005
-53	6 ± 2	28 ± 3	667	0.042 ± 0.006
-132	64 ± 5	106 ± 2	707	0.150 ± 0.02

The locations of spectra for Sgr A which will be presented here are indicated by the numbered points on the continuum map in Figure 3-4, which is used as a key in the following discussion. The fourteen numbered spectra of Figure 3-5 are a representative sample over the map of Sgr A. Spectrum 1 is taken at the grid point nearest the continuum peak. Spectra 2 through 5 are at offsets of 2 arcminutes east, south, west, and north of position 1, and 6 through 12 form a roughly circular pattern near the edge of the continuum source. Number 13 lies slightly south of the continuum, while 14 is at the position of the weak component G0.1+0.0. Each spectrum is a plot of the brightness temperature versus velocity for the specified grid position of the map. The temperature scale is corrected for the primary beam response, assumed to be a gaussian with 24' half-width. Since the grid interval is one arcminute, the spectra represent the average brightness temperature over one square arcminute of the sky. It should be noted that since the diameter of the synthesized beam is 3.25 arcminutes at half-maximum, not all the spectra are completely independent. Pairs of points separated by less than three arcminutes will exhibit some degree of similarity.

Comparison of the first five spectra with that of Figure 3-3 reveals certain notable differences. Most striking is the very large increase in the opacity of the +40 feature, and the relative decrease in opacity of the -132 km/s component. The +40 km/s line width is significantly reduced in the high-angular-resolution spectra. The three narrow features, on the other hand, have the same characteristics

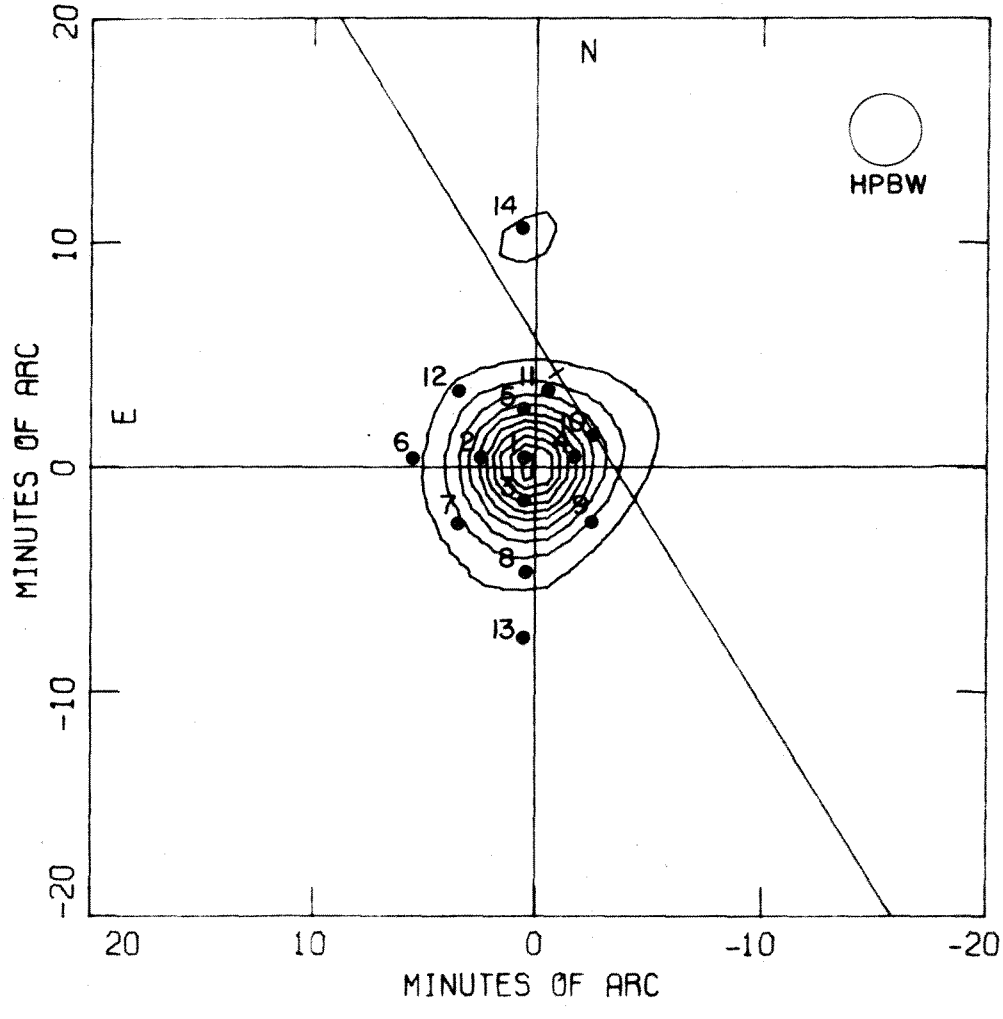

Fig. 3-4. Key to point spectra for Sgr A.

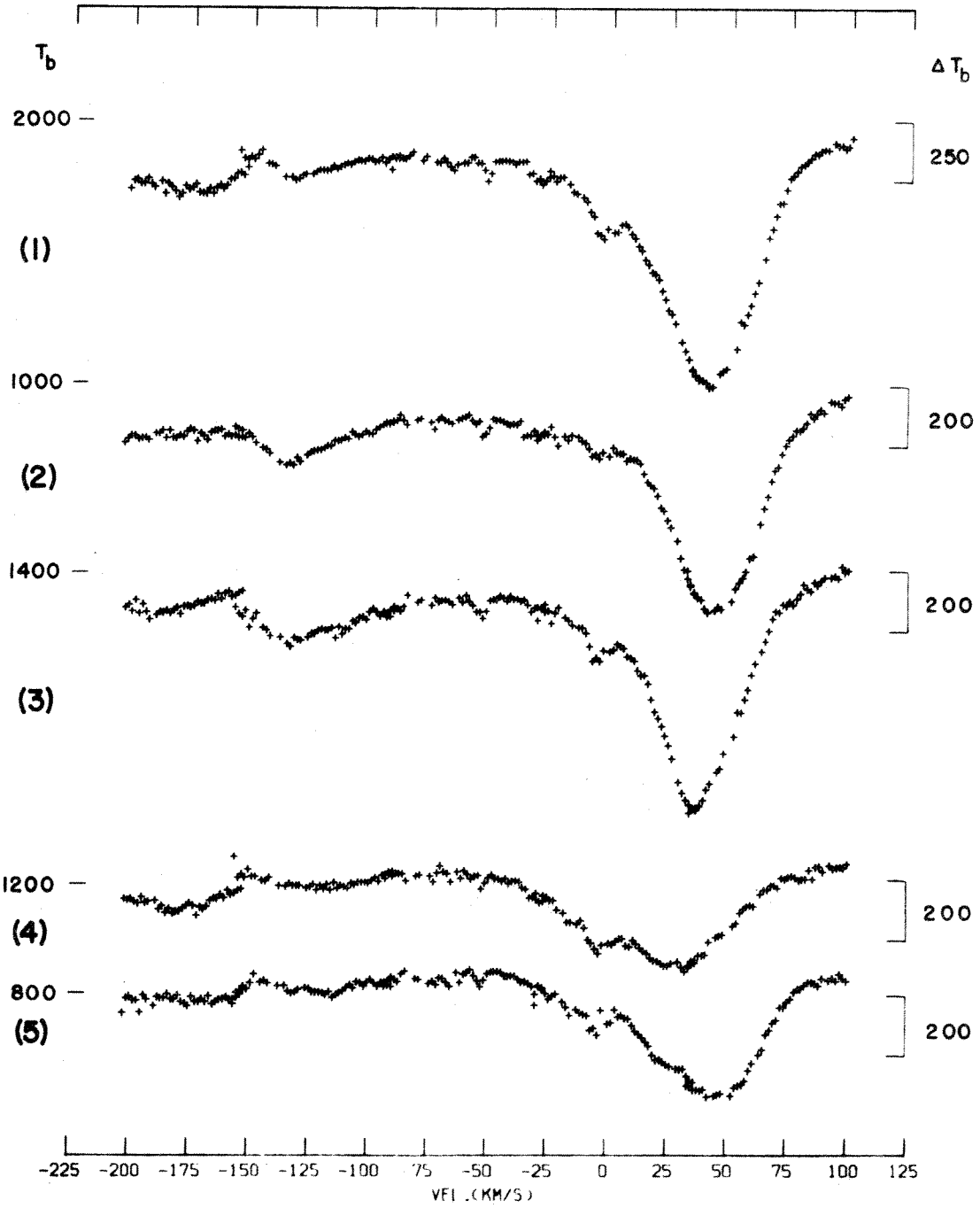

Fig. 3-5. Spectra for selected map points, Sgr A. Numbers in parentheses refer to Fig. 3-4. Brightness temperature level indicated on left, scale on right (both in K). Zeros are displaced.

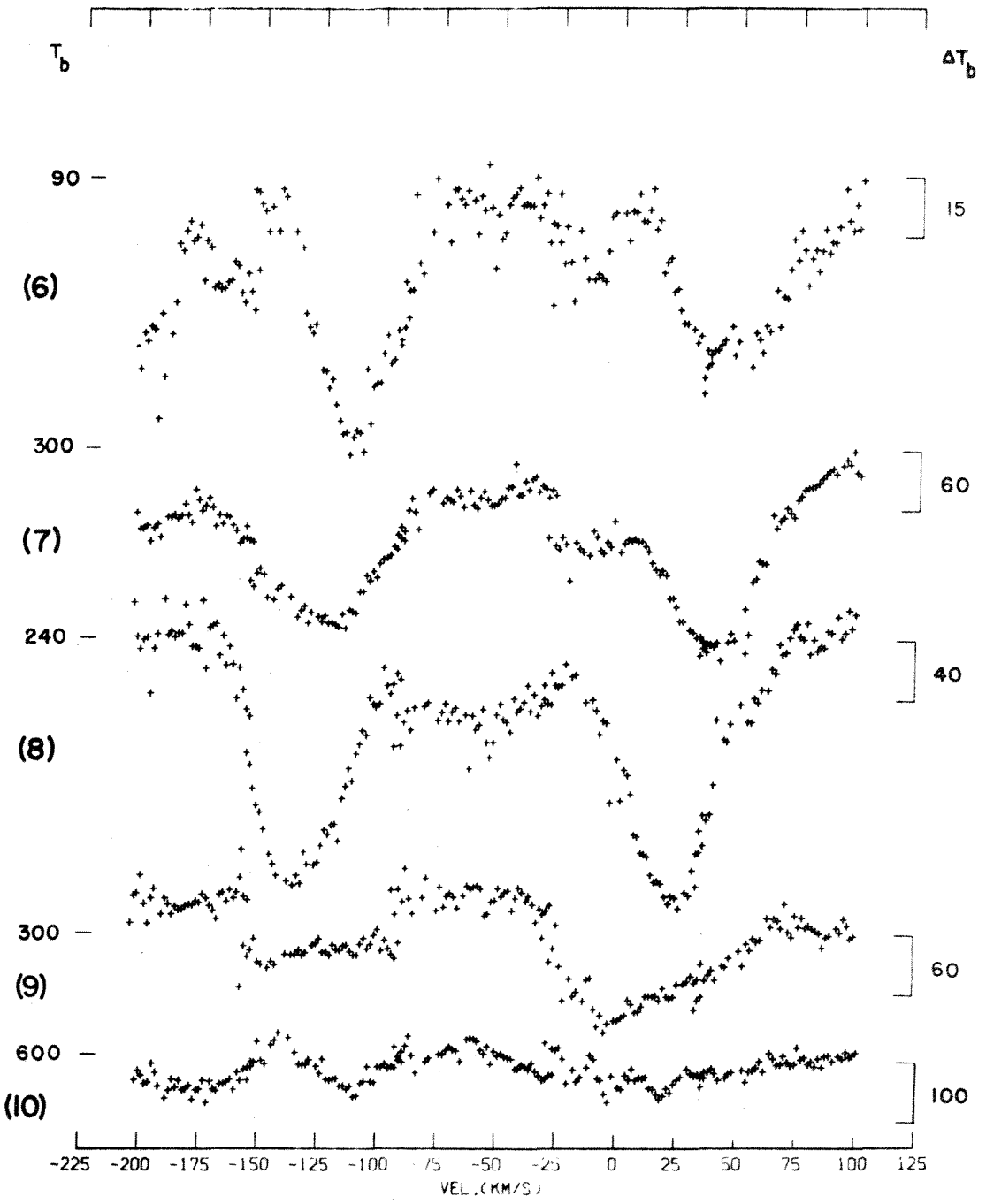
T_b
ΔT_b
90
(6)
15
300
(7)
60
240
(8)
40
300
(9)
60
600
(10)
100
-225 -200 -175 -150 -125 -100 -75 -50 -25 0 25 50 75 100 125
VEL.(KM/S)

Fig. 3-5 (contd.)

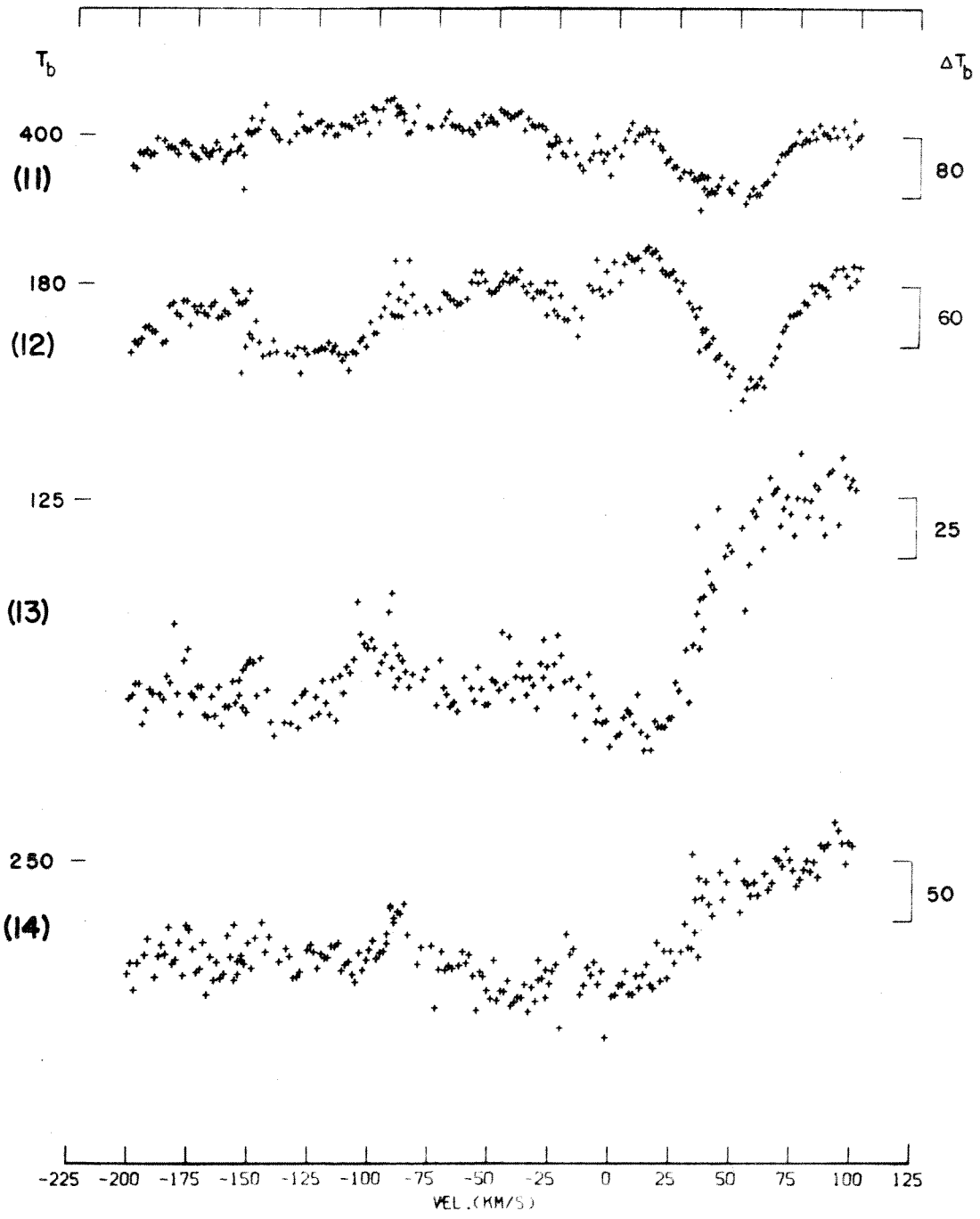
T_b
ΔT_b
400
(11)
80
180
(12)
60
125
(13)
25
250
(14)
50
-225 -200 -175 -150 -125 -100 -75 -50 -25 0 25 50 75 100 125
VEL.(KM/S)

Fig. 3-5 (cont'd.)

as they do in the single-dish spectrum, within the noise level. Measured values for these three components in spectrum 1 (Figure 3-5) are summarized in the following table. The column headings have the same meaning as in Table 3-1.

Table 3-2

Narrow Features of Sgr A, Spectrum 1

V_o (km/s)	$\Delta V_{1/2}$ (km/s)	Opacity
-3 ± 1	10 ± 1	0.05 ± .01
-29 ± 1	5 ± 2	0.04 ± .01
-53 ± 1	3 ± 1	0.07 ± .01

These results agree with those in Table 3-1 to within the uncertainties, which immediately suggests that the absorbing clouds producing the three narrow features are distributed uniformly over the entire continuum source. The +40 km/s cloud, on the contrary, must be concentrated in front of the compact continuum source to account for the large increase in opacity with higher angular resolution. The simultaneous reduction in linewidth suggests a large velocity gradient within the cloud, so that each one-square-arcminute sample spectrum includes only a limited range of velocities within the cloud. This suggestion is confirmed by examining the positional dependence of the peak-absorption velocities. The fourteen sample spectra are summarized in Table 3-3, which lists the right ascension and declination of

Table 3-3

Summary of Major Features--Sgr A Absorption Spectra

Spectrum Number	α_{1950} h m s	δ_{1950} o '	V_o (km/s)	$\Delta V_{1/2}$ (km/s)	Maximum Opacity
1	17 42 33.0	-28 58.7	42(2) -133(5)	48(2) 40(10)	0.54(.02) 0.08(.01)
2	42.2	-28 58.7	43(2) -133(5)	44(2) 50(10)	0.74(.02) 0.23(.03)
3	33.0	-29 00.7	35(2) -133(5)	41(2) 55(10)	0.56(.02) 0.15(.02)
4	23.1	-28 58.7	25(10) -125(10)	70(5) 45(10)	0.28(.02) 0.05(.03)
5	33.0	-28 56.7	50(5) -115(20)	52(2) ?	0.45(.02) 0.07(.03)
6	55.9	-28 58.7	45(10) -112(5)	55(10) 40(5)	0.45(.05) 0.70(.05)
7	46.8	-29 01.7	37(5) -115(10)	46(5) 55(5)	0.64(.05) 0.60(.1)
8	33.0	-29 03.7	25(5) -135(5)	42(5) 45(5)	0.75(.03) 0.70(.05)
9	19.3	-29 01.7	0(10)	55(10)	0.30(.05)
10	19.3	-28 57.7	20(5) -110(10)	? 20(5)	0.1 (.05) 0.12(.05)
11	28.5	-28 55.7	45(10)	42(5)	0.20(.05)
12	46.8	-28 55.7	55(5)	34(5)	0.55(.07)
13	33.0	-29 06.7	< 25	?	0.75(.1)
14	33.0	-28 48.7	?	?	0.45(.1)

each position; the velocities, V_o , at which absorption maxima are found for the two broad components; the velocity width at half-maximum absorption, $\Delta V_{1/2}$; and the maximum opacity, as defined above. The continuum level, as discussed earlier, is assumed to be the average brightness temperature of the four highest-velocity channels. The estimated uncertainties of the tabulated values are given in parentheses. Question marks indicate values which cannot be estimated with any reasonable certainty.

From these data, the run of velocity with position for the +40 km/s feature can be discerned. The absorption has its maximum at higher velocities in the north-east quadrant, tending to lower velocities in the south-west. Spectra 4 and 9 indicate that a second component exists, peaking near zero velocity. This component would account for the anomalously large velocity widths, and the irregular shapes of the profiles in the south-west quadrant. The spectra also clearly show that the absorbing cloud (or clouds) is concentrated below the galactic plane, and diminishes in opacity to near zero at the northwest edge of the continuum. This gradient in opacity is very steep, as comparison of spectra 4 and 10, and 5 and 11, demonstrates.

The difficulties encountered in constructing a complete absorption spectrum by setting down the filter banks at five different local oscillator offsets are shown in spectra 6, 7, 8, 9, and 12. At these positions, the continuum level is between 10% and 20% of the maximum. Systematic differences in the five narrowband calibrations appear as discontinuities in spectra where the filterband settings overlap. (Note

that the three end channels should agree at each of the four points of overlap.) These discontinuities change from point to point on the maps, making it virtually impossible to take them out by any "baseline removal" technique. The discontinuities are almost always less than 2% of the continuum maximum, or less than about 40K in brightness temperature. For positions where the continuum is large (e.g., spectra 1-5, 10, and 11) the discontinuities are negligible. Only near the edges, where the continuum is down to 10% of its maximum, does the effect become important. This caveat should be remembered when examining the contour maps of optical depth to be presented shortly.

The spectra for Sgr A show that the component at -135 km/s is situated to the south and east of the central source. There is a slight indication that the velocity of maximum absorption becomes more negative with decreasing galactic longitude, but such a conclusion must be regarded with caution. Spectra 6, 7, and 8 demonstrate clearly that the opacity of the -135 absorption line is comparable to the +40 km/s line on the southeast of the continuum. The deep negative-velocity component of the single-dish spectrum can be attributed to extended regions of high optical depth concentrated south in latitude from Sgr A.

The weak blended feature between -170 km/s and -230 km/s visible in the single-dish spectrum may correspond to the feature present in spectra 1 through 5 at velocities less than -150 km/s. The apparent absorption cannot be attributed to a discontinuity at -155 km/s, since the agreement across the velocity-shifts is good. Moreover,

the absorption has the appearance of a separate component. (Spectrum 6 shows absorption at -200 km/s, but the signal-to-noise ratio is too poor to allow any definite conclusions.) Tentatively, then, a separate absorption feature is identified in the velocity range -155 km/s to -200 km/s, with an opacity of about 0.1 at the most, and centered approximately on the continuum peak.

Maps of Optical Depth--Sgr A

It is impossible to determine accurately the true optical depth of the ground-state absorption lines of OH using single-dish observations. The molecular condensations are so small compared to the size of the antenna beam and, often, of the continuum source, that the beam filling factor cannot be estimated with any precision. To further complicate the situation, the greatest density of OH molecules may be located on the edge of the continuum source. A single-dish spectrum will, in this case, grossly underestimate the opacity of the absorber, since such a spectrum is strongly weighted in favor of the brightest part of the continuum, the low-brightness regions contributing only a little to the line antenna temperature. Turner (1972) has discussed these problems, and because of the uncertainties in all the crucial parameters, is forced to use the apparent opacity, defined as

$$\langle\tau\rangle = \frac{T_{AL}}{T_{AC} + 3}$$

where T_{AL} is the line antenna temperature, T_{AC} is the antenna temperature of the background continuum, and the term 3 includes the

contribution of the isotropic 3K background. Robinson and McGee (1970) use a similar definition for their observations with the 210-foot antenna at Parkes. Although the situation is more favorable for the smaller primary beam of the large antenna, the problems just mentioned still lead, in some cases, to substantial underestimates of the line opacity.

With the relatively high angular resolution of the present work these difficulties are much less important, because the synthesized beam is small enough to resolve the individual OH clouds in many cases. We may write the solution to the equation of transfer as follows:

$$T_{NB} = F[T_c + R(T_s - T_c)(1 - e^{-\tau})] \qquad (3.1)$$

where

T_{NB} = observed brightness temperature of the narrow-band channel;

T_c = brightness temperature of the background continuum source;

T_s = excitation temperature of the molecular transition;

F = fraction of the synthesized beam covered by the continuum source;

R = fraction of continuum covered by the absorbing cloud;

τ = optical depth of the cloud.

Here the simplest case is assumed: A continuum source of uniform brightness, partially covered by a cloud of uniform optical depth, with no continuum emission arising between the cloud and the observer. We may solve for the optical depth:

$$\tau = \ell n\left[\frac{R(T_c - T_s)}{(T_{NB}/F) - T_c(1-R) - RT_s}\right] . \qquad (3.2)$$

In the case where the synthesized beam resolves both the continuum source and the absorbing cloud, R and F are equal to unity. Then we have

$$\tau = \ell n[\frac{T_C - T_S}{T_{NB} - T_S}] \qquad (3.3)$$

It is known from several kinds of high resolution observations (lunar occultations, high-frequency single-dish maps, interferometry) that the main components of the discrete galactic center sources are not smaller than about three minutes of arc in linear dimensions. The resolution of the synthesis maps presented here is 3'.25 (FWHM), so it is entirely reasonable to set the factor F equal to unity. The filling factor R , however, is unknown. In analyzing the data, R has also been set to unity, the simplest assumption that can be made. The resulting optical depth maps will show whether this assumption is valid, if the typical cloud sizes are larger than the synthesized beam area. If the cloud sizes are comparable to one beam area, the clouds are presumably not completely resolved.

The excitation temperature of the 18-cm OH transitions is a matter of some doubt. The lack of OH emission at 1667 MHz, except in dark clouds, indicates that T_S is generally very low throughout the galaxy (Turner 1970). The extensive survey of the galactic center region at 1667 MHz by Robinson and McGee (1970) found no emission greater than 2K antenna temperature. In the present analysis, T_S is assumed to be negligible compared to the continuum brightness temperature. In the case of Sgr A such a condition is certainly true.

For Sgr B2, at the edges of the continuum source, it is not impossible that T_s might approach the value of T_c, particularly if particle densities are large. The excitation mechanism discussed by Goss (1968) leads to a value of $T_s = 100\,K$ for a gas kinetic temperature of 100 K and a total particle density of $10^3 cm^{-3}$. Under such conditions one could expect to observe emission against the continuum background. However, the gas temperature within dense molecular clouds is most probably much less than 100 K. The excitation mechanism considered by Goss (collisions with charged particles) is probably not dominant in this case, so that considerably lower values for T_s are likely. We will assume that T_s is negligible compared to the brightness temperatures. Equation 3.3 then becomes:

$$\tau = \ell n\left[\frac{T_c}{T_{NB}}\right] \qquad (3.4)$$

This is the relationship on which the optical depth maps are based.

In determining the brightness temperature of the sources, it must be remembered that the interferometer does not respond to the extended background component, as discussed above. Thus, the zero-level away from the continuum sources actually corresponds to some positive brightness temperature, which must be added to the maps. The value of this additive constant is small, relative to the continuum peaks, but is not well determined, unfortunately. From data in Lequeux (1967) and Downes and Maxwell (1966), the best estimates of the added continuum levels are 60 K for Sgr A and 7 K for Sgr B2. These numbers may be uncertain by as much as 30%. This uncertainty will not significantly affect the calculated optical depths except for very

large opacities, in which case the noise in the maps is the dominant source of error anyway.

A representative sample of the optical depth maps for Sgr A is given in the 25 contour plots of Figure 3-6. The general format of these maps is the same as that of the brightness temperature maps presented earlier. The area of each map is reduced to a region $20' \times 30'$, with the origin of coordinates as given above. The zero-level contour is darkened, and negative contours are dashed. The calculation of the optical depth is cut off at the 8% level of the continuum peak. The polygonal figure surrounding the contour map delineates the 8% cutoff level. (The square corners simply reflect the one-arcminute grid interval.)

Examination of these maps reveals the spatial characteristics of the absorption features previously seen in the spectra at individual map points. The most important of these is the +40 km/s line, which shows up in the maps as an elliptical cloud elongated primarily along the galactic plane, with a peak absorption which moves uniformly from higher to lower galactic longitude as the velocity decreases toward zero. At about +35 km/s the cloud breaks up into two components, one of which becomes the dominant feature and moves beyond the continuum boundary. The other component remains at about the same position through the range of velocities at which it is visible as a separate feature.

The data for the +40 km/s feature are summarized in Table 3-4, which also contains measurements from other maps at velocities between

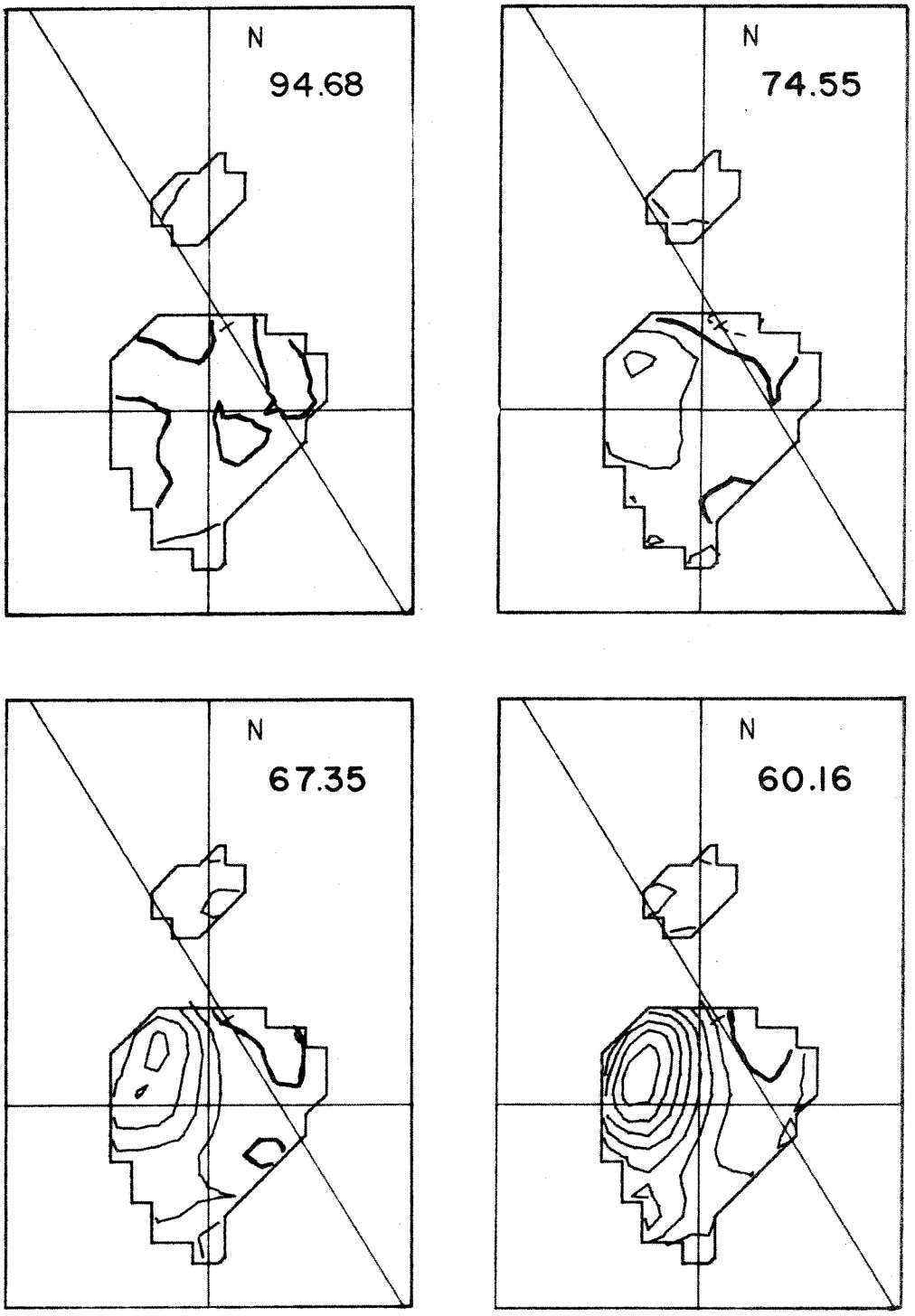

Fig. 3-6. Contour maps of optical depth for Sgr A. Velocity in km/s of each map is in the upper right. Zero contour darkened. Contour interval is 0.10.

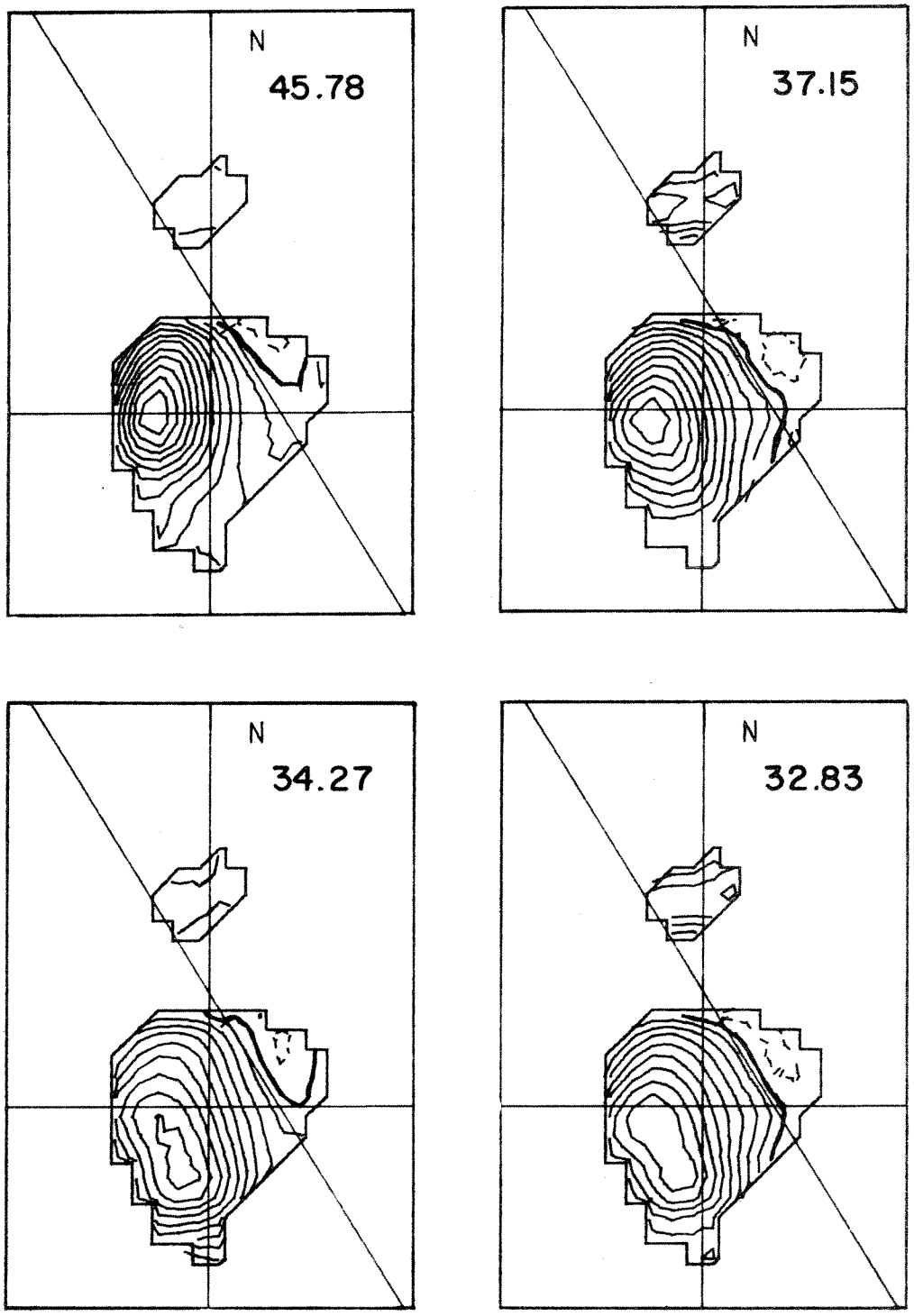

Fig. 3-6 (cont'd.) Contour interval is 0.10

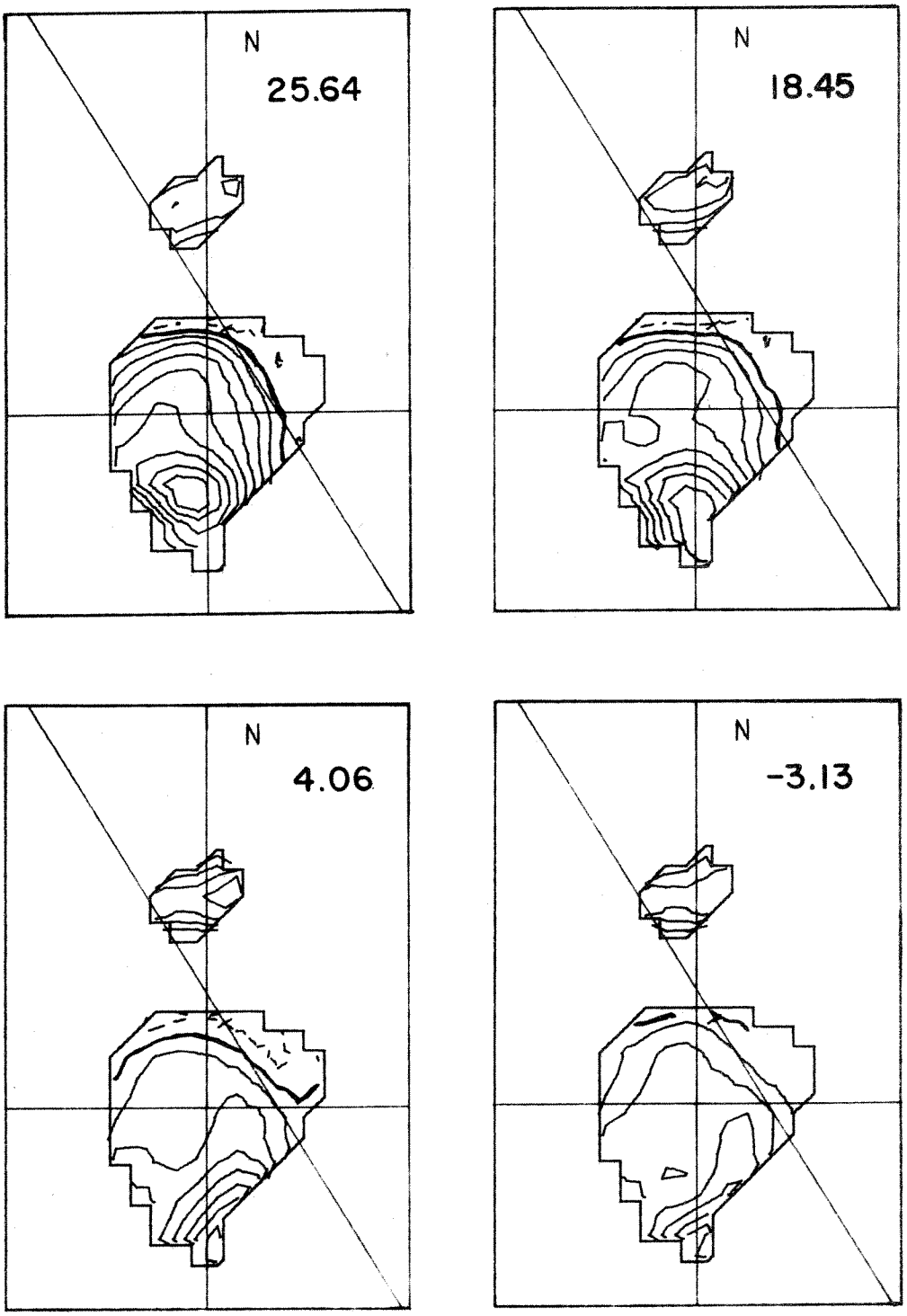

Fig. 3-6 (cont'd.) Contour interval is 0.10

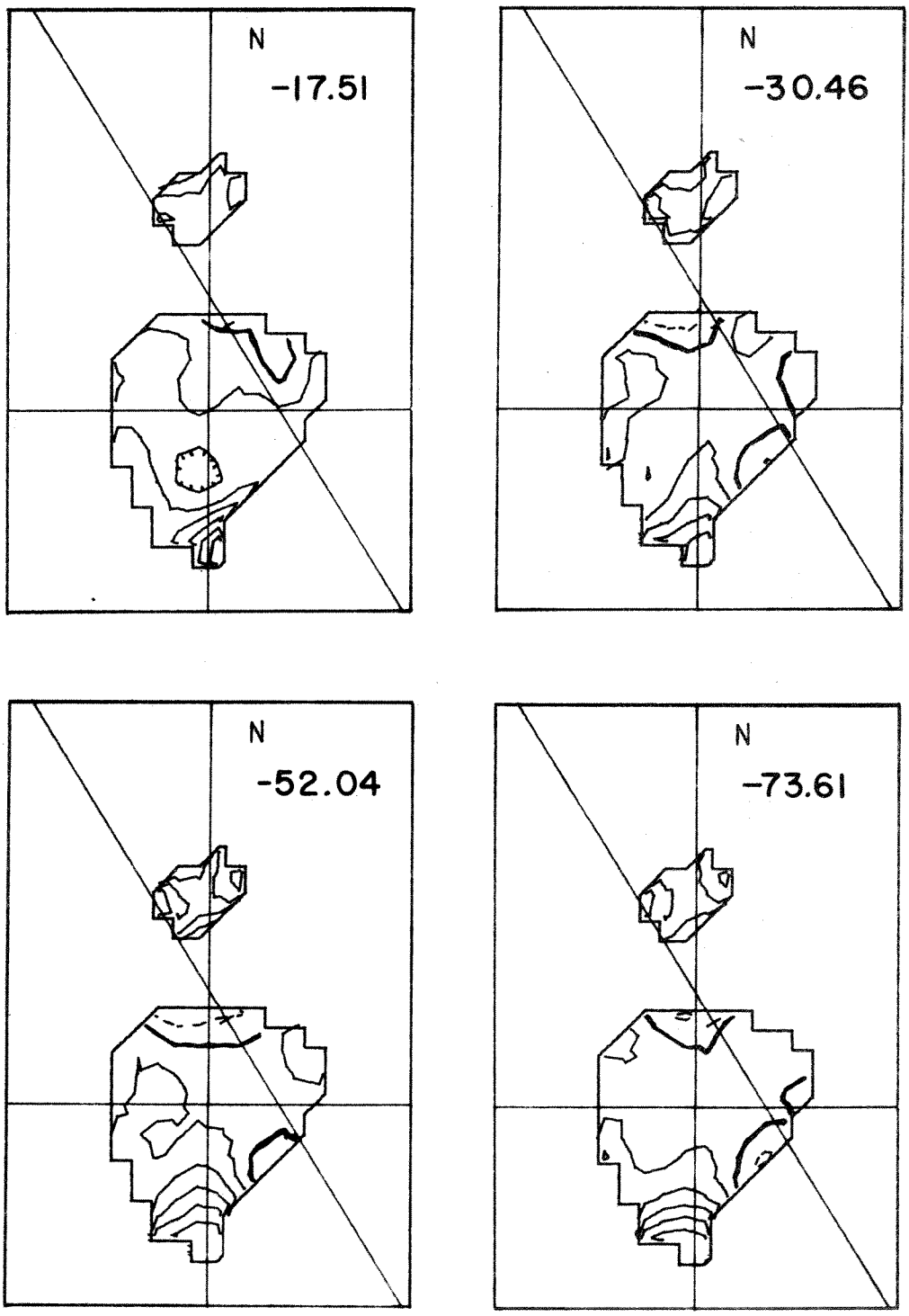

Fig. 3-6 (cont'd.) Contour interval is 0.10

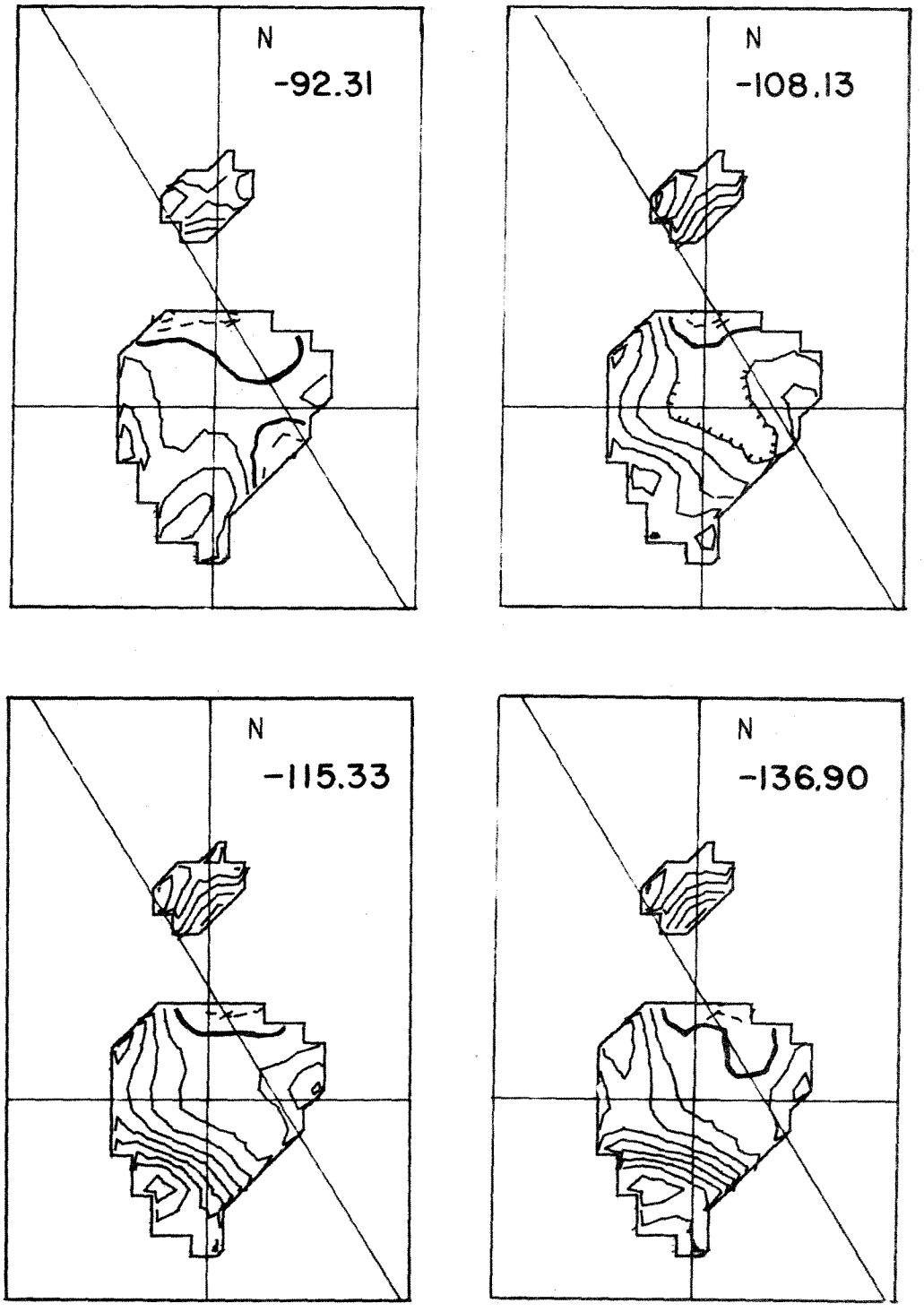

Fig. 3-6 (cont'd.) Contour interval is 0.10

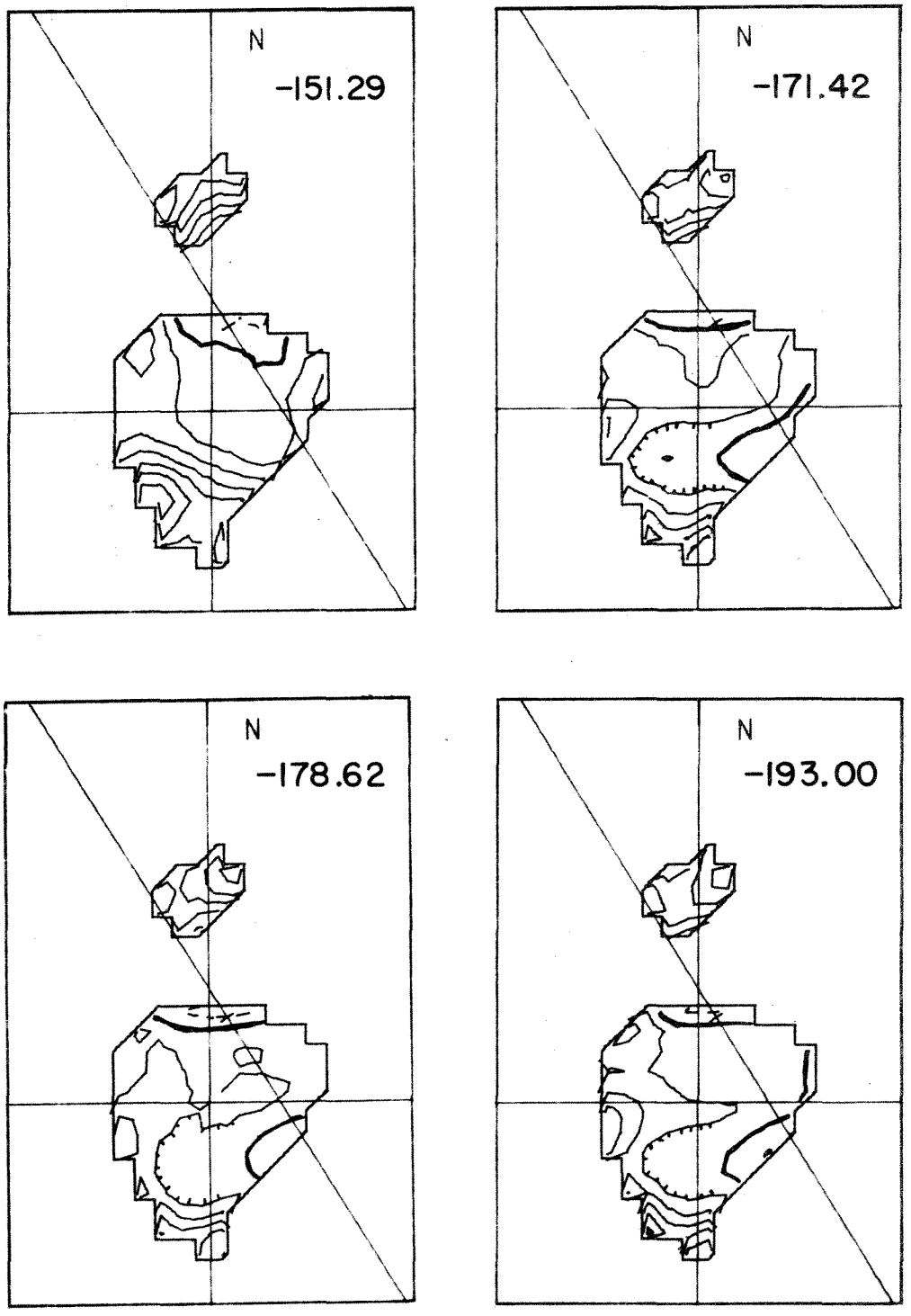

Fig. 3-6 (cont'd.) Contour interval is 0.10

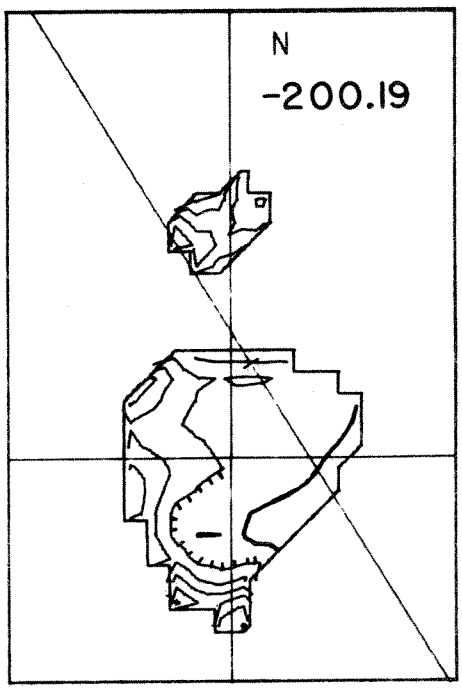

Fig. 3-6 (cont'd.) Contour interval is 0.10

those shown in Figure 3-6. Column one lists the velocity of the map; columns two and three are the galactic coordinates for the position of peak absorption. Note that for velocities less than 37 km/s, there are two components to the cloud. The tabulated values apply to the estimated peaks of each component. Column four gives the approximate dimensions of the absorption feature at half-maximum optical depth. The dimensions given should be viewed with caution, since the cloud appears to extend beyond the edge of the continuum. Column five lists the peak optical depth, and column six identifies which component (labelled "I" and "II") the data refer to.

Table 3-4

Measured Properties of the "+40 km/s" Cloud in Sgr A

V (km/s)	l (')	b (')	Dim's. (')	τ_{max}	Component
74.55	+0.5	-4.4	6 × 4	0.22	
67.35	+0.4	-3.7	7 × 5	0.43	
60.16	-0.4	-4.9	7 × 5	0.77	
52.97	-0.9	-5.4	7 × 5	1.12	
45.78	-1.8	-5.2	7 × 5	1.19	
38.59	-2.2	-5.4	8 × 5	1.11	
37.15	-2.2	-5.5	7 × 5	1.09	
34.27	-2.7	-5.4	9 × 5	0.90	I
	-5.0	-5.7		0.96	II
32.83	-2.4	-5.4	8.5 × 6	0.90	I
	-5.2	-5.7		0.90	II
25.64	-2.2	-4.9	6	0.5	I
	-6.0	-5.7	5	0.88	II
18.45	-1.7	-3.8	6	0.33	I
	-7.4	-5.7	?	0.80	II

Discussion of the kinematical implications of these data is deferred until Chapter 4. It is worth noting, though, that the cloud size is clearly larger than the synthesized beam. Since the continuum source also fills the beam, we are indeed justified in setting R and F , the filling factors of equation (3.2) to unity. The continuum brightness temperature of the maps is large, being greater than 100 K even at the edge of the optical depth maps, so the excitation temperature T_s is also expected to be negligible. Given these conditions, the calculated optical depths of column five should be the true values for the +40 km/s cloud, unaffected by the instrumental errors to which lower-resolution observations are subject. As an example, the maximum optical depth of 1.19 at 45.78 km/s corresponds to an opacity, $(1 - e^{-\tau})$, of 0.70. The best previous estimate (McGee 1970a) has an opacity of about 0.25 for that velocity and position, which implies an optical depth of 0.28, a factor of four smaller than the true value. Since the columnar density of molecules is proportional to optical depth, this fourfold increase may have significant implications for the determination of the physical and chemical conditions in the molecular clouds.

Other than the +40 km/s cloud, the optical depth maps of Sgr A do not show any clearly discrete features. The absorbing material appears to be concentrated near the edge and away from the central source. This confirms the impression gotten from the sample spectra of Figure 3-5, where the five spectra nearest the continuum peak show only weak absorption except for the +40 km/s feature. For this reason

the clouds cannot be catalogued by the location and velocity of the maximum absorption. Instead, a largely qualitative discussion will be given. The maps at 4.06 and -3.13 km/s are similar in appearance, with a broad feature of $\tau \simeq 0.2$ covering most of the continuum, except the northern edge, which is unabsorbed. At -3.13 km/s, the optical depth contours are larger in value by about 0.1, reflecting the sharp absorption feature noted above. There is no evidence of clumpiness in this absorption, which fact supports the view that the narrow spectral feature is due to large-scale OH distributed along the line of sight to the galactic center. At the southern tip of the continuum, a feature persists with rather high optical depth at the edge of the map. This feature is found even at very large negative radial velocities, and it might be argued that it is due to a systematically high value for the continuum in that region. However, point spectra 8 and 13 (Figure 3-5) give evidence that the absorption is real. Spectrum 8 closely resembles the single-dish spectrum, both showing significant absorption at velocities between the two deep features. Spectrum 13 appears to have a number of blended components which combine to produce an absorption line from at least +50 km/s to the end at -200 km/s. The good continuity across frequency shifts seems to indicate that the effect is not due to systematic differences between the shifts, but is a real absorption over that large velocity range. (The profile given in McGee (1970b) for the position $l = 359^{o}50'$, $b = -10'$, shows a similar depression of the entire spectrum below the level at +90 km/s. McGee dismisses this simply as a "baseline effect",

without further explanation, but the present results indicate that the absorption is, in fact, real.)

The contour maps between -17.51 and -73.61 km/s show little change in the structure of the absorption. The optical depth is about 0.05 over the central source, with a gradient increasing toward the south. The small region at the northern edge of the continuum which appears to show emission (negative optical depth) in frequency shift number three is attributable to a systematic level error for that shift and region. The maps at -30.46 and -52.04 km/s do not show any significant differences from adjacent channel maps, which is evidence that the narrow features of the single-dish spectrum are due to material uniformly distributed in front of the source, not associated with the galactic center but lying closer to the Sun. The absorption at -53 km/s is identified with the 3.7 kpc expanding arm, which has been discussed extensively by Rougoor (1964) on the basis of neutral hydrogen observations.

Beginning with the map at velocity -92.31 km/s, a group of absorbing clouds becomes visible lying southeast of the continuum peak and forming a band roughly parallel to the galactic equator. The spectra 6, 7, and 8 of Figure 3-5 show a very strong absorption line centered at around -120 km/s. The velocity of maximum absorption is a function of position, such that at position 6, the peak opacity is at -112 km/s while at position 8 the value is -135 km/s. Moreover, the intermediate position 7 spectrum shows what looks like a blend of two components, one at each of these velocities. The -92.31 km/s map suggests two clouds connected by a bridge of absorption, with maximum

optical depths of about 0.4 in each component. At -108.13 km/s the maximum optical depth in the map is 0.55 along this band of OH clouds. Note that the contour lines bend around the position of the continuum peak, which has an optical depth of less than 0.05 at this velocity. A similar picture is found in the -115.33 km/s map, except that the maximum optical depth is up to 0.88, with weaker absorption at higher galactic longitude. Unfortunately the peak absorption almost certainly lies beyond the edge of the cutoff for computing optical depth, so that the location of the cloud center and the overall dimensions cannot be estimated. The contour maps clearly show that the absorption extends over an angular distance of 12 arcminutes in galactic longitude at a latitude of $b = -5'$.

At the velocity -136.90 km/s the absorption peak has shifted to a longitude of about -5', and a latitude below -7'. The contour maps are essentially unchanged to the velocity -151.29 km/s, except for a gradual decrease in optical depths. By -171.42 km/s, the absorption at latitude $b = -5'$ has largely disappeared, except for the very southern tip of the continuum. There is a weak band, of optical depth about 0.1, running across the continuum peak approximately perpendicular to the galactic plane. This absorption is present in spectra 1 through 5 of Figure 3-5, beyond -160 km/s. A cluster of local absorption maxima are concentrated along the southeast edge of the continuum, and are essentially unchanged to the end of the velocity coverage. These relatively small absorption features are evidently extensions in the velocity domain of the major absorbing clouds seen from -90 to

-150 km/s. Together with the weak band of absorption across the Sgr A peak, these small features produce the low-velocity shoulder of the -135 km/s absorption line in the single-dish spectrum.

Spectra at Selected Grid Points--Sgr B2

Following the format of the discussion for Sgr A, we now consider brightness temperature spectra for points in the map of the Sgr B2 region. Figure 3-7 is a spectrum obtained with the 100 channel autocorrelator and 130-foot telescope, with a frequency resolution of 25 kHz. The telescope was pointed toward the peak of the G0.7-0.0 continuum. (For the observations which produced this spectrum I am indebted to R. M. Crutcher.) In some respects the spectrum resembles the single-dish result for Sgr A. We see two broad components, one with a smooth minimum at -90 km/s. The other is a blend of at least two features, with local minima at 19 and 62 km/s; its shape is quite asymmetrical, probably due to blending of the constituent lines. Only two narrow spectral features are present, both very weak. At -42 km/s is a feature with a linewidth at half-maximum of 8 km/s, and at -24 km/s another feature with a 10 km/s width. By assuming as for Sgr A, that these lines arise in material not associated with the galactic center, but lying well in front, we can extrapolate the wings of the +60 km/s line across the narrow features and derive their opacities. The results of this analysis are presented in Table 3-5, which has the same information as defined for Table 3-1.

In comparing the two single-dish spectra, we see that the Sgr B2 profile has no evidence for a sharp feature near zero velocity. This

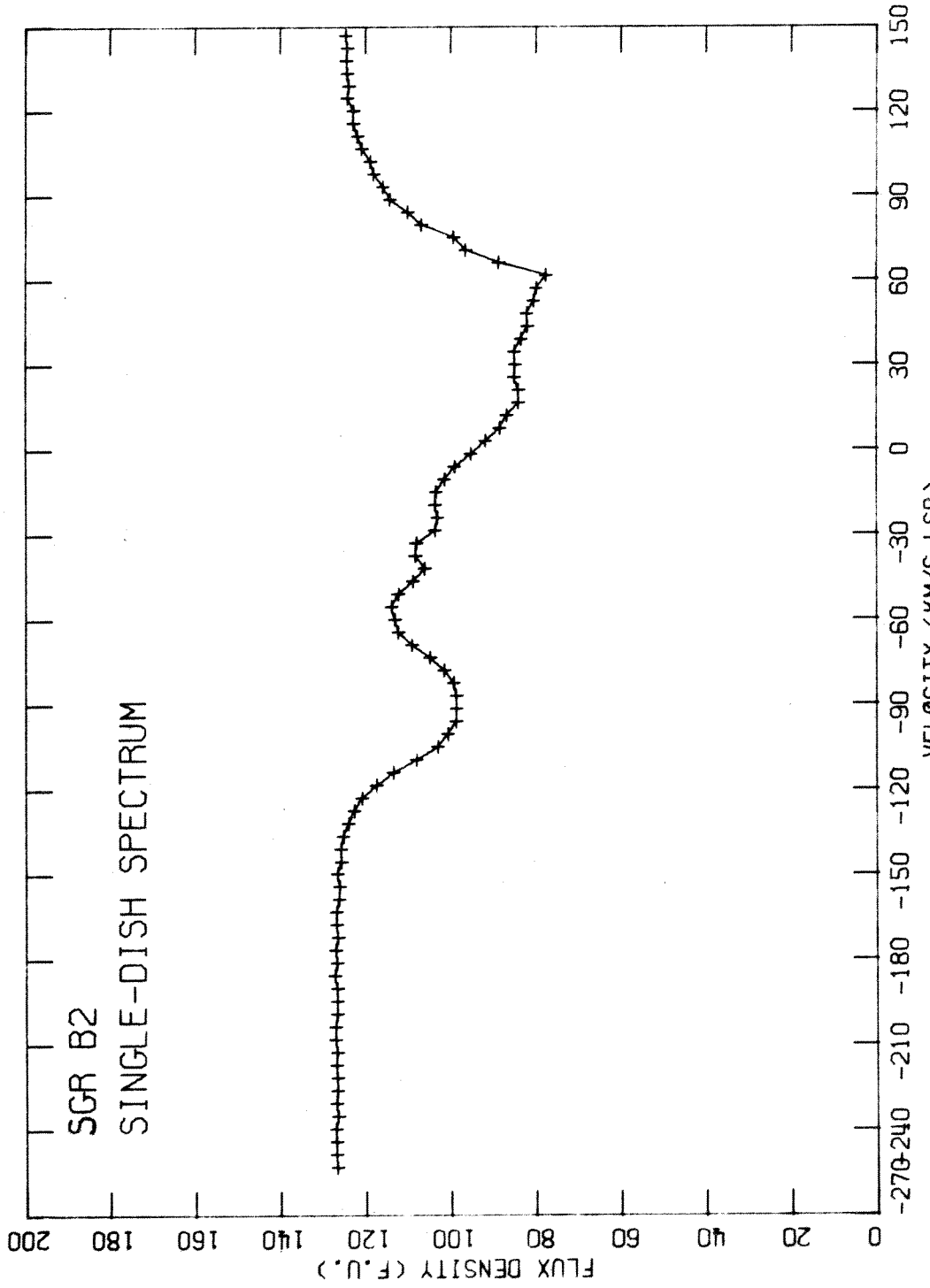

Fig. 3-7. Sgr B2 1667 MHz absorption spectrum obtained with 130-foot telescope and 100-channel autocorrelator.

Table 3-5

Summary of Single-Dish Spectral Features--Sgr B2

V_o (km/s)	$\Delta V_{1/2}$ (km/s)	S_{line} (f.u.)	S_{cont} (f.u.)	Opacity
62	90 ± 5	49 ± 1	127	0.39 ± 0.01
19		43 ± 1	127	0.34 ± 0.01
-24	10 ± 3	3 ± 1	106	0.03 ± 0.01
-42	8 ± 2	4 ± 1	110	0.04 ± 0.01
-90	50 ± 3	28 ± 1	127	0.22 ± 0.01

is in contrast to the Sgr A spectrum, where the absorption at -2 km/s is the most prominent of the three narrow lines. The shapes of the broad, positive-velocity features are quite different in the two spectra, and the broad negative-velocity components are at different velocities. For the Sgr B2 spectrum, there is no evidence of absorption below -150 km/s, but the line definitely extends above +100 km/s. For Sgr A, the absorption is essentially gone at +100 km/s, but extends down to -240 km/s. Finally, the two weak features of the Sgr B2 spectrum, while about the same opacity as their Sgr A counterparts, are centered at velocities systematically closer to zero, by 11 and 6 km/s for the -42 and -24 km/s lines, respectively.

The continuum map of Sgr B2 in Figure 3-8 is a key to the numbered spectra to follow, as for the Sgr A spectra presented earlier. Figure 3-9 is a selection of 23 spectra with brightness temperature corrected for the primary beam response, at individual grid points on the synthesized maps. As before, pairs of spectra at points less than

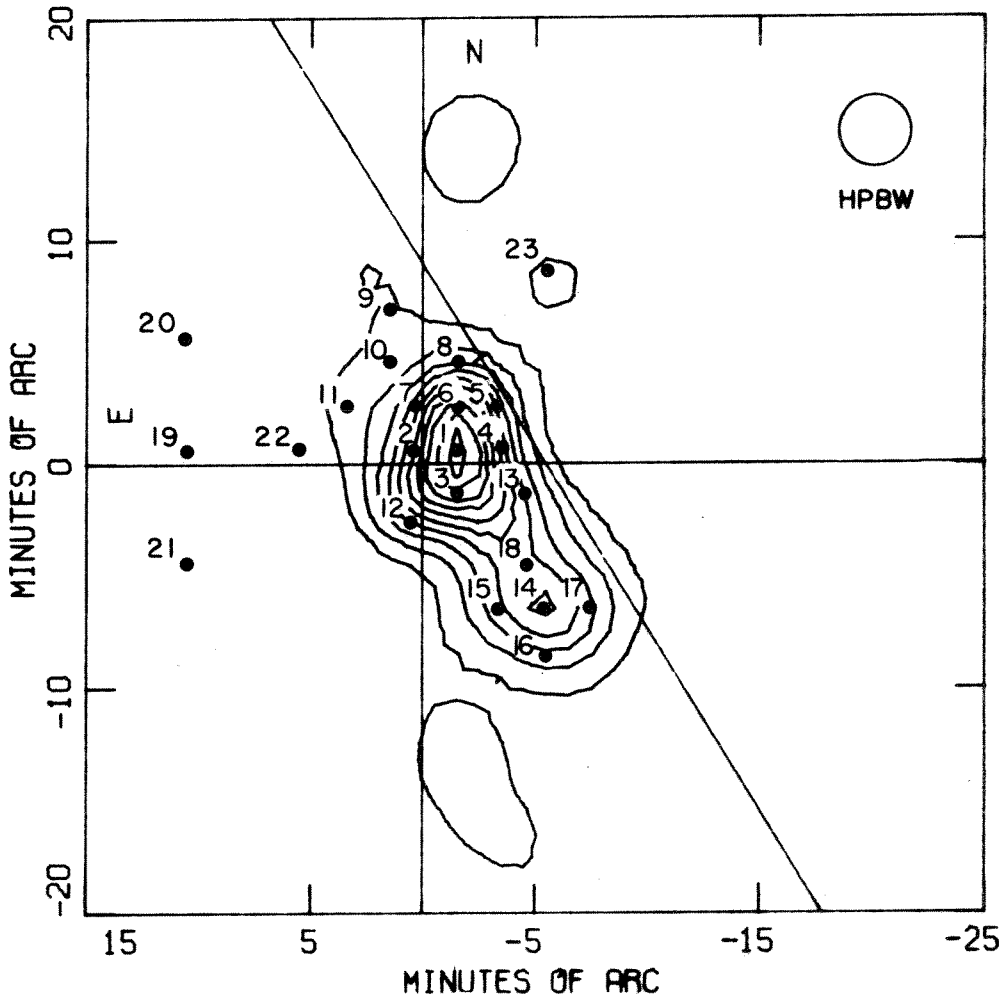

Fig. 3-8. Key to point spectra for Sgr B2.

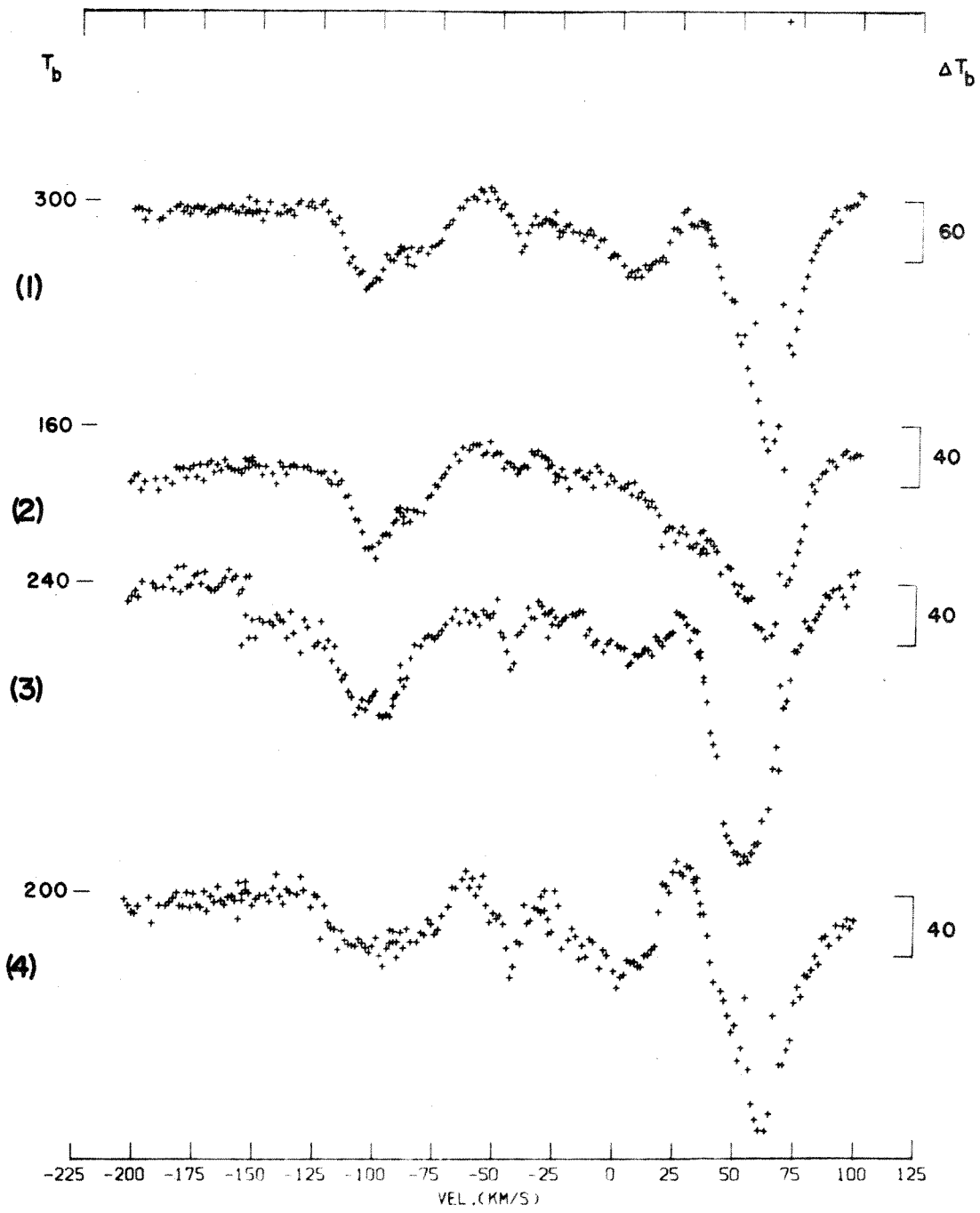

Fig. 3-9. Spectra for selected map points, Sgr B2. Numbers in parentheses refer to Fig. 3-8. Brightness temperature level indicated on left, scale on right (both in K). Zeros are displaced.

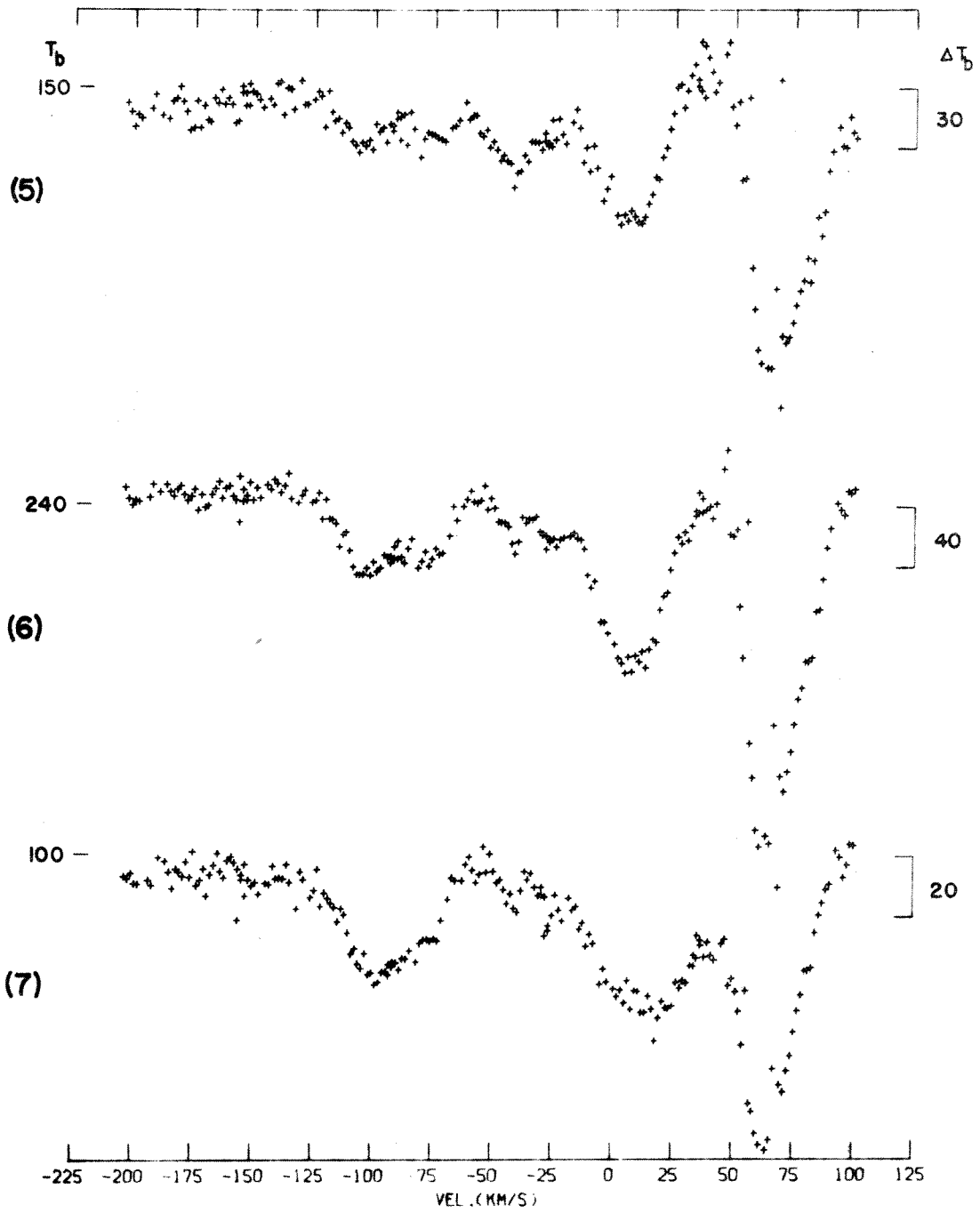
T_b
150
ΔT_b
30
(5)
240
40
(6)
100
20
(7)
-225 -200 -175 -150 -125 -100 -75 -50 -25 0 25 50 75 100 125
VEL.(KM/S)

Fig. 3-9 (cont'd.)

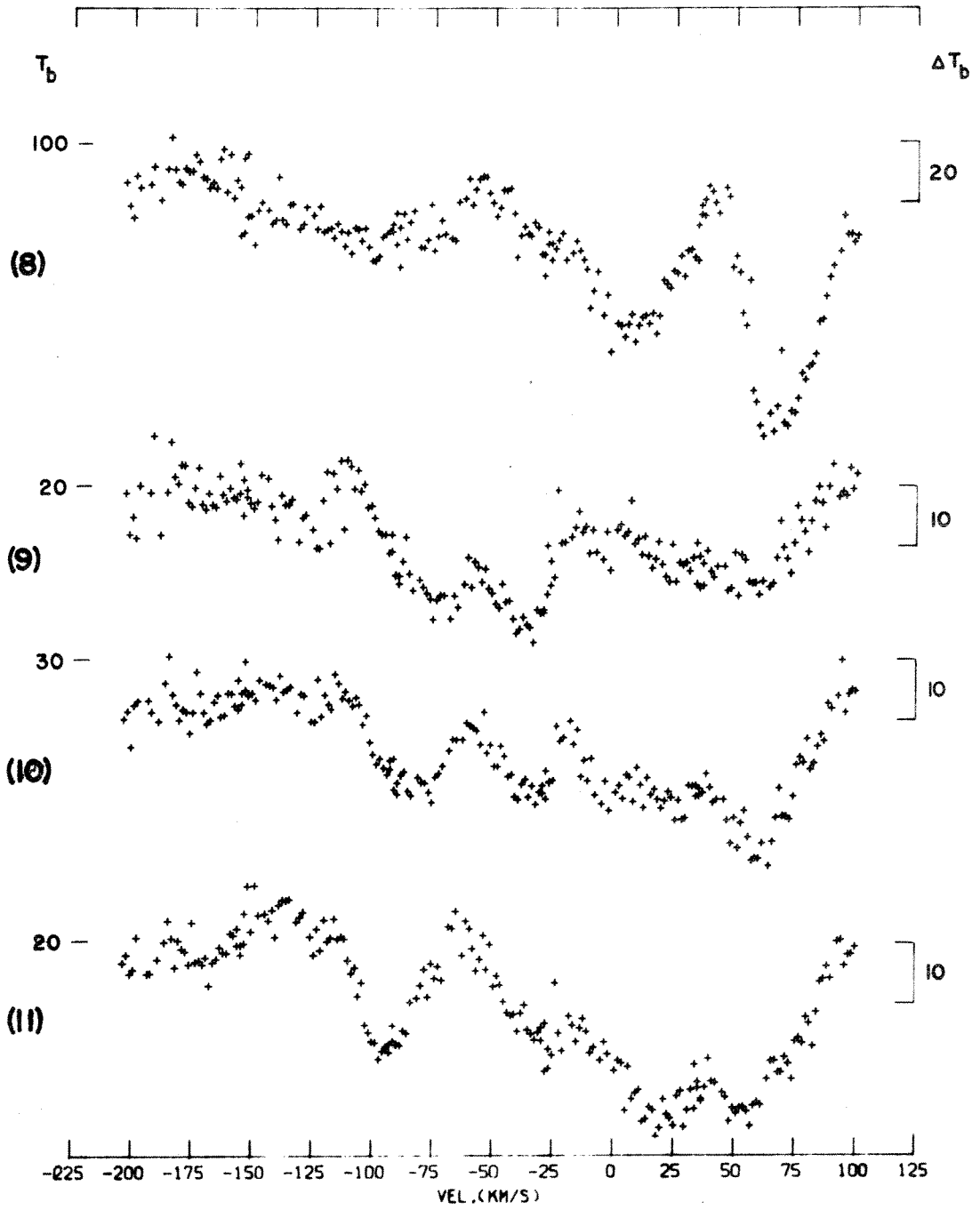
T_b
ΔT_b
100
20
(8)
20
10
(9)
30
10
(10)
20
10
(11)
-225 -200 -175 -150 -125 -100 -75 -50 -25 0 25 50 75 100 125
VEL.(KM/S)

Fig. 3-9 (cont'd.)

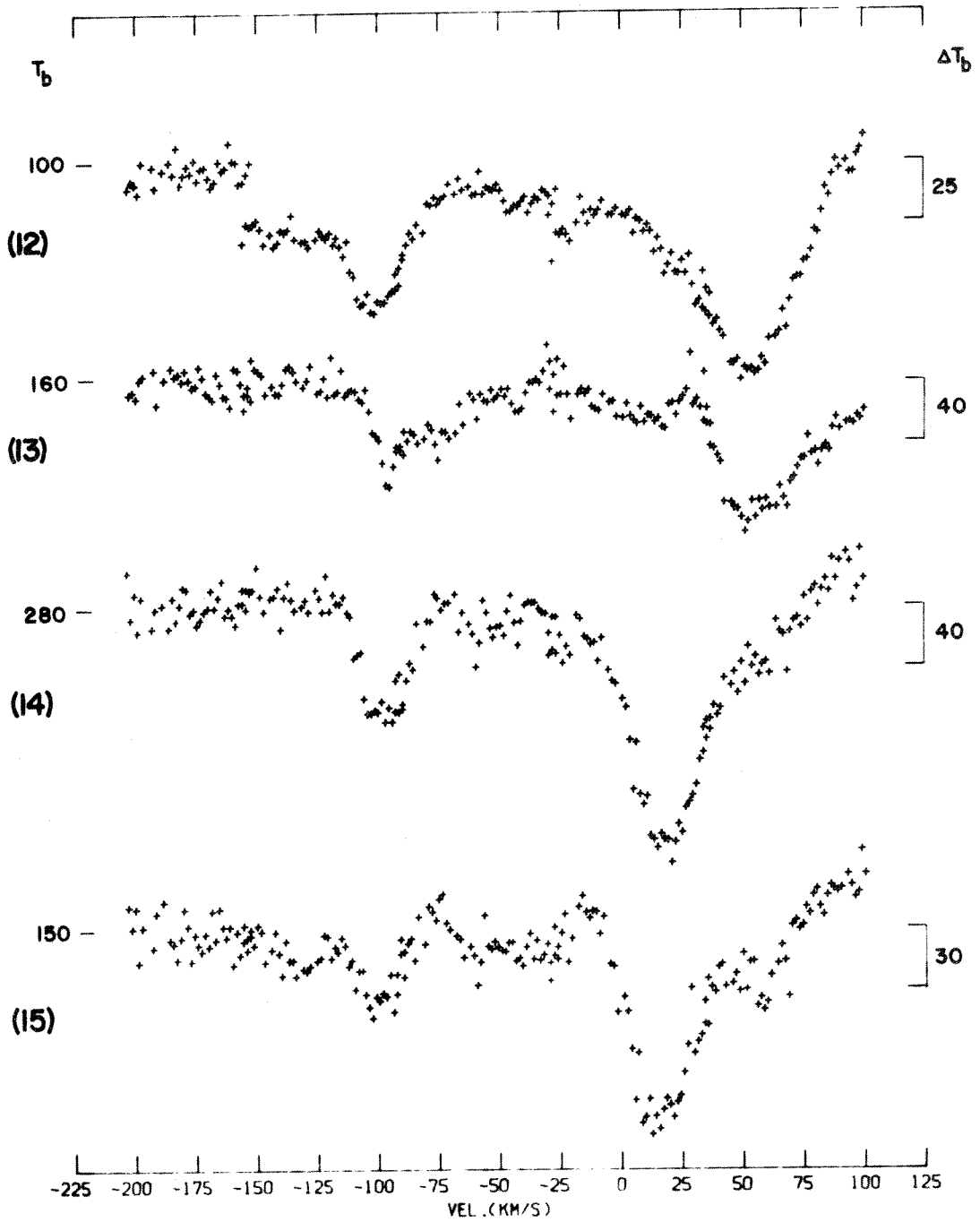
T_b
ΔT_b
100
(12)
25
160
(13)
40
280
(14)
40
150
(15)
30
-225 -200 -175 -150 -125 -100 -75 -50 -25 0 25 50 75 100 125
VEL.(KM/S)

Fig. 3-9 (cont'd.)

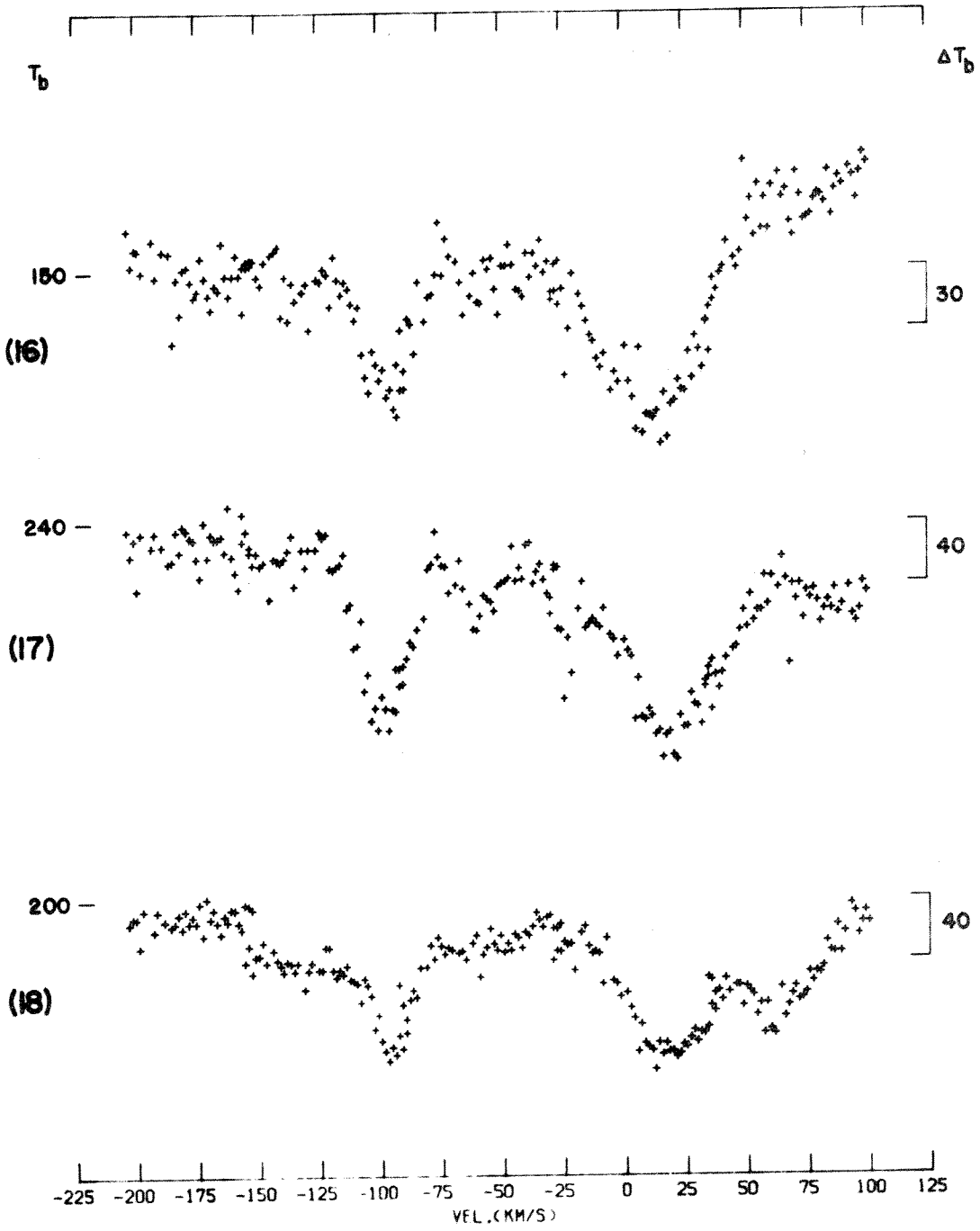
T_b
ΔT_b
150 —
30
(16)
240 —
40
(17)
200 —
40
(18)
-225 -200 -175 -150 -125 -100 -75 -50 -25 0 25 50 75 100 125
VEL.(KM/S)

Fig. 3-9 (cont'd.)

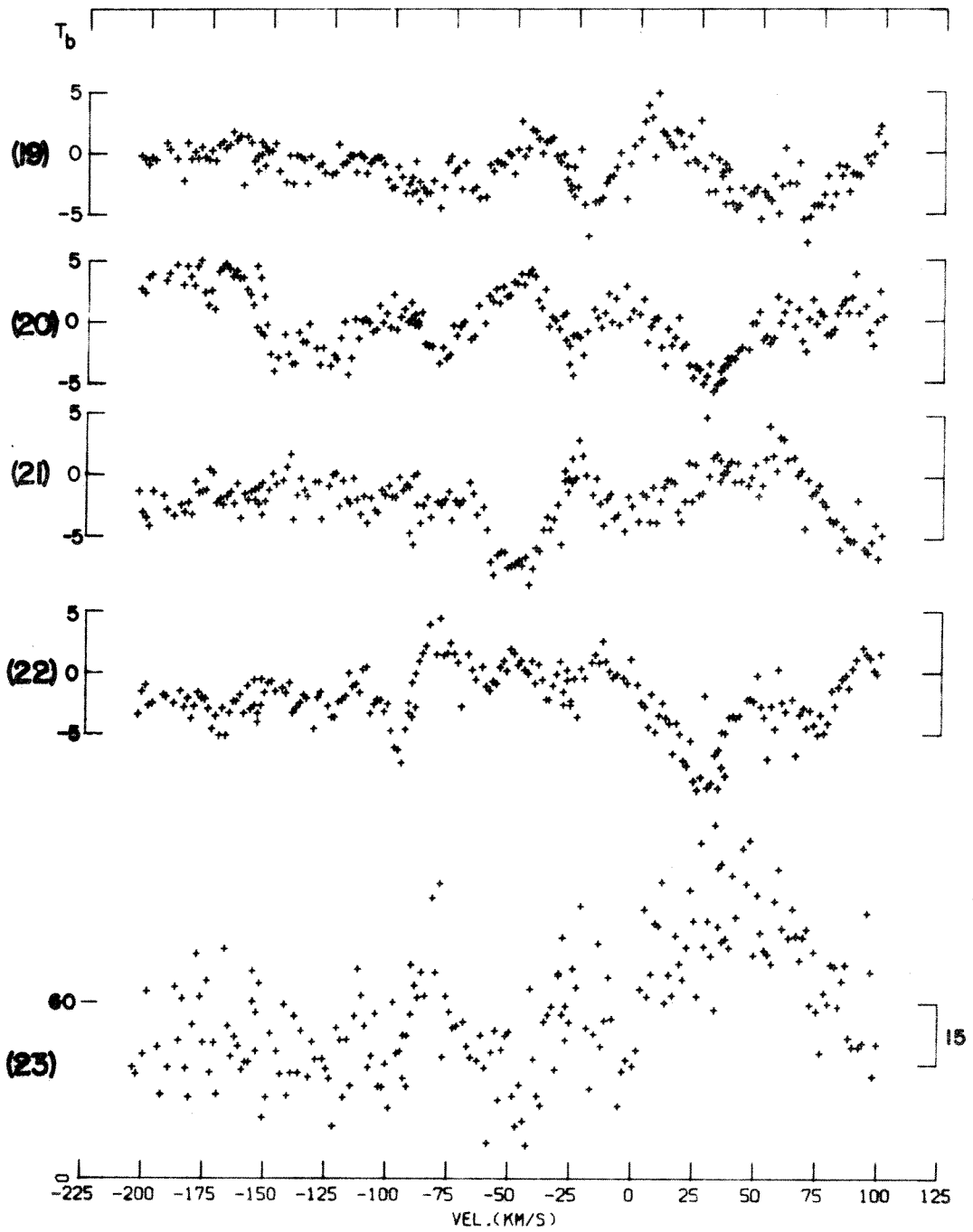
T_b
(19)
(20)
(21)
(22)
(23)
5
0
-5
60
15
-225 -200 -175 -150 -125 -100 -75 -50 -25 0 25 50 75 100 125
VEL.(KM/S)

Fig. 3-9 (cont'd.)

three arcminutes apart are not completely independent, since the synthesized beam has a half-power diameter of 3.25 arcminutes. The general arrangement of sample points is as follows: Number 1 lies at the continuum peak of the discrete source G0.7-0.0, and 2 through 7 form a ring around the peak, offset by some two arcminutes. Points 8 through 13 lie in an outer ring about the peak, at distances from five to eight arcminutes. Point 14 is at the continuum peak of the source G0.5-0.0, with 15 through 18 at two arcminute offsets around it (number 18 lying near the line between the two continuum maxima). Points 19 through 22 are away from the discrete continuum components, in the region where McGee (1970a) reports a large number of high opacity clouds. It was hoped that, although there is no discrete continuum source in this region, evidence for small-scale areas of line emission might be found, or that limits could be set on the excitation temperature. Finally, point 23 is located near the center of the extended region of weak emission seen in the brightness temperature maps of Figure 3-2, for velocities between 18.45 and 74.55 km/s.

This collection of spectra shows how complicated is the distribution of the molecular clouds in both velocity and position. Number 1 has five clearly distinguishable absorption components, and two or possibly three sharp maser emission spikes. In contrast, spectrum 14, at the peak of the G0.5-0.00 source, has apparently only two components, including one at about 20 km/s which has a markedly larger opacity than the 20 km/s absorption in spectrum 1. Similar comparisons of other spectra show more absorption features, which also have opacities strongly dependent on position.

In order to permit a quantitative analysis, the parameters of all the absorption features visible in spectra 1 through 18 have been measured and are tabulated in Table 3-6. The information given is similar to that of Table 3-3 for Sgr A, with the 1950 coordinates of the gridpoint in columns 2 and 3, the velocity of maximum opacity, V_o, in column 4, the full linewidth at half-maximum intensity in column 5, and the value of the maximum opacity in column 6. In determining the line opacity, which is defined as the ratio of the brightness temperature removed by the line to the brightness temperature of the continuum, the continuum level was taken to be the average of the channels with velocity less than -150 km/s. From the single-dish spectrum of Figure 3-7 it is known that Sgr B2 is unabsorbed in this velocity range. Some of the features are blended together, making an estimate of the linewidth too uncertain to be meaningful. These entries are indicated by question marks, and by a notation in the comments column. In some cases the profile appears to consist of a narrow core centered on a weaker, broader component; this condition is indicated in the last column. Two of the spectra have a significant discontinuity across the end of a frequency shift, so that the opacity of a spectral feature becomes very uncertain, and this is also noted.

Table 3-6 shows that the absorption features tend to fall within certain velocity ranges, depending on position in the map. Near +60 km/s there is a series of intense absorption components concentrated on the source G0.7-0.0, but absent from the positions on G0.5-0.0. Similarly, a strong absorption occurs centered at about +5 km/s in front

Table 3-6

Summary of Absorption Components--Sgr B2

Spectrum Number	α_{1950} h m s	δ_{1950} ° '	V_o (km/s)	$\Delta V_{1/2}$ (km/s)	Maximum Opacity	Notes
1	17 44 11.8	-28 23.5	62(1)	20(3)	0.83(.02)	
			5(5)	25(5)	0.22(.03)	
			-43(1)	4(1)	0.15(.02)	Cf
			-85(5)	?	0.15(.04)	
			-106(3)	15(4)	0.27(.05)	
2	20.8	23.5	61(1)	35(10)	0.85(.02)	
			-85(5)	?	0.23(.05)	
			-105(3)	15(4)	0.40(.05)	
3	11.8	25.5	55(3)	29(2)	0.76(.02)	
			5(5)	35(5)	0.10(.03)	
			-43(2)	8(3)	0.23(.03)	Cf
			-100(10)	35(5)	0.33(.03)	
4	02.7	23.5	62(3)	25(3)	0.78(.02)	
			0(5)	35(5)	0.25(.05)	
			-42(2)	6(2)	0.25(.03)	Cf
			-100(10)	40(5)	0.18(.05)	
5	02.7	21.5	64(2)	28(2)	0.93(.02)	
			5(5)	30(3)	0.40(.04)	
			-42(2)	15(5)	?	Cf
			-107(3)	15(5)	0.15(.04)	
6	11.8	21.5	62(2)	25(3)	0.94(.02)	
			7(5)	32(5)	0.45(.02)	
			-41(1)	5(2)	0.10(.02)	Cf
			-85(10)	?	0.17(.04)	
			-105(5)	20(5)	0.21(.02)	
7	20.8	21.5	62(2)	24(2)	>0.95(.05)	
			10(5)	45(5)	0.45(.05)	
			-41(2)	5(2)	0.12(.03)	Cf
			-100(5)	40(5)	0.37(.03)	
8	11.8	19.5	61(2)	30(5)	>0.95(.05)	
			5(5)	45(5)	0.58(.05)	
			-100(10)	60(15)	0.25(.05)	

Table 3-6 (cont.)

Spectrum Number	α_{1950} h m s	δ_{1950} ° '	V_o (km/s)	$\Delta V_{1/2}$ (km/s)	Maximum Opacity	Notes
9	17 44 25.4	-28 17.5	50(15)	?	0.50(.10)	Bl
			-37(5)	25(5)	>0.90	
			-75(5)	30(5)	0.75(.10)	
10	25.4	19.5	60(5)	25(10)	0.80(.10)	
			20(10)	?	0.55(.10)	
			-35(5)	25(10)	0.50(.05)	
			-85(5)	35(5)	0.45(.05)	
11	34.5	21.5	55(5)	?	>0.9	
			20(10)	?	>0.9	
			-30(5)	?	0.45(.10)	
			-96(5)	25(5)	0.55(.10)	
12	20.8	26.5	53(3)	48(5)	0.85(.05)	
			-43(3)	6(2)	0.10(.03)	
			-100(5)	22(5)	0.55(.15)	D
13	58.1	25.5	55(5)	40(5)	0.55(.05)	
			5(10)	?	0.15(.05)	
			-43(2)	5(2)	0.10(.02)	
			-96(5)	10(2)	0.42(.03)	
			-85(5)	35(5)	0.2 (.05)	
14	53.6	30.5	18(4)	30(3)	0.56(.04)	
			-98(4)	22(3)	0.27(.03)	
15	02.7	30.5	12(5)	33(5)	0.60(.05)	
			-100(5)	15(5)	0.23(.05)	
16	53.6	32.5	10(5)	40(5)	0.50(.05)	
			-100(5)	20(5)	0.40(.07)	
17	44.5	30.5	20(5)	50(5)	0.55(.05)	
			-60(5)	20(5)	0.20(.05)	
			-97(3)	25(5)	0.50(.05)	
18	58.1	28.5	61(3)	?	0.37(.05)	Bl
			15(5)	40(10)	0.45(.05)	Bl
			-96(3)	20(5)	0.45(.05)	D

Notes: Bl = blended; Cf = confused by underlying broad component; D = opacity uncertain because of discontinuity across frequency shifts.

of the higher longitude source but not in front of the lower one. Conversely, G0.5-0.0 shows a strong absorption line centered around +15 km/s, whereas the G0.7-0.0 source is largely unabsorbed at that velocity, except near the northeast edge of the continuum. There is evidence of an absorption line at -43 km/s in spectra 1 through 7, 12 and 13. The opacity of this narrow feature seems to be somewhat larger, when it is present, than the opacity of the single-dish feature. The point spectra, however, show a broader component underlying the narrow core. The true value of the opacity is quite uncertain, because the continuum level is not well determined. The other narrow component, at -24 km/s, is not evident in the spectra from the synthesized maps.

The prominent negative velocity absorption appears to come from three distinct velocity components centered at -85, -100, and -105 km/s. Near the G0.7-0.0 peak the two at -85 and -105 are blended together, but spectra 1, 2, 6, and 7 have a definite appearance of two features close together. Spectra 13 and 18 show a deep, fairly narrow feature at about -95 km/s, roughly midway between the two continuum peaks. At the southwest source, G0.5-0.0, an absorption line near -100 km/s is found in the five spectra, 14 through 18, but is strongest toward the southwest edge (numbers 16 and 17).

Although the spectra of Sgr B2 for the selected map points show the range of velocities and opacities which the molecular clouds encompass, we find as for Sgr A that the picture is incomplete. The spatial relationships between absorption features are not clear from the spectra alone. By combining the information from the spectra of

Figure 3-9, with two-dimensional plots of optical depth at fixed velocities, a coherent picture of the molecular clouds will emerge.

Observational Limits on the Value of the Excitation Temperature

It is known that the excitation temperature of the 1667 MHz OH line is low in the vicinity of the galactic center (Robinson and McGee 1970), since normal (i.e., non-masering) emission has not been detected there. All previous observations had inadequate angular resolution, however, so that the complicated structure and high brightness temperatures of the discrete continuum sources mask any weak emission away from the bright continuum but within the telescope beam. With the angular resolution of the present work, it is possible to differentiate the absorption in front of the strong sources from any weaker emission that might exist off source. Any off-continuum emission would be expected to have a low brightness temperature, given by equation (3.1). If we assume that the cloud fills the synthesized beam and that the continuum is negligible, we have

$$T_{NB} = T_S(1 - e^{-\tau}) \ .$$

In the case where the cloud is optically thick, the observed brightness temperature equals the excitation temperature. Spectra 19 through 22 of Figure 3-9 are taken at points in the region where McGee (1970a) finds the largest concentration of OH clouds. If regions of high opacity and with an excitation temperature larger than the residual galactic background brightness temperature are present in these clouds, they should show up as emission lines in the point spectra of that

area.

The spectra are difficult to interpret, unfortunately, because of the uncertainty in determining the true continuum level. Spectral features appear with both positive and negative brightness temperature. If the galactic and the isotropic backgrounds contribute a total of about 7K, so that the true zero of brightness temperature is at -7K on the ordinate of spectra 19-22, and if we assume the OH is optically thick, as it is in front of the bright continuum sources, then we may set upper limits on the excitation temperature. Given the scatter of the points, there is no emission greater than 3K in any of the spectra. With the above assumptions, we conclude that $T_s \leq 10K \pm 2K$ for this region.

Spectrum 23 of Figure 3-9 shows evidence for what may be line emission. In the discussion of brightness maps at the beginning of this chapter, it was noted that the maps between +75 km/s and +20 km/s showed a bright extended region lying north and a little west of G0.7-0.0. The noise level is high on the spectrum at that position, but there is a definite impression of an emission line peaking at about 45 ± 10 km/s, and extending from +75 km/s to around +10 km/s. This is roughly the velocity range at which the strongest absorption of G0.7-0.0 occurs. It seems not unreasonable to infer that the cloud complex at around +60 km/s extends to the region in which the emission appears. Given this hypothesis, one can estimate the excitation temperature of the OH gas. From spectrum 23 (which has been corrected for the primary beam response), the continuum level is about $50K \pm 8K$, while the brightness temperature at 45 km/s is about

80K ± 10K. Assuming both that the cloud is optically thick so that $(1 - e^{-\tau})$ is close to unity, and that no continuum emission arises in front of the OH, then the observed brightness temperature will equal the excitation temperature, so $T_s \doteq 80K \pm 10K$. If, on the other hand, we assume that all the continuum emission is produced in front of the cloud (in a region which is itself optically thin at 1.7 GHz), then the excitation temperature is given by the excess line temperature alone, so $T_s \doteq 30K \pm 10K$. The implications of these results will be examined in Chapter 5.

The Sgr B2 Maser Emission Lines

In spectra 1 through 8 of Figure 3-9 there are sharp spikes of emission in the deep +60 km/s absorption line. The existence of these maser sources has been known for some time (Palmer and Zuckerman 1967). The position of the most intense component, at +69.0 km/s, has been determined interferometrically by Raimond and Eliasson (1969). Positions of the 1665 MHz sources were obtained by Manchester, et al. (1969) from lunar occultation observations. Palmer and Zuckerman (1967) list five features at 1667 MHz, three with nearly 100% left-circular polarization at velocities +69.0, 68.1, and 67.1 km/s; and two with 100% right-circular polarization, at 55.8 km/s and 54.7 km/s. The velocity resolution of the present work is not adequate to distinguish all of these five components, but the emission at 69.0 km/s clearly extends over three channels in the spectrum, in agreement with Palmer and Zuckerman. There is evidence in spectra 1 through 8 that there may also be a weak emission line at 51.5 km/s in addition to the

obvious lines at 55.85 km/s and 68.79 km/s.

The position and intensity of these emission sources was determined by interpolating the brightness temperature of the channels on either side which show no emission, to the channel where emission was present. This procedure was performed at each map point, to produce an interpolated estimate of the brightness distribution without emission. This map was then subtracted from the map which showed emission, leaving only the excess brightness temperature due to the maser source. The resulting brightness maps for channels 24 and 33 (velocities 68.79 and 55.85 km/s) are shown in Figures 3-10 and 3-11. Each map shows a single unresolved point source, smoothed by the synthesized beam to a half-power diameter of about three arcminutes. To obtain the best estimate of the position and intensity of the maser sources, a least-squares fit to a circular gaussian was performed for this residual map in each channel showing emission. It was found that the positions for channels 23, 24, and 25 agreed to within the uncertainties, so only the peak channel, for which the errors are the smallest, is given here. This analysis was also carried out for channel 36, which appeared as a weak point source. The results of the fit are in Table 3-7; quoted errors are three standard deviations of the fitted parameters.

Table 3-7

Parameters of Best-Fit Gaussian to Point Emission Sources--Sgr B2

Channel	Velocity (km/s)	α(1950) h m s	δ(1950) ° ′ ″	Flux Density (f.u.)	Diameter (FWHM) (′)
24	68.79	17 44 10.6 ± 0.3	-28 22 45 ± 4	37 ± 4%	3.15 ± .05
33	55.85	17 44 10.7 ± 0.4	-28 22 01 ± 6	11 ± 5%	3.1 ± .1
36	51.53	17 44 09 ± 1.5	-28 22 11 ± 20	3.0 ± 20%	3.2 ± 0.2

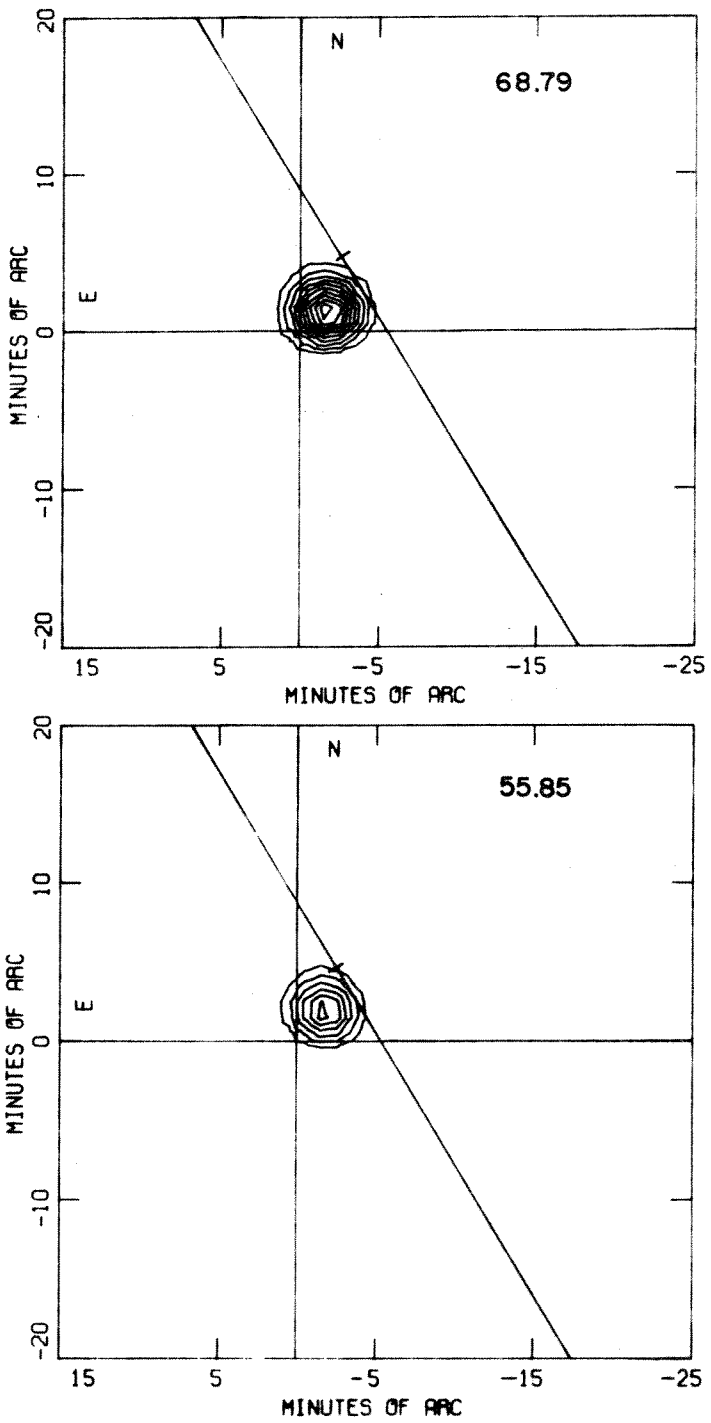

(TOP): Fig. 3-10. Sgr B2 maser emission at 68.79 km/s. Contour interval is 20K.

(BOTTOM: Fig. 3-11. Sgr B2 maser emission at 55.85 km/s. Contour interval is 10K.

Within the errors, the emission in channels 33 and 36 come from the same position, indicating that the velocity spread of the 55 km/s source is comparable to that at 69 km/s. The fitted diameters are consistent with that for a point source and the angular resolution of the maps. The value of the flux density is obtained by calculating the flux from a gaussian of the fitted width and central brightness temperature, namely

$$S = \frac{2kT(max)}{\lambda^2} \cdot \pi\sigma^2$$

where σ is the dispersion of the gaussian.

Raimond and Eliasson (1969) find that the 1667 MHz emission at 69.0 km/s is located at coordinates: R.A.(1950) = $17^h44^m10\overset{s}{.}7 \pm 0\overset{s}{.}4$, Dec.(1950) = $-28^o22'50" \pm 3"$ which agrees very well with the fitted value for channel 24. They do not report any other positions for 1667 MHz emission because of their poor sensitivity. It is interesting to note, though, that they list coordinates for emission between 59.0 and 62.5 km/s in the 1665 MHz line, giving R.A.(1950) = $17^h44^m10\overset{s}{.}5 \pm 0\overset{s}{.}4$, Dec. (1950) = $-28^o22'15" \pm 3"$. This position is only 14" from that for channel 33, and given the poor signal-to-noise ratio of their spectrum for that feature, a positional coincidence may be possible. The velocity difference between that 1665 MHz feature and channel 33 is some 4 km/s, however. In any case, there is no doubt that the emission spikes in channels 24 and 33 arise from physically distinct regions. The angular separation of the two sources is 44 arcseconds, which corresponds to a linear dimension of 2.1 parsec

at an assumed distance of 10.0 kiloparsecs. The channel 24 position also agrees with those of Manchester, et al. (1969) for the 1665 MHz line; their velocity coverage does not extend below +65 km/s, however.

Maps of Optical Depth--Sgr B2

We consider now the contour maps of optical depth, computed from equation (3-4), for the Sgr B2 region. As indicated earlier, a small additive correction to the brightness temperature of the maps has been included to account for the error in the zero level of the temperature scale, due to the extended galactic background. The amount of this correction is 7 K , estimated from the difference between the flux of the single-dish spectrum and that of the integrated map. The computation of optical depth is cut off at the 10% contour of the continuum brightness distribution. As in the case of Sgr A, the maps show a heavy line around the contours, which represents the cutoff level of the continuum. The calculation was also cut off if the optical depth exceeded 3.0, an opacity of 0.95. A selection of optical depth contour maps of Sgr B2 are shown in Figure 3-12. This sample was chosen to display the individual absorption clouds such that each is shown at or near its velocity of greatest opacity. The velocity is indicated for each map; the contour interval is 0.1 in optical depth, except for velocities 64.47, 61.60, 57.28, and 52.96 km/s, for which the contour interval is 0.25. The numbered lines on the maps indentify the individual clouds which will be summarized in tabular form below. We consider briefly the individual maps, in order of decreasing velocity.

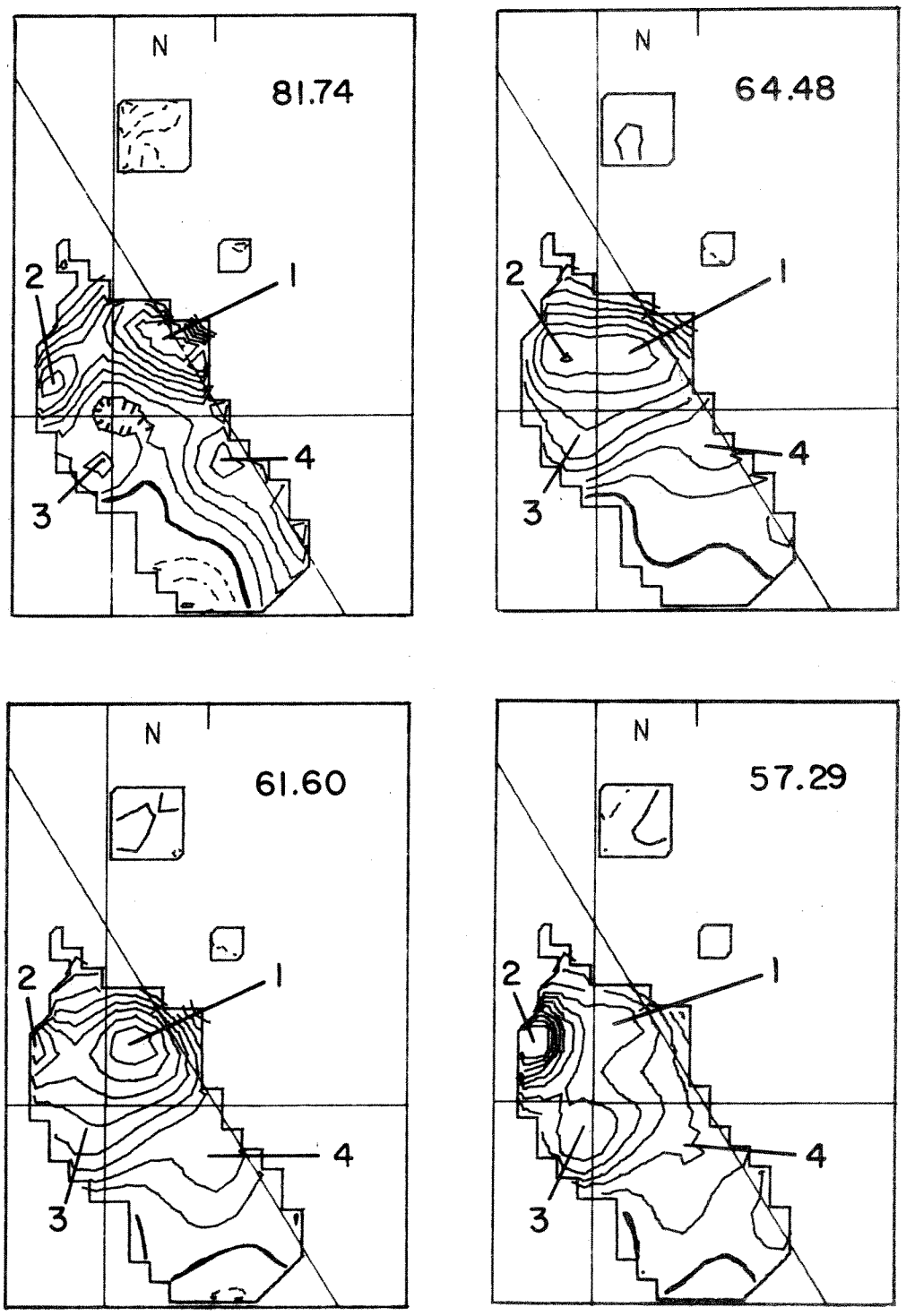

Fig. 3-12. Contour maps of optical depth for Sgr B2. Velocity in km/s is in the upper right. Zero contour darkened. Contour interval is 0.10 for 81.74 km/s, 0.25 for all others. Cloud locations indicated by numbered lines.

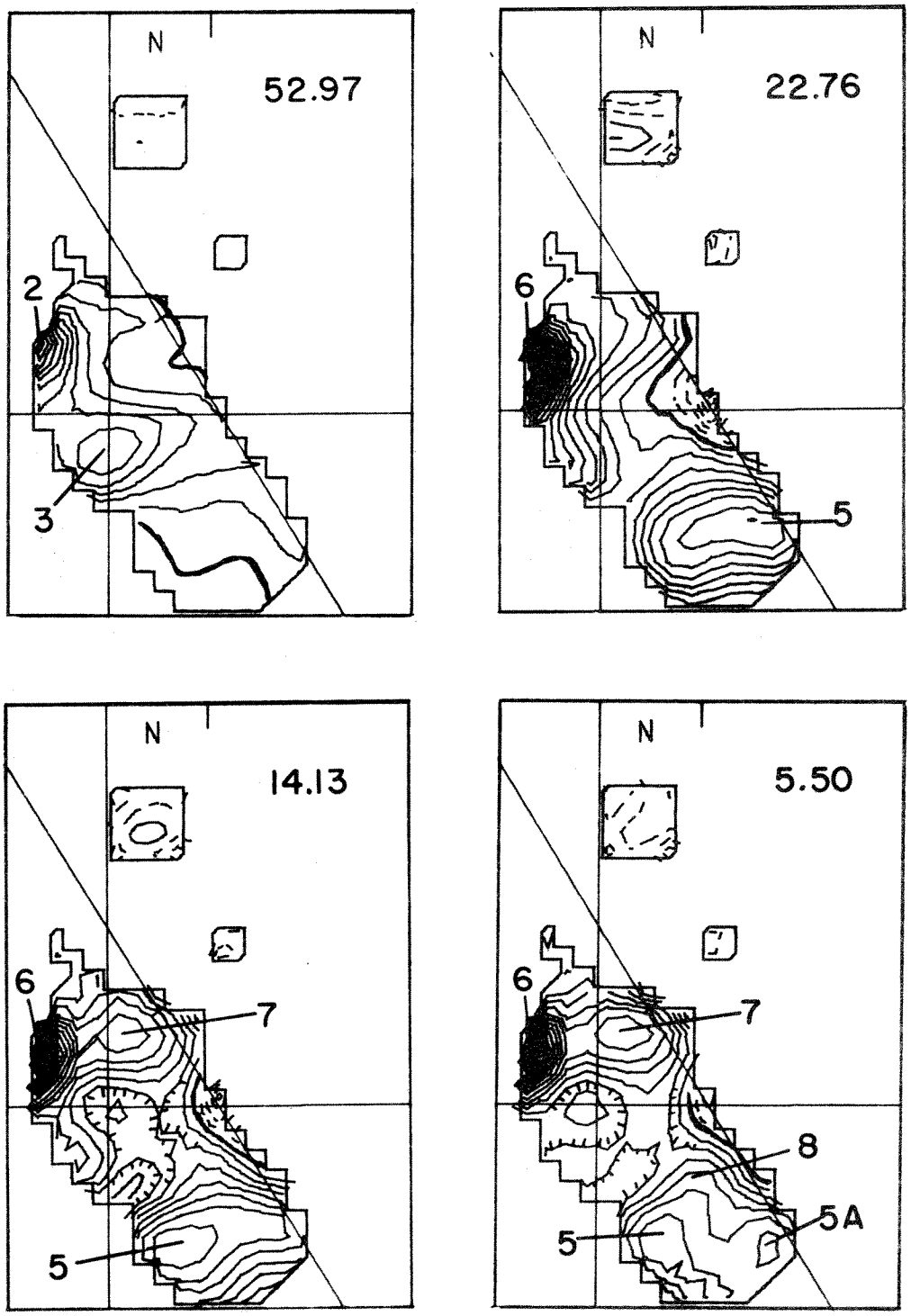

Fig. 3-12 (cont'd.) Contour interval is 0.25 for 52.97 km/s, 0.10 for all others.

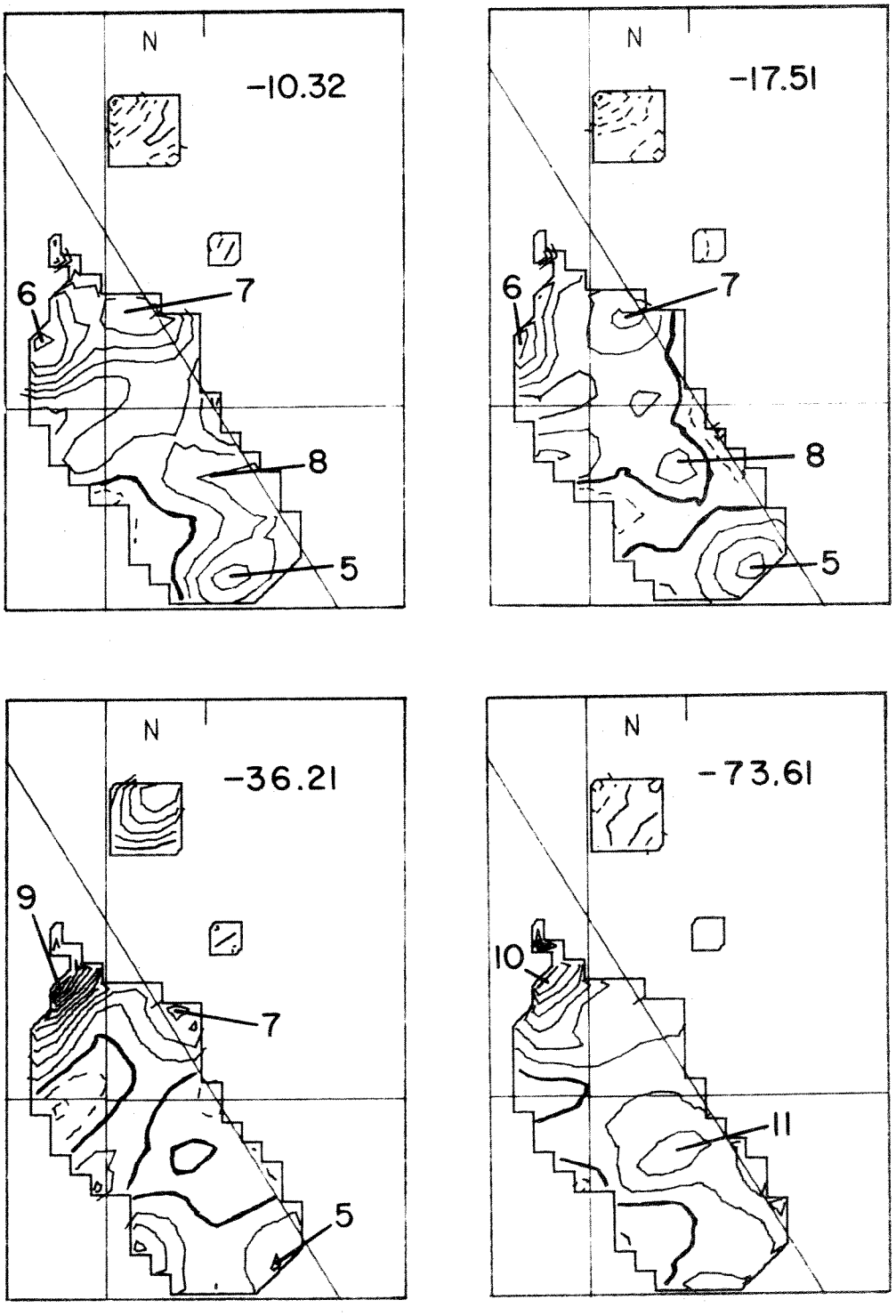

Fig. 3-12 (cont'd.) Contour interval is 0.10

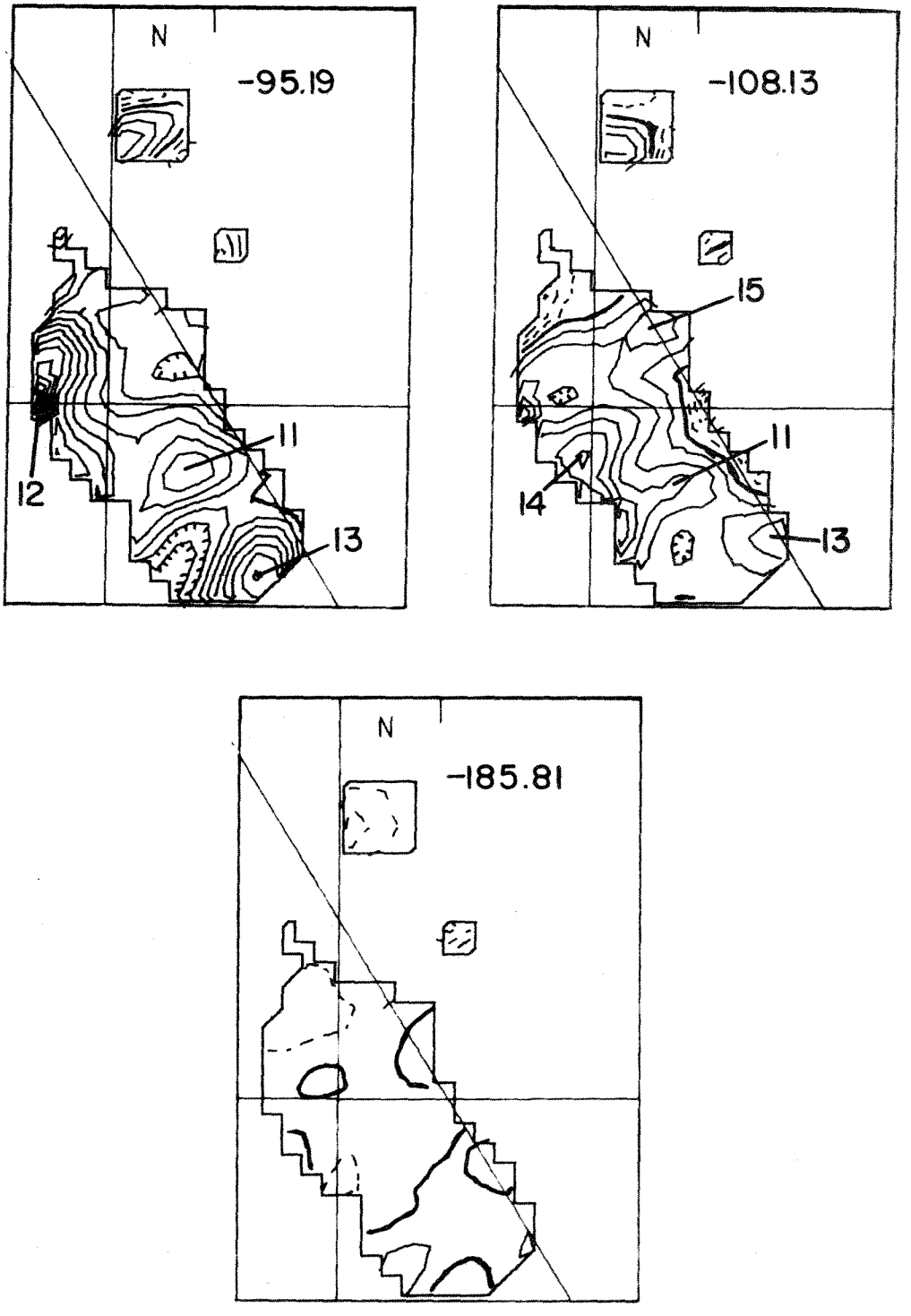

Fig. 3-12 (cont'd.) Contour interval is 0.10

The map for 81.73 km/s shows four clearly separated regions of absorption. Cloud 1 is centered at $l = 41'$, $b = -1'$, and has a peak optical depth of 0.9. Cloud 2 is centered some 5' south of cloud 1 in galactic latitude, and has a maximum optical depth of 0.6; cloud 3 is at the same latitude as cloud 2, but is displaced to lower longitude by 5', and has a peak optical depth of about 0.2. Finally, cloud 4 is centered at $l = 35'$, $b = -1'$, with a peak value of 0.5. Cloud 4 appears to be elongated in the direction of the galactic equator and away from G0.7-0.0. At the velocity 64.47 km/s, the optical depth map has a contour interval of 0.25; the same four features are present, but show much stronger absorption. Cloud 2, with $\tau = 2.03$, is the most intense, and appears to blend with the contours of cloud 3, which is less distinct than in the previous example. Cloud 1 shows twice the optical depth of the previous map, but 4 is only slightly changed. The map for velocity 61.60 km/s, the velocity of greatest absorption in the single-dish spectrum (Fig. 3-7) has cloud 1 the dominant absorber, with $\tau = 2.22$. Cloud 2 is shifted to the edge of the map, where it has a peak $\tau = 2.1$, essentially unchanged from the previous map. Also, clouds 3 and 4 are little different from their previous positions and opacities.

Moving to the velocity 57.28 km/s, cloud 1 is substantially lower in optical depth ($\tau = 1.3$) while cloud 2, near the edge of the continuum, shows an absorption greater than the maximum allowable optical depth of 3.0, at which point the calculation is cut off. The peak absorption is at the edge of the continuum, where noise is the most serious, so the true value of τ is rather uncertain. (A full

discussion of the uncertainty in the calculated optical depths is given at the end of this chapter.) Cloud 3 is also more distinct, with a peak value of $\tau = 1.5$. Cloud 4 has decreased in size and opacity, with $\tau = 0.5$. At 52.96 km/s, cloud 2 is concentrated on the edge of the continuum, still with very high maximum optical depth. The center of the cloud is evidently beyond the contour limit of the maps. Cloud 3 is nearly unchanged from the previous map, while clouds 1 and 4 have virtually disappeared.

The optical depth maps for lower velocities show features 2 and 3 fading out until 3 has disappeared. Beginning about +35 km/s, the first strong absorption in front of G0.5-0.0 becomes visible in the feature designated cloud 5. Cloud 2, however, continues to show large optical depths, decreasing only to about $\tau = 1.5$. Spectra 10 and 11 of Figure 3-9 indicate that there are two absorption components at this position, one at a velocity of 55 km/s, the other at 25 km/s. This very broad spread of velocities has therefore been divided into two clouds, cloud 6 being nearly coincident with cloud 2. The map at 22.76 km/s shows cloud 6 to be comparable to cloud 2 in optical depth and extent, but displaced some two arcminutes south in declination from the cloud 2 maximum. (Note that the contour interval here is again 0.10.) This map indicates that cloud 5 has a more complex shape than 1 through 4. The deepest absorption lies on a slightly curved line extending roughly perpendicular to the galactic plane and directly across the continuum peak of G0.5-0.0. It is cloud 5 that produces the deep +25 km/s absorption lines in spectra 14 through 18 of Figure 3-8. Cloud 5 is physically distinct from the clouds which

cause the high-opacity postive-velocity lines in the spectra of G0.7-0.0.

The structure and position of cloud 5 are velocity dependent. Shifting to the map for 14.13 km/s, the cloud center moves perpendicular to the galactic plane, to a lower latitude, though still elongated as before. The feature appears as an unresolved, or barely resolved double, but the map does not show a clear separation of components. A new cloud shows up clearly on the 14.13 km/s map, near the position of cloud 1 at higher velocities. Designated cloud 7, it has its peak absorption, $\tau = 0.7$, at $l = 42'$, $b = -2'$. At 5.50 km/s, cloud 6 is still the deepest absorption, but lying at the edge of the map, its true optical depth is uncertain. Cloud 7 is unchanged from the previous map. Cloud 5, however, appears to be resolved into two peaks, both at nearly the same declination. The western component is identified as 5A. Note, though that the optical depth between 5 and 5A does not even approach zero. The two peaks are quite probably associated with a single large-scale cloud, albeit not one with a simple structure. There is evidence for a weak unresolved component centered three arcminutes north of 5 and 5A, and midway between them in right ascension. At negative velocities this component stands out more clearly. In the map at -10.32 km/s, it is identified as cloud 8, the weakest absorption feature to be catalogued. Clouds 5 and 5A have merged to form a single elliptical component, which is shifted back toward the galactic plane, with a center at $l = 28'$, $b = -4'$ and a peak opacity of 0.4. Cloud 6 is greatly reduced in opacity, with $\tau = 0.63$ at the maximum, while cloud 7 is down to $\tau = 0.5$ and has shifted its center by one minute of arc to higher galactic longitude.

Considering next the map for -17.51 km/s, we see that cloud 5 has shifted closer to the galactic equator, lying now at the southwest end of the continuum. All the features--5, 6, 7, and 8--have optical depths less than their peak values. The map for -36.21 km/s shows clouds 5 and 6 about to disappear off the edges of the continuum. In the northeast corner of the continuum, a strong absorption has appeared. Examination of spectra 9 and 10 of Figure 3-9 shows that this represents a separate feature, centered at a velocity of about -36 km/s. It is designated as cloud number 9.

Between -36 km/s and -74 km/s, no significant new absorption features appear in the map. The numbered spectra 9 and 10 of Figure 3-9 referred to above show two components in velocity at the northeast corner of G0.7-0.0. The one centered at -36 km/s has been assigned number 9; that at -75 km/s is number 10. Cloud 10 is indicated in the map at velocity -73.61 km/s. Also present is cloud 11, just beginning to show up at coordinates $l = 34'$, $b = -3'$. At -95.18 km/s cloud 11 is clearly delineated, with a peak optical depth of 0.7. Two other clouds are also present: 12, at the extreme eastern edge of the continuum; and 13, lying in the southwest end. These objects are major absorption features and account for most of the broad negative-velocity absorption component of the Sgr B2 spectrum.

The center of cloud 13 shifts slightly with velocity, until at -108.13 km/s it is seen to have moved almost off the map. Cloud 11 is weaker at this velocity and 12 has nearly disappeared. A new feature, less intense than 12, is designated cloud 14 and is located four arcminutes south and west of 12. Finally, a relatively weak absorption,

cloud 15, appears, offset by 3 arcminutes northwest of the continuum peak of G0.7-0.0. Its peak optical depth is 0.25. Beyond -108 km/s, clouds 11, 13, 14, and 15 fade out, without any new features appearing, so that the map shows no absorption greater than the noise, for velocities below -150 km/s, in agreement with the single-dish spectrum. The map at -185.80 km/s demonstrates this absence of absorption, where over the whole map, $\tau = 0.0 \pm 0.1$.

The spatial and velocity relationships of the fifteen distinguishable OH clouds in the Sgr B2 region are summarized in Figures 3-13 and 3-14, and in Table 3-8. Maps of the continuum brightness temperature are shown with the location of the absorption maximum for each cloud represented by the black dot. The cloud number is given, followed in parentheses by the velocity in km/s of the maximum absorption. These velocities were determined from the point spectra of Figure 3-9. For clouds 5 and 13, the position of maximum absorption is a function of velocity; in these two cases, the maximum optical depth over the range of velocities in the cloud is shown by a series of dots. The map of Figure 3-13 shows clouds at positive velocities, while Figure 3-14 shows the ones at negative velocities. (The figures are separated for the sake of clarity.) The size and shape of each cloud is indicated by the heavy line, which is drawn to follow the contour at half the value of the maximum optical depth. In the case of blended features, the line represents the best estimate, consistent with a smooth cloud outline, of the half-maximum optical depth.

The measured properties of the fifteen absorption clouds are summarized in Table 3-8, which draws both on the maps of optical depth

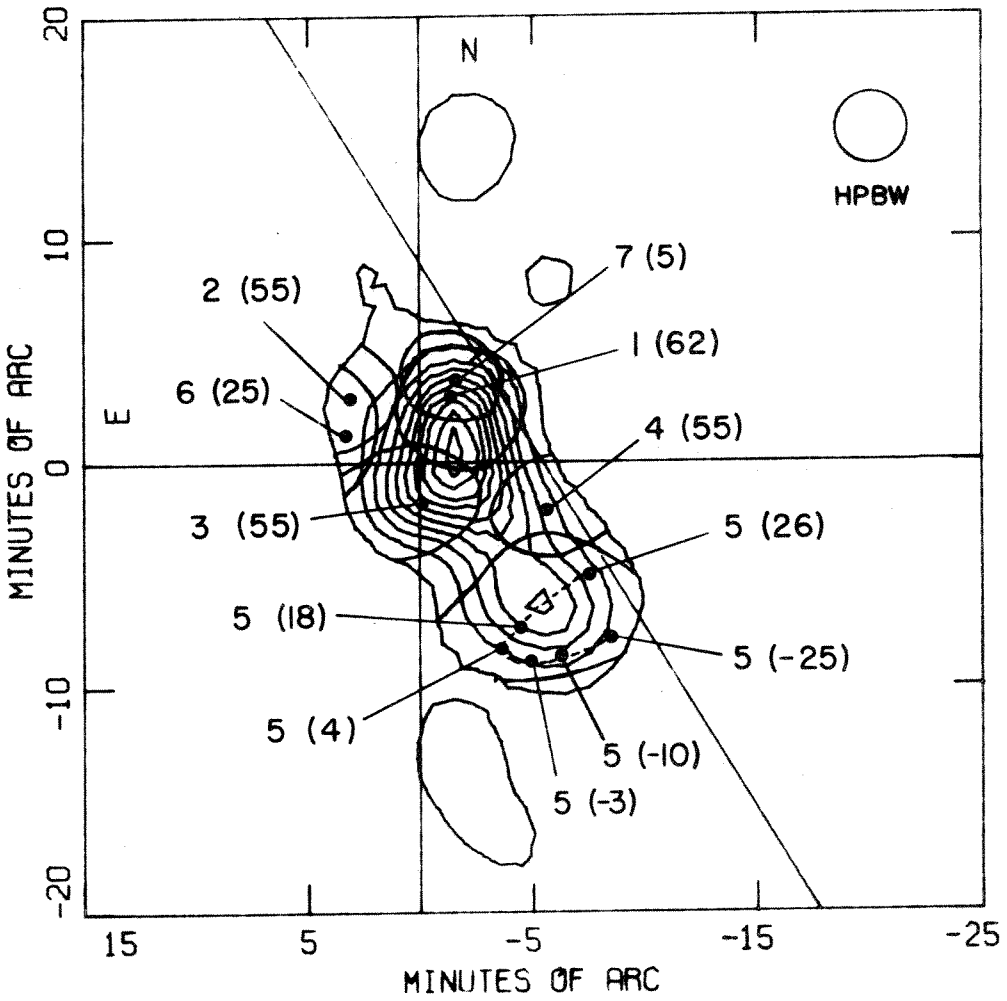

Fig. 3-13. Locations of discrete positive-velocity clouds in Sgr B2, from Table 3-8. Cloud number is followed in parentheses by velocity of maximum absorption in km/s.

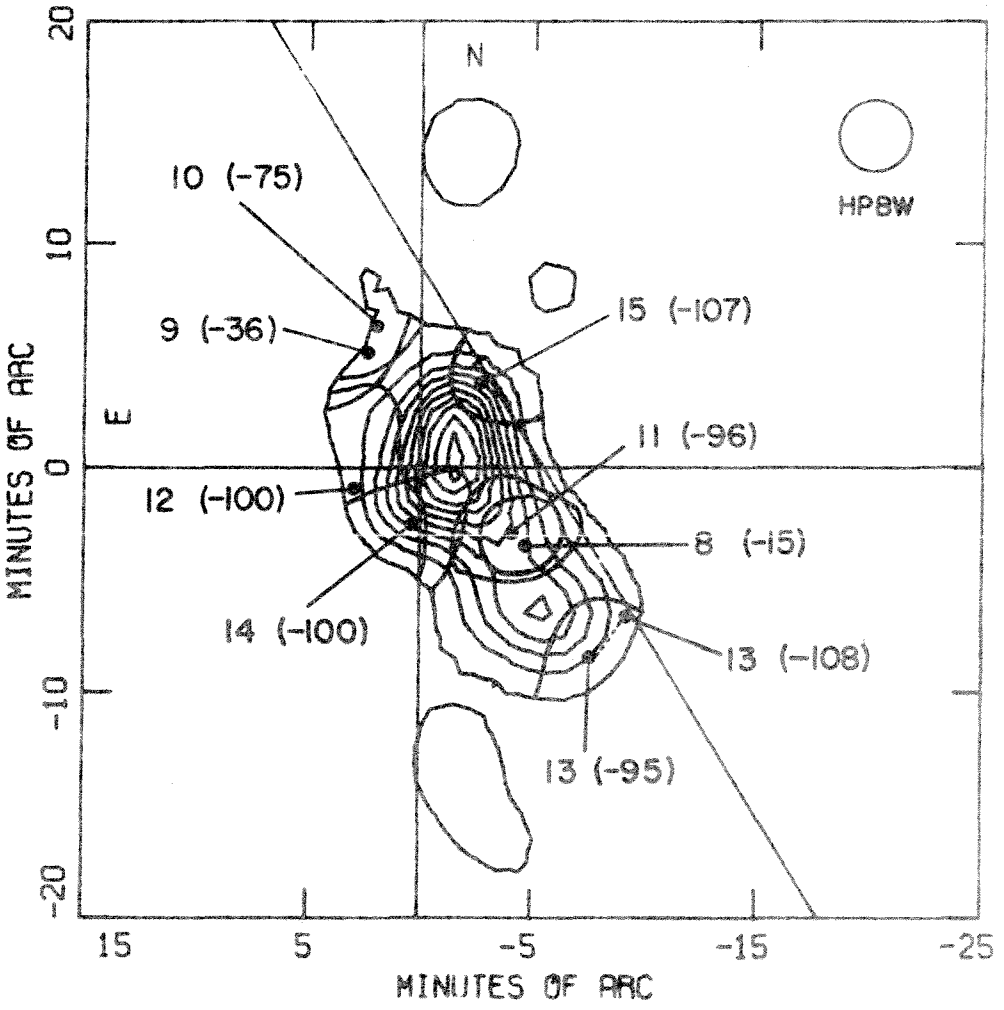

Fig. 3-14. Locations of discrete negative-velocity clouds in Sgr B2, from Table 3-8. Cloud number is followed in parentheses by velocity of maximum absorption in km/s.

Table 3-8

Cloud No.	V_o (km/s)	$\Delta V_{1/2}$ (km/s)	$\Delta\alpha$ (')	$\Delta\delta$ (')	l (')	b (')	τ_{max}	Diam. (')	Spect. Ref.No.	Notes
1	+62	25(3)	-1.5	+3.0	41.0	-2.0	2.22	5.5	6	
2	+55	40(10)	+3.0	+3.0	43.0	-5.5	3.0	4	11	E
3	+55	45(10)	0.0	-1.5	37.5	-5.5	1.5	5.5	12,13	
4	+55	40(5)	-5.5	-2.0	34.0	-1.0	0.6	5	13,18	
5	+15	35(5)	-6.0	-7.0	29.5	-3.5	0.8	6 10	14-17	V
6	+25	45(10)	+3.0	+1.0	42.0	-6.5	3.0	5	11	E
7	+ 5	40(8)	-1.5	+3.5	41.5	-1.5	0.8	4	8,6	
8	-15	30(10)	-4.5	-3.5	34.0	-2.5	0.2	4	18	
9	-36	30(10)	+2.0	+5.0	45.0	-4.0	1.4	?	9,10	E
10	-75	25(10)	+2.0	+6.5	45.5	-3.0	0.7	?	9	E,Cf
11	-96	20(5)	-4.0	-3.0	35.0	-2.5	0.7	6	18	
12	-100	22(5)	+3.0	-1.0	40.0	-7.5	1.2	9	12	E,Cf
13	-98	22(5)	-7.5	-8.5	28.0	-2.5	0.9	5	16,17	
14	-100	22(5)	+0.5	-2.5	37.5	-6.0	0.65	5	12	V
15	-107	15(5)	-2.5	+3.5	41.0	-0.5	0.25	3	9	

Notes: E = extends beyond continuum edge; V = position changes with velocity; Cf = spectrum confused by adjacent features.

and on the spectra at points in the maps. The first column gives the cloud number; columns 2 and 3 list the velocity of maximum absorption and the linewidth at half-maximum opacity. Columns 4 and 5 give the right ascension and declination offsets from the origin (the center of the compass rose) for the cloud centers, while columns 6 and 7 list the corresponding galactic coordinates. The maximum optical depth of the cloud is in column 8, and the diameter at half-maximum optical depth is in column 9. Column 10 indicates the spectrum number in Figure 3-9 which is nearest the cloud maximum. The last column contains cautionary notes to observe in interpreting the tabulated numbers.

Uncertainties of the Measured Quantities

The errors in the synthesized maps are caused by several factors including receiver noise; random errors of measurement; systematic errors in calibration of the visibility function; computational noise, or round-off error; and residual sidelobes not removed by the cleaning process. Of these, the errors in calibrating the visibility data, and the residual sidelobes not removed by cleaning are the most important in this work. The Sagittarius sources have such high brightness temperature that receiver noise is generally a negligible source of uncertainty in the maps. Random errors of measurement, such as an incorrect entry in the computer controlling the interferometer, were usually obvious in the reduced data, and were deleted from the Fourier inversion. Hence, this is not a significant source of error. Computational noise is also negligible since the inverted maps were stored in half-

word integer format, providing 16 bits of information per point. Round-off error is less than one part in 600 at one percent of the maximum brightness temperature.

A simple calculation shows that the maps are not sensitivity limited. The rms fluctuation in brightness temperature over the synthesized map due to receiver noise can be estimated (Christiansen and Högbom 1969; Shostak 1972) by the formula:

$$\Delta T_{B\ rms} = \frac{T_{r+s}}{\sqrt{\beta t}} \cdot \frac{A_{dish}}{A_{synth}}$$

where T_{r+s} is the total noise temperature due to the receiver and the radio source; β is the IF bandwidth, here 4×10^3Hz; t is the total integration time for all data points in the Fourier inversion and A_{dish} and A_{synth} are the angular areas of the telescope primary beam and the synthesized beam. A conservative estimate of t for this observational program is two hours per spacing per source, or about 5×10^5seconds. The ratio of beam areas is the square of the ratio of half-power diameters: $(24/3.25)^2 = 55$. The total system temperature on Sgr A is about 130 K , and 100 K on Sgr B2. Then equation (3.5) yields the values:

$$\Delta T_{B\ rms} = 0.5\,K \text{ for Sgr A}$$
$$= 0.4\,K \text{ for Sgr B2}$$

Relative to the maximum continuum brightness temperature, the rms error due to receiver noise is 0.03% for Sgr A and 0.3% for Sgr B2.

The errors in the cleaned maps are larger than these values because calibration errors and residual sidelobes are of overriding importance. The uncertainties in the narrowband fringe amplitudes and phases include important contributions due to the calibration errors, as already discussed in Chapter 2 (see Table 2-3). To this must be added the error due to residual sidelobes not eliminated by the cleaning process. There is no simple analytical means of estimating the uncertainty due to the cleaning process, because the errors in the map have a high degree of correlation from one point to another. As a result, the errors are not related in any simple way to the brightness distribution function. The most satisfactory means of determining the noise level in the final maps is to calculate the rms fluctuation in the value of the brightness temperature at points where the true value is known. This computation was done for the outer portions of the map grid, where the brightness distribution should be zero. (The maps were not corrected for the primary beam, which does not affect the cleaning process.) The mean and standard deviation of T_b were computed for the five outermost rows of the map grid along all four edges, for one-quarter of all the maps produced. In essentially all cases, the mean value was zero to well within one standard deviation. The noise fluctuations were constant in amplitude over the outer regions of the map, independent of position. The standard deviation depends slightly on the intensity of the peak brightness temperature. Average values for the rms deviations as a function of maximum continuum brightness are summarized here:

Table 3-9

Residual Sidelobe Levels of the Cleaned Maps

Source	T_b(max)	ΔT_b	Rel. Error
Sgr A	1900 K	10 K	0.5 %
	1100 K	8 K	0.7 %
Sgr B2	160 K	1.6 K	1.0 %
	120 K	1.6 K	1.3 %
	60 K	1.8 K	3.0 %

Assuming the noise level due to residual sidelobes is constant over the whole map, then the rms error in brightness temperature is about 10K for Sgr A and is not worse than 1.8 K for Sgr B2.

Besides the estimation of the noise level in a single map, we are interested in the noise in the spectrum of brightness temperature with velocity, for any point on the map grid. The standard deviations of the brightness temperature in the continuum channels (as previously defined) were computed at some 100 map points for Sgr A and 150 points for Sgr B2. The standard deviations were plotted versus mean brightness temperature. The resulting graphs were approximately linear with some scatter about the mean. The graph for Sgr B2 was best fitted with two line segments, since the noise level was somewhat smaller at the lower continuum levels. A least-squares estimate to a straight line gave these results:

$$\sigma_{T_b} = (5.3 + 0.005\ T_b)K \qquad \text{for Sgr A}$$

$$\sigma_{T_b} = \begin{cases} 2.4K\ (T_b/T_b(\max) \geq 0.2) \\ 2.0K\ (T_b/T_b(\max) < 0.2) \end{cases} \qquad \text{for Sgr B2}$$

The most useful form in which to give the uncertainty of T_b is in terms of relative errors. In order to refer easily to the continuum contour map, we tabulate here the relative error, σ_{T_b}/T_b, as a function of the normalized continuum brightness temperature, $T_b/T_b(\max)$, where $T_b(\max)$ refers to the continuum peak. The errors are given both for the mean value of σ_{T_b} and the upper envelope of the scatter of points.

Table 3-10

Relative Errors for Spectra at Map Points

$\frac{T_b}{T_b(\max)}$	Sgr A			Sgr B2		
	T_b	σ_{T_b}/T_b (%)		T_b	σ_{T_b}/T_b (%)	
		mean	max		mean	max
1.0	1900	0.8	1.0	153	1.6	2.0
0.8	1520	0.9	1.0	122	2.0	2.4
0.6	1140	1.0	1.0	92	2.6	3.4
0.4	760	1.2	1.3	61	3.9	5.2
0.2	380	1.9	2.6	31	7.7	10.
0.1	190	3.3	4.6	15	13.	17.
0.08	152	4.0	6.5	-	-	-

Taking the most unfavorable case, at the edge of the optical depth contour maps the relative error in brightness temperature for Sgr A is typically 4.0% and is not worse than 6.5%; in the case of Sgr B2, the

relative error is 13% on the average, and is not worse than 17%.

Since the optical depth maps are calculated from two quantities which are determined by different observations, namely, the five different frequency shifts, it is important to estimate the magnitude of any systematic disagreement between maps at the different frequency shifts. The observations were set up so that the velocity ranges covered by each local oscillator setting overlapped by three channels. Comparison of the channels at identical velocities affords a realistic estimate of the systematic differences between the frequency shifts. The mean and standard deviation of the differenced brightness temperatures were computed for all the overlapping pairs of maps. The average was taken only for those points within the cutoff boundary of the optical depth calculation. The mean difference indicates the systematic error in integrated flux for the whole map. For Sgr A, the mean differences ranged between -15K and +4K; for Sgr B2 the corresponding values were -2.3K and +2.4K. These relatively small systematic differences may produce jumps or discontinuities in optical depth across the ends of the various frequency shifts. The discontinuities are negligible where the brightness temperature is high, while at the edges of the contour maps the systematic changes across frequency shifts are sometimes noticeable.

The purpose of this error analysis is to determine the reliability of the spectra and the maps of optical depth already presented. The optical depth at a given point is

$$\tau = -\ell n(T_{NB}/T_C) \qquad (3.6)$$

where T_C and T_{NB} are the continuum and narrowband brightness temperatures at the given map point. If the error in τ is small, we may write

$$\sigma_\tau^2 = \left(\frac{\sigma_{T_C}}{T_C}\right)^2 + \left(\frac{\sigma_{T_{NB}}}{T_{NB}}\right)^2$$

assuming the errors in T_C and T_{NB} are uncorrelated. Since the continuum map is an average of four narrowband maps, it is reasonable to assume that $\sigma_{T_{NB}} = 2\sigma_{T_C}$. Then we can write

$$\sigma_\tau = \frac{\sigma_{T_C}}{T_C} \left(1 + 4e^{2\tau}\right)^{1/2} \tag{3.7}$$

which is valid for small errors: $\sigma_\tau << \tau$. Expression (3.7) relates the error in optical depth to the relative error in continuum brightness temperature and to the optical depth itself. It should be appreciated that for large τ, the error also becomes large very rapidly. Equation (3.7) is, in fact, not valid for large τ, so that a direct calculation of the error limits is required. The uncertainty in τ, then, depends on the uncertainties in the quotient of continuum and narrowband brightness temperatures, which is given by

$$\sigma_{(T_{NB}/T_C)} = \frac{T_{NB}}{T_C} \left[\left(\frac{\sigma_{T_C}}{T_C}\right)^2 + \left(\frac{\sigma_{T_{NB}}}{T_{NB}}\right)^2\right]^{1/2} .$$

Table 3-11 lists the uncertainty in optical depth σ_τ, as a function of $\sigma(T_{NB}/T_C)$ and the optical depth itself. The approximate range of continuum brightness temperatures for the two sources, expressed as fractions of the maximum, are given to indicate the regions of the

optical depth maps for which each line of the table is applicable.

We see that above the 80% contour of the Sgr A continuum map, the top line applies. An optical depth of 0.5 has an associated uncertainty of ± 0.02. For Sgr B2, an optical depth of 1.0 at a point above the 80% contour has an error of ± 0.06. The error in optical depth is largest near the edges of the continuum, of course. The error in τ at the 8% cutoff level of the Sgr A continuum is ± 0.09 for $\tau = 0.5$. In the case of Sgr B2, an optical depth of 1.0 at the 10% cutoff has an associated error of (+0.33, -0.24). We also note that for Sgr B2, low optical depths near the edge of the maps are very uncertain, such that for $\tau = 0.1$, the relative error exceeds 100%. Any weak features near the border of the Sgr B2 optical depth maps must be regarded with great caution. Strong features will certainly be real, but with significant uncertainties in the value of the maximum absorption. In particular, an optical depth of 3.0 (corresponding to 95% opacity) at the edge of Sgr B2 has an upper limit of infinity, since the noise level in T_{NB} exceeds the brightness temperature in the absorption line.

To sum up, the uncertainties in these numerical results are due primarily to calibration errors and to residual noise (sidelobes) not removed by the cleaning process. The rms noise level of sidelobes is less than 1.8K per grid point for Sgr B2, and is about 10K for Sgr A. The brightness temperature spectra at a given map point have errors of the same magnitude. Before correction for the primary beam, the rms noise on a Sgr A spectrum is $(5.3 + 0.005\ T_c)$K where T_c is the

Table 3-11

σ_τ as a Function of τ and $\sigma_{(T_{NB}/T_c)}$

$\sigma_{\frac{T_{NB}}{T_c}}$	T_c/T_c(max)		σ_τ						
	Sgr A	Sgr B2	τ=0.1	0.2	0.5	1.0	1.5	2.0	3.0
0.01	0.8-1.0	-	.01	.01	.02	.03	.06	.07	.21
0.02	0.5-0.8	0.8-1.0	.02	.02	.03	.06	.10	.15	$^{+.50}_{-.34}$
0.05	< 0.2	0.4-0.8	.05	.06	.09	$^{+.16}_{-.13}$	$^{+.27}_{-.20}$	$^{+.46}_{-.31}$	$^{+\infty}_{-.7}$
0.10	-	0.1-0.4	.11	.12	$^{+.19}_{-.15}$	$^{+.33}_{-.24}$	$^{+.61}_{-.37}$	$^{+1.35}_{-0.55}$	$^{+\infty}_{-1.1}$

continuum brightness temperature. For Sgr B2 the noise level is 2.4K. The error in calculated optical depth is a function of the continuum brightness temperature and the optical depth itself. The best estimate of σ_τ is summarized in Table 3-11, which should be used in interpreting the contour maps of optical depth presented above.

Chapter 4

KINEMATICAL INTERPRETATION

Sgr A--the "+40 km/s" Cloud

Of the several features in the 1667 MHz OH spectrum for Sgr A, the one with maximum absorption at about +40 km/s is clearly dominant. The spectra at individual map points which we discussed in Chapter 3 show that the +40 km/s absorption is the only major feature concentrated in front of the compact continuum source. Other observers have found that the spectra of a wide range of molecules also have significant absorption or emission in the velocity range of this object. The 4830 MHz formaldehyde line has a strong absorption feature which agrees in velocity and width with the λ18 cm OH spectrum. Several authors (Zuckerman, et al. 1970; Scoville, et al. 1972; Gardner and Whiteoak 1972; Fomalont and Weliachew 1973) have mapped the distribution of formaldehyde absorption with both single-dish and interferometric techniques, providing the most comprehensive set of molecular observations with which we can compare the OH results of this work. More recently, the λ2.6 mm emission spectrum of carbon monoxide has been mapped in the galactic center region by Penzias, et al. (1971) and Scoville, et al. (1973). The CO spectra have their highest brightness temperature in the velocity range +25 to +74 km/s at a galactic longitude of about +0.'1; this emission is believed to come from the same molecular cloud that produces the OH absorption. Cheung, et al. (1968) discovered ammonia emission at about +23 km/s in the vicinity of Sgr A. Their results indicate a concentration of NH_3

lying several minutes of arc lower in galactic latitude than the center of the OH absorption. A large number of other, more exotic molecules have also been found near Sgr A and at a velocity of about +40 km/s.

The 21 cm neutral hydrogen absorption spectrum of Sgr A shows only a modest feature centered at +40 km/s (Sandqvist 1970). This fact has been interpreted as indicating a severe deficiency of neutral atomic hydrogen in the cloud, the hydrogen presumably existing in molecular form. (Some unpublished interferometric results by the author show, however, that the depth of the HI absorption at +40 km/s increases substantially when Sgr A is observed with a fringe spacing of six minutes of arc, so that the extended background is resolved out. This increase in opacity implies that the hydrogen density of the +40 cloud is larger than the single-dish observations indicate.)

The multitude of molecular species present, the high opacity of the cloud, and its proximity to the region which we believe to be the dynamical center of the Galaxy, all suggest that this object is unique among interstellar clouds. In the first part of this chapter we examine the kinematics of the gas and deduce certain physical properties of the cloud.

The +40 km/s cloud is visible in the optical depth contour maps of Figure 3-6 through the range of velocity from +75 to +18 km/s. The position of the maximum absorption shows a clear velocity dependence. To examine this dependence quantitatively, we consider the three graphs of Figure 4-1. The galactic coordinates of the

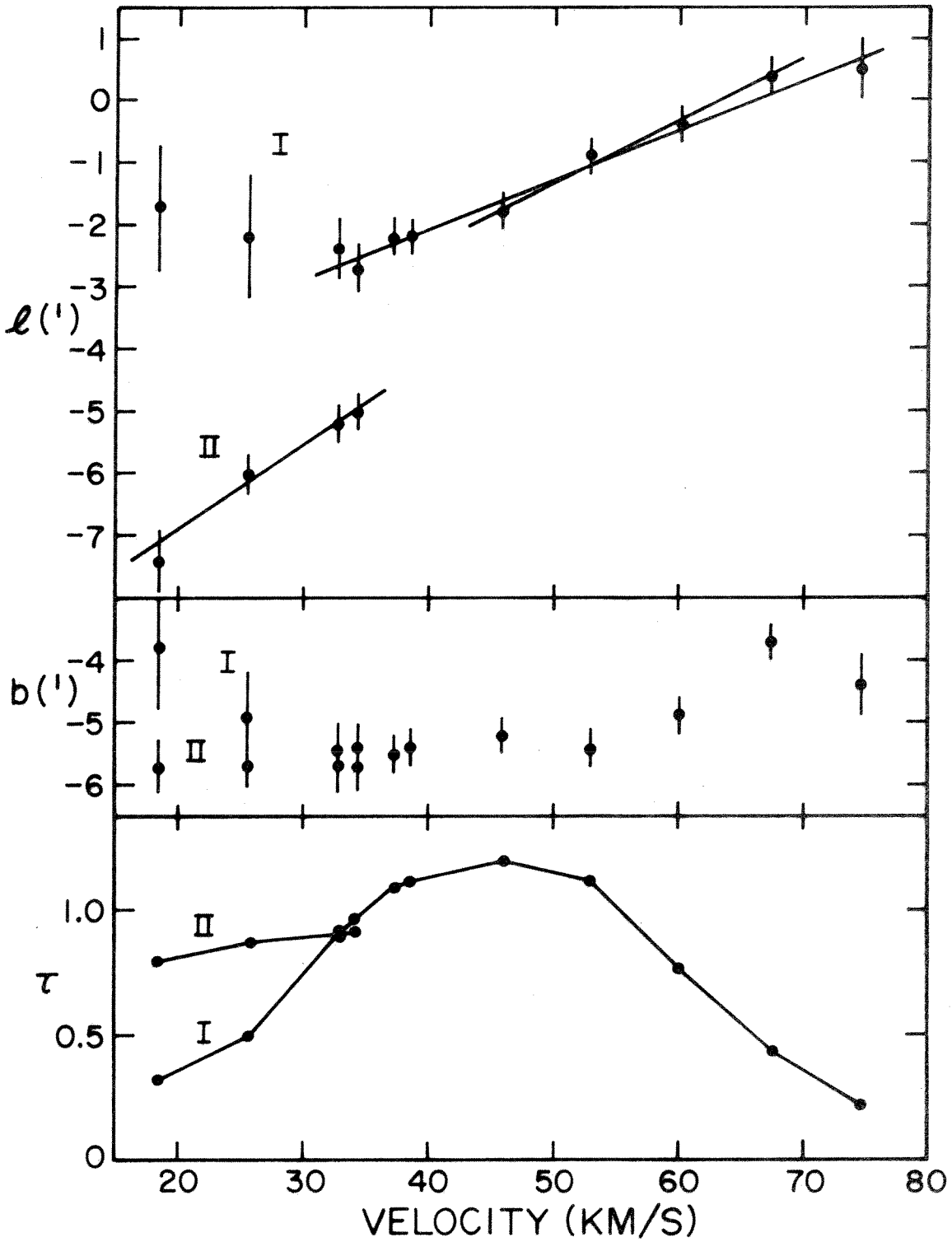

Fig. 4-1. Galactic longitude, latitude, and peak optical depth as a function of velocity, for the centers of components I and II in the Sgr A +40 km/s feature.

position of maximum opacity, and the value of the optical depth at that point are plotted against observed radial velocity. The positions and optical depths were estimated from the maps in Figure 3-6 (as well as some maps not included there); the values have been summarized previously in Table 3-4.

The graphs immediately suggest three conclusions:

(1) The broad +40 km/s absorption occurs in two physically distinct components: One, labelled "I", which dominates the spectrum above 30 km/s, and a second, designated "II", which is strongest below 30 km/s.

(2) The high velocity feature shows a large, nearly constant gradient of velocity with galactic longitude for velocities greater than 32 km/s. The second, low-velocity component also has a constant velocity gradient with longitude, but its value is smaller.

(3) Neither component has a significant velocity dependence in galactic latitude.

The plot of optical depth versus velocity shows that the peak optical depth of the stronger component has an approximately gaussian shape, with a center velocity of about +45 km/s and a full-width at a half-maximum of 36 km/s. The maximum optical depth of component I is 1.25. The weaker, low-velocity absorption has nearly a constant peak optical depth of about 0.9. The optical depth of component II at velocities above 35 km/s is very difficult to estimate, since the absorption structure is dominated by the other component. It appears that the optical depth of II must drop off very quickly above 35 km/s, since the longitude of component I shows no evidence of "pulling", but

forms a nearly straight line with velocity. If component II had an appreciable opacity at 40 km/s, one would expect to see a bulge toward negative values in the run of longitude coordinates, but this is not observed.

The graphs of l vs. V and b vs. V support the interpretation that the component I cloud is in approximately rigid-body rotation. (This hypothesis was suggested originally from lunar occultation observations of the 1667 MHz OH line by Kerr and Sandqvist (1968). Other observations have also shown the presence of a velocity gradient; we will compare the present results with these others later.) The data in the l-V graph of Figure 4-1 lie nearly on a straight line for velocities above 32 km/s, for component I. A straight line fit to all the points has a slope of 12.5 km/s per arcminute. However, there is some indication that the longitude of maximum opacity is constant with velocity below 40 km/s--the curve seems to flatten out. The point at 74.5 km/s may show a similar effect. The error bars on these end points are also larger than those in the center, so a straight line was fitted to the four points between 45 and 70 km/s. The resulting slope was 10.0 km/s per arcminute. The points between 18 and 35 km/s designated as component II fit well to a line with a slope of 7.5 km/s per arcminute. The fitted lines are shown in Figure 4-1.

The plot of b vs. V shows a slight indication of a velocity gradient in latitude for component I. The direction of the total velocity gradient, however, is nearly parallel to the galactic equator, with a deviation not greater than 20^{o}. Thus, the contribution of the latitudinal component to the total gradient is less than 10%.

For component II, the latitude is constant at -5.'7, independent of velocity. The rotation axes of both components are approximately perpendicular to the galactic plane.

It is elementary to show that for a gaseous cloud in solid-body rotation, the observed radial velocity along any line of sight through the cloud is proportional to the linear displacement of that line from the axis of rotation. If the axis of rotation is perpendicular to the line of sight, we have for the radial velocity:

$$v_r = \omega \cdot x$$

where ω is the angular velocity of rotation and x is the displacement from the center of rotation. Assuming that the OH gas cloud is in solid-body rotation about an axis perpendicular to the line of sight, the measured slope in the l-V graph will give ω directly. We distinguished two cases, which represented the maximum and minimum slopes that could reasonably be assigned to the points. Then we have:

(1) Slope = 10.0 km/s per arcmin $\qquad 45 < v_r < 70$

(2) Slope = 12.5 km/s per arcmin $\qquad 32 < v_r < 75$

If the cloud is at 10.0 kpc, we have these angular velocities:

(1) $\omega = 1.1 \times 10^{-13} s^{-1}$

(2) $\omega = 1.4 \times 10^{-13} s^{-1}$

Taking the mean of these values, the rotational period of the cloud is

$$P = \frac{2\pi}{\omega} = 1.6 \times 10^6 \text{years} \pm 12\% \ .$$

If the cloud is gravitationally bound within a radius R, then the mass of the cloud inside a sphere of radius R is (neglecting turbulent motions)

$$M = \frac{\omega^2 R^3}{G}$$

so that

(1) $M = 0.19 \times 10^{-18} R^3$ g

(2) $M = 0.29 \times 10^{-18} R^3$ g

where R is in centimeters. The total mass estimated in this way is very sensitive to the choice of R. The major diameter of the cloud at half-maximum optical depth is 7' (Table 3-4), so we will assume here that R = 10 pc (3'.5 at a distance of 10 kpc). Then for the two cases

(1) $M = 2.9 \times 10^6 M_\odot$

(2) $M = 4.6 \times 10^6 M_\odot$

are the reasonable limits on the total mass inside a sphere of radius 10 pc. A value of 10 pc for R is a conservative estimate: The spectra shown in Figure 3-5 at positions 8 and 12, as well as all spectra in between, show strong absorption at +40 km/s, indicating that the cloud extends over at least 9 minutes of arc in galactic longitude, which corresponds to a linear dimension of 26 pc. In the contour maps of optical depth, the cloud is elliptically shaped, with a ratio of major to minor axes of 7:5. Supposing the cloud to be an

oblate spheroid with a semi-major radius of 10 pc and semi-minor radius of 7.5 pc, and assuming a mass of $3.7 \times 10^6 M_\odot$, we find for a mean density:

$$\rho = 1.2 \times 10^3 M_\odot pc^{-3}$$
$$= 8.0 \times 10^{-20} g\ cm^{-3}$$

In terms of an atomic density, $n_H(total)$, for hydrogen in any form, we have

$$n_H(total) = 4.8 \times 10^4 cm^{-3} .$$

This analysis has assumed only that the gas molecules are in Keplerian orbits and has neglected turbulence. The virial theorem can be used to calculate the effect of turbulence on the mass estimate. We have

$$\frac{1}{2} m(v_g^2 + v_t^2) = \frac{1}{2} G \frac{mM}{R}$$

where v_g is the velocity in the gravitationally bound orbit and v_t is the mean turbulent velocity. Then

$$M = \frac{R}{G} (v_g^2 + v_t^2) .$$

At $R = 10$ pc, $v_g = 40$ km/s ; from the spectra at individual map points, the mean turbulent velocity is estimated to be about 20 km/s. If the cloud is stable against dissipation by turbulence, then the total mass estimate must be increased by about 25%.

Applying this correction for the effect of turbulent motions, the derived parameters of component I, assuming that the cloud is

gravitationally stable and is in rigid-body rotation, are summarized in Table 4-1. The coordinates of the centroid are those at velocity +45 km/s, which is the velocity of maximum optical depth. It is of interest to note that Sandqvist (1971) finds that the centroid occurs at about +48 km/s, in good agreement with Figure 4-1. The position he quotes is $l = -1.'8 \pm 0.'3$; $b = -4.'2 \pm 0.3$, which is one arcminute north in latitude from the position in Table 4-1.

A similar analysis can be carried out for component II. The measured velocity gradient is 7.5 km/s per arcminute, so if the cloud is assumed to be at a distance of 10 kpc and in rigid body rotation, the angular velocity is $0.8 \times 10^{-13} \text{sec}^{-1}$, corresponding to a rotational period of 2.5×10^{6} years. If the cloud is gravitationally stable, the required mass is $2 \times 10^{5} M_{\odot}$ provided the cloud has a radius of 5 pc. The size of the component II cloud is very uncertain, however. For velocities above 30 km/s, the two components are blended; below 30 km/s, component II lies near the edge of the optical depth map boundary. As a result, the size of the feature is difficult to estimate, although one has the impression that component II is smaller than component I. A value of 5 pc for the radius is probably a reasonable estimate. Under this assumption, the mass density of the cloud is about $400\ M_{\odot} \text{pc}^{-3}$ or $3 \times 10^{-20} \text{gm cm}^{-3}$, which corresponds to a number density of hydrogen atoms of $2 \times 10^{4} \text{cm}^{-3}$. The mass estimate is not very certain, because of the possible errors in the size estimate. Assuming the simple model of rigid-body rotation, the density is rather more certain, since it depends only on ω, and not on R. If the cloud is gravitationally bound and in simple rotation, the quantity ω^2/G is equal to the

Table 4-1

Derived Parameters for Component I of the "+40 km/s" Cloud

Cloud Dimensions (to half-maximum optical depth):	$7' \times 5'$ $= 20 \times 15$ pc at 10 kpc
Coordinates of Centroid:	$l = -1\overset{\circ}{.}8 \pm 0\overset{\circ}{.}3$; $b = -5\overset{\circ}{.}2 \pm 0\overset{\circ}{.}3$
Velocity Gradient:	11.3 km/s per arcmin ± 12%
Angular Velocity:	$1.3 \times 10^{-13} s^{-1}$ ± 12% at 10 kpc
Rotational Period:	1.6×10^{6} years ± 12%
Mass (within 10 pc radius):	$4.6 \times 10^{6} M_{\odot}$ ± 25%
Mass Density:	$1.5 \times 10^{3} M_{\odot} pc^{-3}$ ± 25% $= 1.0 \times 10^{-19}$ g cm^{-3}
Number Density of Hydrogen Atoms (in all forms):	$6.0 \times 10^{4} cm^{-3}$ ± 25%

density times a geometrical factor which is about 4 provided the cloud is roughly spherical. Given the observed velocity gradient, then, we conclude that component II will be gravitationally bound if the mean mass density exceeds 3×10^{-20} g cm^{-3}.

The derived parameters for the component I and II clouds are based upon the simplest of kinematic models, namely, rigid-body rotation. It is well to examine alternative explanations for the observed velocity gradient.

A simple uniform contraction or expansion is ruled out both because of the linear velocity dependence of the position coordinates, and because of the appearance of the cloud in the optical depth contour maps. If the motions of the gas were purely radial with respect to the

center of the cloud, then the peak optical depth should occur in a ring (for an isotropic distribution of velocities) or in some form of double structure (for motion perpendicular to a given axis, assuming the axis is not parallel to the line of sight.) The contour maps show instead a single elliptical feature above 35 km/s, whose size is independent of velocity. The observations do not support a pure expansion or contraction model for component I. The data for component II are less discriminating because of the cloud's proximity to the continuum edge. The linearity of points in the l-V plot favors the rotational model over one with radial motions, however. Moreover, the magnitude of the velocity gradient in either component requires that for an expansion model the age of the clouds is less than 10^6 years; for a contraction model the clouds must be experiencing a rapid collapse, such that in the absence of strong braking effects the objects will be highly condensed in less than 10^6 years. Although these possibilities suggest many intriguing theoretical ramifications, the observational evidence supports a rotational model best, with radial motions smaller by perhaps an order of magnitude.

The assumption that the objects are gravitationally bound might also be questioned. Instead of a rotational motion, an explanation for the velocity gradient could be a shearing motion, in which the molecular cloud is being stretched apart along the line of sight. Now we cannot observe the velocity structure of the gas in the transverse direction to the line of sight. It seems reasonable to suppose, however, that transverse motions within the galactic plane are comparable to the line-of-sight motions. The velocity dispersion across

component I is at least 40 km/s; if we assume a comparable transverse dispersion, the cloud will appear as a highly elongated object, more than doubling its present angular extent in longitude, in only 10^6 years. The fact that we observe it now as a fairly compact, low eccentricity object would be fortuitous. This argument is not conclusive, of course, but it suggests one of two alternatives: (1) The clouds are in fact gravitationally bound, or (2) the clouds were formed as compact, dense objects which have sufficient internal kinetic energy that they will expand and be dissipated on a time scale of a few million years, in which case the present appearance of the objects is simply due to chance.

In conclusion, the most plausible explanation for the large velocity gradient across the absorption components is still rotation about an axis nearly perpendicular to the galactic plane. The model used here of solid-body rotation is certainly over-simplified, in that we would at least expect the angular velocity ω and the density ρ to be functions of position. The excitation temperature, T_s, may be a function of density, and hence of position also. The available data are not adequate to distinguish between more sophisticated models of the gas velocity and density. In spite of this, the derived parameters presented in Table 4-1 describe physical conditions which are in agreement with most other observations of the region, taking into account the differences in angular and velocity resolution.

The positive systemic velocity of the +40 km/s cloud complex is an unsolved problem. The cloud is seen in absorption against the

nonthermal continuum source in Sgr A, which has generally been identified with the nucleus of the galaxy. The velocity of the cloud centroid estimated from Figure 4-1 is +45 km/s. Then this object must be falling in toward the center of the galaxy, in contrast to the bulk of neutral hydrogen in the vicinity of the galactic nucleus (some $4 \times 10^7 M_\odot$) which appears to be either expanding outward or in rapid circular motion about the center (Rougoor 1964; van der Kruit 1970). A possible explanation has been suggested by Oort (1968), who argues that the galactic nucleus underwent a series of explosive events which ended about 10^7 years ago. In these explosions large quantities of gas were expelled from the nuclear region, probably clearing out the gas from the central region to a radius of at least 1 kpc. The expelled matter has since fallen back toward the nucleus, carrying with it angular momentum picked up from the galaxy during its outward passage. The infalling gas then forms a disk in rapid rotation about the center. The +40 km/s cloud may be the remnant of such an explosion, ejected recently enough that it did not acquire sufficient angular momentum to hold it in the nuclear disk. At present the cloud is falling back toward the nucleus. In the absence of dissipative forces, the total kinetic energy of the cloud sets a lower limit on the energy released in the initial explosion. For a systemic velocity of 45 km/s and an assumed cloud mass of $5 \times 10^6 M_\odot$, the kinetic energy of the cloud is 10^{53} ergs.

Other Related Observations

As indicated at the beginning of this chapter, a number of other molecules have been observed in the velocity range and position of the +40 km/s cloud of Sgr A. We review this work here, as it relates to the present results.

The most extensive mapping of 1667 MHz OH absorption to date has been the work at Parkes by Robinson and McGee (1970). In the subsequent analysis by McGee (1970a) his cloud number 40 corresponds to the feature we have discussed above. McGee locates the center at $l = 0^{o}00'$, $b = -0^{o}06'$, with half-widths of $17' \times 16'$. The center velocity is +38 km/s, with a line width at half-maximum of 48 km/s. The maximum apparent opacity is 0.26, corresponding to an optical depth (defined by equation (3-4)) of $\tau = 0.3$. The difference between these results and those of this dissertation can be attributed entirely to the poorer resolution of the Parkes observations. The beamwidth of the 210-foot antenna at 18 cm is 12.'5; the size of the cloud is overestimated as a result, and since no correction was made for the filling factor of the cloud, the opacity is underestimated. As mentioned in Chapter 3, the present work finds an optical depth four times larger than McGee's result. The coordinates of the cloud center agree fairly well with those of Table 4-1, but one should note that there is no evidence for a velocity gradient in McGee's figure 1(e). The separation into two components is also lost. We see the crucial importance of adequate angular resolution in determining the velocity structure of the galactic center molecular clouds.

The lunar occultation observations by Kerr and Sandqvist (1968) in the 1667 MHz OH line discovered the velocity gradient in the 40 km/s object, which they interpreted as a rotation of the cloud, with the axis of rotation inclined at an angle of 60^{o} to the galactic plane. Subsequent observations (Kerr and Sandqvist 1970) in the λ6 cm H_2CO line confirmed this result. In a more extensive analysis Sandqvist (1971) determined that the position of maximum opacity was at $l = 1\overset{\prime}{.}8$, $b = -4\overset{\prime}{.}2$, and occurred at a velocity of +48 km/s. The size of the cloud at his limits of detectability was $6' \times 4'$ in l and b. The cloud has a high velocity gradient, which Sandqvist estimates at about 8 km/s per arcminute, in the same sense as galactic rotation.

The lunar occultation results agree rather well with the present work. The velocities of maximum absorption are the same within the uncertainties. The coordinates of the cloud centroid show a discrepancy of about one arcminute, which is probably not serious, in view of the size of the cloud and the difference in the methods by which the two positions were derived. The lunar occultation value of 8 km/s per arcminute for the velocity gradient was obtained from the limits of detectability for immersion and emerision, as a function of velocity. The quoted value, then, might easily differ from that derived here by 25%, so the agreement is reasonable. Sandqvist's cloud size is $6' \times 4'$, which is significantly smaller than this work's measured dimensions, $7' \times 5'$ at <u>half-maximum</u> optical depth. This difference is almost certainly due to a much higher noise level for the lunar occultations, where the integration time per spectrum is less

than 70 seconds. In sum, the lunar occultation studies, which have better angular resolution but poorer sensitivity than this work, find that the properties of the +40 km/s cloud in Sgr A are essentially the same as we have deduced from our synthesis observations.

Probably the most thoroughly studied molecule in the galactic center to date has been formaldehyde. Because the 1_{11}-1_{10} transition occurs at the relatively high frequency of 4830 MHz, this line allows improved angular resolution over the 1667 MHz OH line. The sources Sgr A and B2 were mapped in the H_2CO line by Scoville, et al. (1972) with a 6.'6 antenna beam. Their cloud 5 corresponds to the object we have been discussing. However, the position and velocity gradient which they calculate are significantly different from those found here. Because the antenna beam was comparable to the cloud size, the velocity gradient they derive is a factor of 6 too small. The center of the cloud is also in error, for the same reason. A more satisfactory single-dish mapping was done by Gardner and Whiteoak (1972), with a 4.'2 beamwidth. They conclude that the absorption is due to a single feature for velocities above 30 km/s, but that additional features are present at lower velocities. Their positions of peak H_2CO absorption agree reasonably well with the present work for velocities greater than 30 km/s. Below that range, the position they measure lies between the centers of OH components I and II, indicating that they have not resolved the two clouds. The velocity dispersion is estimated to be 8 or 9 km/s per arcminute, in reasonable agreement with the present results.

The interferometric mapping of Sgr A in the H_2CO line by Fomalont and Weliachew (1973) also is in good qualitative agreement with these aperture synthesis results, although a detailed comparison is difficult because the H_2CO map covers a much smaller area of the sky, but with higher angular resolution. Their size estimate for the cloud is $5' \times 2'.5$, which is comparable to their map area. Thus, their mass estimate, based on an analysis similar to ours, is a lower limit. They obtain a value of $3 \times 10^5 M_\odot$, assuming the quoted dimensions. Their estimated density of hydrogen molecules is $\sim 10^5 cm^{-3}$, somewhat larger than the value in Table 4-1. On the whole, however, there is good agreement between the present work and the H_2CO maps of Fomalont and Weliachew.

Solomon, et al. (1972) have done mapping of the Sgr A region at positive velocities in the J = 1-0 emission lines of CO at λ2.6 mm, with a spatial resolution of 1'. They find two optically thick clouds centered at velocities around +55 and +20 km/s. The locations of these two features agree with the positions of components I and II listed in Table 4-1. Their higher-velocity component has a peak brightness temperature of 16 K, and the lower-velocity component peaks at 13 K. The velocity +55 km/s is not in very good agreement with our OH value of +45 km/s for component I. The ^{12}CO lines are heavily saturated, however. We note that for the optically thin ^{13}CO line, the spectrum in their Figure 4a peaks at 44 ± 1 km/s. Since observed ^{13}CO emission arises in a much larger volume of the cloud, the excellent agreement of this velocity with the OH value apparently confirms that our component I and the higher velocity feature of the CO

emission represent the same physical object.

The observations by Cheung, et al. (1968) of NH_3 emission at $\lambda 1.25$ cm in Sgr A locate the center of emission at a position $3' \pm 2'$ south in declination from the continuum peak of Sgr A, and with a mean velocity of +23 km/s. The size of the NH_3 source is less than 5' in overall extent. The position and velocity both agree with the values for component II. Thus, it appears that the NH_3 emission is from the component II cloud, but not (or at least to a much smaller extent) from component I. This implies that there is a significant difference in either the abundance or the excitation of NH_3 between the two clouds.

We have considered the implications of the observed velocity structure of Sgr A in the positive-velocity range. The simplest interpretation consistent with the data is that the molecular absorption occurs in two clouds, separated by at least 20 km/s in observed radial velocity. Both clouds are undergoing rotation, which to first order can be treated as that of a solid body. The velocity widths of the absorption spectra show that the gas must have large turbulent internal motions, with mean velocities of about 20 km/s, in addition to the gradient with position. We estimate that the rotational velocity in the outer parts of the cloud exceeds the turbulent motion by a factor of two.

The derived densities and masses for components I and II are consistent with the observations of other molecules. Solomon, et al.

(1972) find a firm lower limit of $10^5 M_\odot$ for each of the clouds, and it seems likely, considering their assumptions, that the true value could certainly be a factor of 10 higher, in agreement with our dynamical calculation. The observation of NH_3 in emission requires a density of molecular hydrogen of $n_{H_2} > 10^3 cm^{-3}$ to explain the observed intensity of the line. The existence of other molecules, including OH, in the clouds requires a high density of shielding material, either dust or H_2, to prevent dissociation by UV photons.

The large-scale motions of the gas near the galactic nucleus should lead to local density enhancements within turbulent cells. For a homogeneous uniformly-rotating sphere, the density at which the cloud is gravitationally unstable towards collapse is

$$\rho > \frac{3\omega^2}{4\pi G} .$$

The rotation of the cloud will tend to hinder the collapse of the initial condensations. If, as is likely, the gas is in differential rotation about the galactic nucleus, it can be shown (Goldreich and Lynden-Bell 1965) that the density limit for collapse is increased by a term proportional to the rate of velocity shear, $(d\omega/dR)$.

A possible interpretation of the two components, then, is that they have formed from density enhancements within the turbulent, rapidly rotating nuclear gas, and are in motion relative to each other due to the effects of differential rotation about the nucleus. The clouds themselves are in rapid rotation following the initial collapse, since each region of enhanced density undoubtedly had considerable angular momentum initially, in the form of a turbulent eddy. This

rotation will tend to slow further collapse. The large observed turbulent velocities within the two clouds suggest that the process of fragmentation and collapse will proceed on a diminishing scale of size, leading ultimately to star formation.

Although somewhat speculative, this picture is highly plausible on two grounds: specifically, it is in good agreement with the observational data; and, more generally, it is a reasonable extension of our knowledge concerning the behavior of large gas clouds undergoing rotational and turbulent motion.

Sgr A--Negative-Velocity Absorption Features

Comparison of the single-dish spectrum (Figure 3-3) with the map-point spectra shows how the deep absorption line at around -135 km/s is produced by OH clouds lying well south in latitude of the Sgr A peak. The contours of optical depth increase monotonically toward the southern-latitude edge of the continuum, and for the most part do not reach a local maximum within the maps. For this reason, it is impossible to determine the center of the absorbing clouds, their dimensions, or maximum optical depths. The strong absorption in the single-dish spectrum at -135 km/s is hardly visible in the high-angular resolution spectra near the continuum peak (Figure 3-4, numbers 1 through 5) but becomes prominent in the spectra which lie at galactic latitude $b = -7'$ (numbers 6, 7, and 8). The negative-velocity range of the absorption is very large--we see that in spectrum 7 of Figure 3-4, the brightness temperature does not come completely back up to the continuum level even at -200 km/s. This observation is corroborated by the single-dish spectrum, which is not clear of absorption for any

velocity between +100 km/s and -230 km/s. At -80 km/s, the single-dish spectrum shows an absorption equal to 6% of the continuum level; it is not surprising, then, to find weak absorption ($\tau \simeq 0.05$) in the optical depth contour maps at all negative velocities.

The strongest absorption is concentrated along the southern-most edge (in latitude) of the continuum, and avoids the continuum peak, as the optical depth maps clearly show. This agrees with McGee's results (McGee 1970a) which show two separate clouds (numbered 6 and 7 in his Table 1) with radial velocities of -136 and -137 km/s, and centered at ($l = -10'$, $b = -13'$) and ($l = +11'$, $b = -16'$) respectively. The linewidths are large--47 and 34 km/s for the two clouds. The center position of cloud 6 lies about five minutes of arc from the negative-longitude tip of the continuum map, while the center of cloud 7 is some fifteen minutes from the edge of the contour maps. Examination of the optical depth maps in the range from -92 to -151 km/s shows that in fact the OH absorption definitely appears to split into two components, the stronger of which corresponds to McGee's cloud 6, whose center lies closer to our maps than does cloud 7. The maximum absorption is found at a velocity of -137 km/s. So far as they can be compared, then, McGee's results and those of this work are in good agreement. It is also worth noting that Sandqvist (1971), in his lunar occultation study, states that the -130 km/s absorption is much larger in angular extent than the +40 km/s cloud, that it has a higher opacity, and that its centroid position is at least 10 arc-minutes south of the +40 km/s cloud in galactic latitude. Since the

+40 cloud is at about b = -5', the -130 km/s absorption is centered at b = -15', in agreement with McGee's findings.

The positions of the absorption centers and the peak optical depths of these clouds cannot be located with the synthesized maps. We can only put limits on them. The latitude of maximum absorption is south of b = -9'. The longitudes of the two features are very uncertain; McGee's values of -10' and +11' are evidently consistent with these maps, but nothing more can be said with any confidence. The peak optical depth is greater than 0.9 for the negative-longitude cloud and greater than 0.4 for the positive-longitude feature. The latter value is not a very strong limit, since the cloud center is evidently far from the continuum edge. We note that McGee's apparent peak opacity for the two clouds are 0.23 and 0.35, respectively, illustrating again the effect of insufficient angular resolution in underestimating the opacity. These lower limits tend to support Sandqvist's assertion that the negative-velocity clouds have higher opacities than the +40 km/s cloud.

There is some indication in the optical depth contours that the negative-velocity clouds may have condensations on an angular scale of a few minutes of arc. The map for -92.31 km/s gives the impression of an elliptical feature with a width of 5'. The proximity to the edge of the map makes such an interpretation uncertain, however. The maps at -115.33, -136.90, and -151.29 km/s also show what appears to be a local peak with a small angular size. One must also beware of edge effects here. The narrowness of the absorption peak suggests that the closing of the contour lines around it may be due partly to

noise. In spite of these problems, one has the impression that there are small-scale condensations in the clouds, lying close to the edge of the map. Such an interpretation is consistent with the situation for Sgr B2, where we found a large number of discrete clouds with angular sizes typically of five to ten arcminutes.

Kinematic Models

The interpretation of these observations in terms of a unified theory of gas motions near the galactic center is far from clear. The model proposed by Rougoor (1964) and extended by van der Kruit (1970) includes the well-known "rapidly-rotating nuclear disk", which is seen as feature IV of van der Kruit's Figure 2. However, the HI observations are confused by absorption in the vicinity of the Sgr A source, so that the interpolation of the disk locus in the l-V plane is uncertain for the region near $l = 0^{o}$. Rougoor interpreted the HI emission observations in terms of a disk of gas whose motion was almost entirely rotational, with only a small radial component. Since that time, the discovery of the various molecular absorption lines has necessitated a kinematic model for the gas which includes a large radial velocity component. Such models have been proposed by Scoville (1972) and by Kaifu, Kato, and Iguchi (1972). Scoville suggests two possible models, one to fit the negative-velocity features and one for the positive-velocity absorption of formaldehyde. Both models are simply rings centered on ($l = 0^{o}$, $b = 0^{o}$); for the negative-velocity features the ring radius is 218 pc, with a rotational velocity of 50 km/s and a radial velocity of 145 km/s. Scoville favors the interpretation that the ring is

expanding, but he does not rule out a contracting ring. Kaifu, et al. use the l-V maps of OH opacity from McGee (1970a) to derive a ring 270 ± 30 pc in radius, with a rotation velocity of 50 ± 20 km/s and an expansion velocity of 130 ± 5 km/s. In addition, they postulate an inner, contracting ring, based on the velocity-longitude distribution of "dense" molecular clouds and of HII region recombination line velocities. The inner ring has a radius of 140 pc with a rotational velocity of 60 km/s (in the same sense as the outer ring, and of galactic rotation) and a contraction velocity of 40 km/s. (It is interesting to note that the neutral hydrogen feature V of van der Kruit (1970) agrees in longitude and velocity with the negative velocity model of Scoville, and with the outer ring of Kaifu, et al.)

The kinematic picture of a ring of gas in both radial and rotational motion will explain many of the OH absorption features in our maps of the Sgr A and Sgr B2 regions. It should be emphasized that the range of galactic latitude covered by these maps is too small to distinguish between the specific velocity models. Some general conclusions can be made, however. First, the negative-velocity clouds almost certainly lie between us and the galactic nucleus. This point was not clear from previous low-angular resolution studies. The negative-velocity absorption could have been due to gas beyond the nucleus. However, the high optical depths found in this work argue against any significant extended continuum emission arising in front of the clouds. There is also evidence in the spectra of Figure 3-4 for a weak absorption feature near -135 km/s on the Sgr A continuum peak. This evidence

suggests that the negative-velocity OH cloud is in front of the nucleus and thus is expanding away from it, although the main cloud concentration is south in latitude from Sgr A. Secondly, the -135 km/s cloud is probably located well away from the galactic nucleus. A value of around 250 pc is not inconsistent with the observations. The outer ring must be somewhat below the equatorial plane of the galaxy, an asymmetry not explained by the kinematical models.

The relationship between the +40 km/s cloud and the negative-velocity absorption is still unclear. From the near-coincidence of the Sgr A peak with the maximum absorption in the cloud, it is likely that the two objects are close together in space. The inner contracting ring of Kaifu, et al. (1972) fits the observed velocity and longitude of the +40 km/s cloud quite well, but this is hardly surprising since the +40 cloud values were part of the data from which the ring is derived. Moreover, component II of the Sgr A + 40 km/s feature (the lower-velocity component) is not explained by the inner ring, unless we also postulate large random motions within the velocity field of the ring. Indeed, the simplicity of the velocity models of Scoville and of Kaifu, et al. are a result of the simplification of the input data which they use. Our higher angular resolution observations (and, in fact, even the maps of McGee (1970a) and Scoville, et al. (1972)) show that chaotic or turbulent motions seem to be nearly as important as any large-scale systematic velocity fields. The evidence in favor of the inner contracting ring is therefore not very compelling.

One of the important problems relating to the proposed expanding rings of gas clouds is the matter of their origin. There has been considerable speculation on possible explosive events in the galactic nucleus, which somehow expelled the gas clouds from the center. Subsequent interaction with the inner regions of the galaxy resulted in the transfer of angular momentum to the gas, resulting in the observed velocity distributions (Oort 1968,1971; van der Kruit 1970,1971; Sanders, et al. 1972). There are many questions raised by this hypothesis. In common with the problem of the QSO's is the matter of energy sources and the mechanism by which matter (in this case not only electrons but, evidently, neutral atoms, molecules, and possibly even dust) is accelerated out of the nuclear region. Second, the time-scale of the events is a problem. Oort (1971) and van der Kruit (1971) claim that such events have recurred as recently as $\sim 5 \times 10^6$ years ago. This is shorter than the time for one revolution of Rougoor's "nuclear disk" ($\sim 10^7$ years). The gas of the disk should have been severely disrupted by such explosive occurrences, and would not have had time to settle down into circular motion since the last disturbance. Thus, the claim that the "nuclear disk" is in simple rotation seems inconsistent with the explosion hypothesis. Van der Kruit (1971) has argued that the explosion may have shot material out at a large angle to the galactic plane, so that the inner regions are not greatly disrupted. (On the other hand, we have already remarked on the apparently chaotic nature of the gas motions when looked at in detail.) If the explosive events occurred at intervals of 5×10^6 years over a significant fraction of the age of the galaxy, then the mass loss from the nuclear region

also becomes a severe problem (Sanders, et al. 1972).

An alternative explanation for the observed longitude-velocity dependence of the gas motions has been suggested by Simonson and Mader (1973) and by Scoville (1973, in preparation). They investigate the observed velocity field of two-arm spiral models for the inner galaxy. Detailed calculations by Simonson and Mader show that the observed HI distribution can be well-described by a disk in differential rotation. The motions in the central part can be explained by superposing on the rotating disk an elliptical dispersion ring which is the natural consequence of a two-armed spiral density wave. The model by Scoville has a two-armed spiral of constant inclination, undergoing differential rotation and an expansion which varies linearly with radial distance. His computed l-V curve shows fair agreement with the observed distribution of molecular absorption. The advantage of these alternative explanations for the observed gas motions is that they postulate reasonable extensions of the spiral structure of the Galaxy. One is not forced to invoke explosive events of uncertain origin to explain the gas motions, nor are the disruptive results of such explosions a difficulty. It will be interesting to see if the spiral-arm density wave concept can be fitted to a more detailed picture of the gas motions as higher resolution surveys over a wide range in galactic longitude (such as the λ2.6 mm CO emission studies of Scoville, Solomon, and Jefferts (1973, in preparation) are completed.

Sgr B2--Kinematics

In this section we will interpret the observed distributions of Sgr B2 OH absorption clouds in terms of their motions and locations relative to each other and to the sources of continuum emission. The evidence which the observations provide to support or disprove the models of gas motions near the nucleus, as discussed above, will also be examined.

The Sgr B2 region includes the dominant components G0.5-0.0 and G0.7-0.0, both of which are HII regions believed to lie close to the galactic center. The sources have flat spectra (Downes and Maxwell 1966) and produce detectable hydrogen recombination line emission. Observations of the H109α line (Reifenstein, et al. 1970) have shown that the velocity of peak emission and the observed width of the line for the two sources are:

$$V = 47.2 \text{ km/s} \quad ; \quad \Delta V_{1/2} = 36 \pm 1.1 \text{ km/s} \quad \text{(G0.5-0.0)}$$

$$V = 61.6 \text{ km/s} \quad ; \quad \Delta V_{1/2} = 48 \pm 1.4 \text{ km/s} \quad \text{(G0.7-0.0)}$$

They also note that for G0.7-0.0 the width and shape of the line suggest that it might be a superposition of two or more separate components at different velocities. The mass of ionized hydrogen is calculated to be $9.1 \times 10^3 M_\odot$ for G0.5-0.0 and $5.9 \times 10^3 M_\odot$ for G0.7-0.0. An estimate of the turbulent-velocity half-widths results in values of 20.8 ± 1.7 km/s and 32.4 ± 1.6 km/s for G0.5-0.0 and G0.7-0.0, respectively.

These results for the ionized gas should be compared with the velocities and linewidths for the molecular clouds catalogued in the previous chapter (Table 3-9). The deepest absorption features occur at or near a velocity of +62 km/s, and are confined entirely to the neighborhood of the G0.7-0.0 source. There is no evidence for significant absorption at +62 km/s in the map-point spectra of G0.5-0.0. The best agreement in peak velocity and linewidth of the H109α line is for cloud 1, which lies nearest the peak of the HII region. It should be noted that the survey by Reifenstein, et al. (1970) had a primary beamwidth of about 6', so that pointed at the peak of G0.7-0.0 their antenna would have a significantly lower gain at the positions of our clouds 2, 3, and 4. We also recall their remark on the possibility of multiple components to explain the width and shape of the recombination line. The good agreement between the hydrogen recombination and OH absorption line velocities, and the remarkably close spatial grouping about the G0.7-0.0 continuum peak of the four clouds near +60 km/s, are convincing evidence that the molecular clouds at this velocity are intimately connected with the G0.7-0.0 HII region and are situated in close proximity to it. There is some difference in the velocity and velocity dispersions of the four clouds; cloud 1 has the narrowest linewidth and seems to have a systemic radial velocity about 7 km/s larger than the other three clouds. The velocity difference between the clouds is such that if cloud 1 is assumed to have the same velocity as the HII region, then clouds 2, 3, and 4 are moving away from the HII region with a velocity of 7 km/s projected onto the line of sight. Because the absorption lines for clouds 2, 3, and 4 have large velocity widths, the

velocity relative to cloud 1 is uncertain by as much as 50%.

The four clouds show little or no change in position with velocity, unlike the +40 km/s cloud of Sgr A, indicating that rotational motion is not significant. Since G0.7-0.0 is an HII region, one would expect to find gas in expansion around it, and indeed, the peaks of OH optical depth lie more or less in a ring around the continuum peak. The measured optical depth is proportional to the column density of OH molecules and inversely proportional to the excitation temperature of the line. (Thus, the relatively lower optical depths near the continuum maximum could be due to an increase in the excitation temperature of the OH near the center, rather than to a lower column density of molecules.) However, if we assume that the excitation temperature is essentially constant throughout the clouds, then the optical depth maps (Figure 3-12) suggest that the molecular clouds are condensations within an expanding shell of gas, moving away from the central HII region with a velocity on the order of 7 ± 3 km/s, and with rms turbulent velocities of about 25 km/s. We also recall that the two maser emission sources were found to lie about one arcminute from the continuum maximum, with velocities of 69 and 56 km/s. If the H109α line indicates a radial velocity of 62 km/s for the ionized gas, then the OH maser sources have velocities of +7 and -6 km/s with respect to the HII region. These velocities suggest that the maser emission may be produced within the expanding shell. The stronger line, at 69 km/s, lies on the far side of the HII region, while the weaker line at 56 km/s is on the near side.

The apparent expansion of the gas could be explained simply by random velocity dispersion of the dense molecular condensations. In that case the velocity of cloud 1, which does not appear to be moving relative to the HII region, is not surprising. On the other hand, the expansion of ionized gas into the surrounding neutral matter is a well-known phenomenon associated with HII regions. For example, detailed optical studies of the Orion Nebula (Wilson, et al. 1959) have shown that the ionized gas is expanding with a velocity of about 10 km/s, which is approximately the isothermal sound speed for the hot gas. Recently, Zuckerman (1973) has proposed a model for the Orion Nebula in which the HII region is expanding away from the dense molecular cloud, thus accounting for the systematic difference in velocities of the hydrogen recombination lines and the molecular line. The postulated expansion velocity of 7 km/s for the molecular clouds surrounding G0.7-0.0 is comparable to the sound speed for the HII region, for which Reifenstein, et al. (1970) calculate an electron temperature of 6900 ± 1200 K. Since the ionized gas will expand behind a shock front propagating at approximately the sound speed (Spitzer 1968), we investigate the possibility that the observed molecular cloud velocities could be explained by an interaction of the cold, dense clouds with the hot expanding gas of the HII region.

To estimate whether such a mechanism is feasible, we ask if the gas pressure of the HII region exceeds the pressure in the molecular clouds. If the expanding HII region is to affect the clouds, this criterion must be satisfied. The pressure of a gas is given by

$$P = \frac{\rho k T}{\mu} \tag{4.1}$$

where ρ is the mass density, T is the temperature, and μ is the mean mass per particle. We denote the quantities referring to the molecular clouds by subscript I and to the HII region by II. If the molecular cloud consists entirely of H_2, we have $\mu_I = 4\mu_{II}$. The electron density for G0.7-0.0 is 190 cm^{-3} and the temperature is 6900K (Reifenstein, et al. 1970). If the gas is fully ionized, we have $\rho_{II} = 3 \times 10^{-22} g\ cm^{-3}$. Based on the CO emission observations of Scoville, et al. (1973), we assume $T_I = 20K$. Then the ratio of pressures is

$$\frac{P_{II}}{P_I} = \frac{\rho_{II} T_{II} \mu_I}{\rho_I T_I \mu_{II}} \tag{4.2}$$

$$= \frac{4 \times 10^{-19} g\ cm^{-3}}{\rho_I} \tag{4.2}$$

The gas pressure of the HII region will exceed that of the cold cloud if the particle density of molecular hydrogen is less than $10^5 cm^{-3}$, corresponding to a mass density of 5000 $M_\odot pc^{-3}$. It is unlikely that the average cloud density is this high, although there may be small condensations approaching this value. But for the clouds as a whole, it is probable that the quantity P_{II}/P_I is at least as large as 10. If, as we have argued, the molecular condensations lie very close to the HII region, it is plausible that a pressure difference of this magnitude would produce significant dynamical effects on the cold, dense clouds.

This argument suggests that expanding motions are possible, as long as the molecular cloud densities are not too large. A detailed calculation, however, should include the effects of the expanding shock front when it encounters the dense neutral regions. The fragmentation of the absorbing region into the four distinct clouds of Figure 3-13 can readily be explained by this picture of an expanding hot gas encountering a cold cloud. Since the pressure gradient produces an outward acceleration of the cold cloud, the cloud will develop a Rayleigh-Taylor instability which separates regions of enhanced density, allowing the hot gas to "bubble" around the condensations. (The situation is similar to that seen in the well-known optical photographs of the HII region M16.)

The large widths of the OH absorption lines make the systemic velocities of the four clouds somewhat uncertain. It is clear, both from the spectra of Figure 3-9 and the optical depth maps in Figure 3-12, that the velocity of greatest absorption is about +55 km/s for clouds 2, 3, and 4. The model of expanding hot gas against the cold clouds could account for the difference of 7 ± 3 km/s between this value and the H109α velocity. Cloud 1 is evidently not moving away from the HII region, since it has the same radial velocity within the errors of measurement. We could explain the cloud 1 velocity by assuming either that it has not yet encountered the hot gas of the HII region, or that its density and temperature are sufficient to keep the cloud in pressure equilibrium with the hot gas. If the Rayleigh-Taylor instability is operative, it is possible that cloud 1 was sufficiently

massive to "fall through" the expanding gas very early on, so that it has not acquired much outward motion.

Our calculation of the pressure difference between the ionized gas and the cold molecular clouds suggests that the latter may be expanding away from the HII region. The observed fragmentation of the clouds has a natural explanation in this picture. A detailed model cannot be constructed with any accuracy, given the existing data, however. One would like to have at least a factor of two or three improvement in resolution to get a better understanding of the structure of the HII region and the cloud sizes. The large turbulent linewidths within the cloud also complicate the kinematical picture. In any case, the results of this study show that the dense molecular clouds at about +60 km/s are closely associated with the HII region G0.7-0.0; the cloud is fragmented into at least four components, with optical depths ranging from 0.6 to greater than 3, and with typical sizes of about 5', or 15 pc at the galactic center. We have suggested that the cold gas may be undergoing an expansion away from the HII region because of pressure from the ionized gas.

We consider next the absorption of G0.5-0.0 by cloud 5 of Figure 3-13. The recombination line velocity of the continuum source, as noted above, is 47.2 ±1.2 km/s. There is no significant absorption over the source at that velocity, becoming important only at about +25 km/s. It seems likely, then, that cloud 5 is not closely associated with the HII region, but lies some distance in front of it, as part of a larger association of discrete OH clouds. These clouds are

present in the optical depth maps between about +25 km and -20 km/s, and include numbers 5, 6, 7, and 8. Cloud 5 appears to be actually a group of condensations, not well-separated in space. At +5.50 km/s the feature is broken into two weakly resolved parts, which we have called 5 and 5A. Cloud 8 may also be a part of this complex. The change in the position of maximum absorption with velocity is most probably due to a velocity dispersion in the components, implying large turbulent motions in this particular association of molecular clouds. The appearance of clouds 6 and 7 in this same velocity range indicates that they are also probably part of the same kinematical feature.

The strongest absorption of cloud 5 occurs in the velocity range between +5 and +20 km/s. None of the existing models for gas motions near the galactic center would predict absorption in this velocity range. A successful kinematical model will have to include the "intermediate velocity" clouds 5, 6, 7, and 8. The existence of these features, which are not shown in the low-resolution OH survey of McGee (1970a), demonstrates that the molecular clouds cannot be explained by one or two rings in expansion and rotation. There exists a substantial amount of gas which does not fit the simple models proposed by Kaifu, et al. (1972) or by Scoville (1972). The two-armed spiral with expansion may be more fruitful in explaining the observations, although at the moment, the limited range of galactic longitude covered by this work does not allow a proper fit to the models.

We note, in this regard, that clouds 9 and 10, centered at velocities of -36 and -75 km/s, lie at the extreme positive longitude

end of the Sgr B2 map. Their presence may mean that there are additional concentrations of gas at these velocities, close to $l = +1.'0$. The features correspond to McGee's clouds numbered 18 and 10, at -31 and -83 km/s (McGee 1970a).

The single-dish spectrum of Sgr B2 (Figure 3-7), like that of Sgr A, has a large negative-velocity absorption feature. The maximum opacity is at -90 km/s with a width at half-intensity of 50 km/s. The shape of the line is remarkably smooth and symmetrical, with no hint of multiple components in the absorbing medium. It is surprising to find, then, that the optical depth maps show at least five discrete OH condensations in front of the continuum sources. Designated as cloud numbers 11 through 15, they are most prominent in the maps at velocities of -95.19 and -108.13 km/s, although cloud 11 is visible even at -73.61 km/s (Figure 3-12). The cloud sizes are small, typically 5' across; the maximum optical depths are on the order of unity, except for cloud 15 which is weaker ($\tau_{max} = 0.25$).

Comparison of these features with the low-resolution OH maps of McGee (1970a) shows a poor correlation with his "clouds". The discrete features of the present study are apparently disguised by the nearby strong continuum peaks of G0.7-0.0 and G0.5-0.0 when observed with low angular resolution, again showing the importance of having resolution comparable to or smaller than the size of the continuum sources.

The five clouds near -100 km/s appear to be local condensations within one large-scale kinematic structure. The velocity and longitude

range in which they are found corresponds fairly well to the neutral hydrogen emission feature "V" in van der Kruit's analysis (van der Kruit 1970; see his Figure 2). The velocity width of the HI emission is considerably narrower than the OH lines, and van der Kruit estimates that the mean latitude of the feature is -1^{o}, placing it well south of the region we observe. Therefore, it is difficult to argue that the OH clouds are associated with this HI feature. There is no other hydrogen emission that can be identified with these OH condensations.

In our discussion of the Sgr A kinematics, we considered the models proposed by Scoville (1972) and by Kaifu, et al. (1972). Both models predict radial velocities near -100 km/s for observations in the longitude range $l = 0^{o}.5$ to $0^{o}.7$, and so are in agreement with the Sgr B2 observations, as was the case for Sgr A. The difficulty with these models, as we said earlier, is their failure to predict the observed absorption at other velocities. One can add more rings, as Kaifu, et al. have done to explain some of the positive-velocity features. With our improved resolution, the situation becomes more complicated and no longer fits the model. Our results here show that a comprehensive explanation of the gas motions will also have to include large turbulent velocities within individual clouds. It is clear that the gas is highly fragmented into distinct condensations, which complicates the interpretation of the observed molecular distributions. A kinematical picture based on spiral structure, as discussed above but incorporating turbulent motions, may offer a simpler explanation than concentric expanding and contracting rings.

Chapter 5

PHYSICAL CONDITIONS IN THE MOLECULAR CLOUDS

Cloud Dimensions and OH Column Densities

We are interested in calculating the density of OH molecules in the fifteen clouds found in Sgr B2, and the two components in the "+40 km/s" feature of Sgr A. The calculation requires knowledge of the cloud dimensions, the column density of the molecules integrated along the line of sight, and the excitation temperature of the molecular transition. The clouds we have detected are, in general, found to be somewhat larger than the synthesized beam. Since the true optical depth can only be measured if the cloud fills the (synthetic) telescope beam, it is important to consider the possibility of unresolved clouds. In the case of Sgr A, we have already argued earlier that the observed cloud sizes show that they are resolved. For Sgr B2, the deep absorption lines near +60 km/s must also be due to clouds which fill the beam. If the fraction of the synthesized beam covered by the cloud were small, the observed opacities could not approach unity. For clouds 2 and 6, the maximum optical depths exceed 3.0, corresponding to an opacity of 95%. Even if the absorbing cloud were completely opaque, the observed opacity requires that the cloud cover 95% of one beam area. For an observed optical depth of 1, the area of such an opaque cloud could only be as small as 0.63 of the beam area, corresponding to a linear dimension of 0.80 of the beamwidth. The resolution of the maps, then, probably does not overestimate the true cloud sizes by more than about 20%. For regions of high opacity, the error will be even smaller.

In the following analysis we will neglect the correction for convolution by the synthesized beam. Our results for mean molecular densities may then be somewhat underestimated in some cases.

The column density, N_{OH}, of OH molecules and the excitation temperature of the 1667 MHz transition are related to the optical depth by the equation

$$\frac{N_{OH}}{T_s} = \frac{8\pi k \nu_o}{hc^2 A_{22}} \frac{\Sigma\, g_i}{g_u} \int_0^\infty \tau(\nu)\, d\nu \qquad (5.1)$$

where the optical depth, $\tau(\nu)$, is integrated over the line. Here ν_o is the frequency of the transition, 1667.358 MHz; A_{22} is the Einstein coefficient for spontaneous emission, which has the value 7.712×10^{-11} s^{-1} (Turner 1966). The statistical weight of the upper (F = 2+) hyperfine state is represented by $g_u = 2F+1$, and Σg_i is the sum of the weights. The other symbols have their usual meaning. Then the factor in front of the integral has the value $4.038 \times 10^{10} cm^{-2} K^{-1}$ if $d\nu$ is in Hertz.

The excitation temperature, T_s, is defined by the usual Boltzmann relation for the upper and lower levels. If g_u and g_l are the statistical weights of the upper and lower levels, we have

$$\frac{n_u}{n_l} = \frac{g_u}{g_l} e^{(-h\nu_o/kT_s)}$$

for the ratio of the populations of the two states. It has long been known (e.g., Goss 1968; Turner and Heiles 1971) that the four hyperfine lines of the OH ground state are often not characterized by a single

value of T_s . The most spectacular of these departures from LTE are manifested in the OH maser lines, for which the excitation temperature is negative. We will consider the problem of relating the line excitation temperature to the physical parameters of kinetic temperature and particle density, in the section following this one.

Using data for components I and II of the Sgr A +40 km/s feature and the fifteen clouds found in the maps of Sgr B2, we can compute the quantity (N_{OH}/T_s) from equation (5.1). The assumption is made that the velocity-dependence of the optical depth is gaussian, with widths as determined from the spectra at the positions of peak opacity and tabulated in Table 3-8. The velocity dispersion, σ_v , of the clouds is then

$$\sigma_v = \frac{\Delta V_{1/2}}{2 \cdot (\ell n\ 2)^{1/2}}$$

where $\Delta V_{1/2}$ is the full-width at half-maximum opacity. The linear diameters of the clouds can be estimated directly from the observed angular sizes, under the assumption that all the clouds are close to the galactic center, at a distance of 10 kpc. The observed sizes are probably fairly close to the true cloud dimensions, for the reasons discussed above. If we also assume that the line-of-sight dimensions of the clouds are similar to the observed transverse dimensions, then we can estimate the mean space density of OH molecules, n_{OH} , weighted by the excitation temperature:

$$\frac{n_{OH}}{T_s} = \left(\frac{N_{OH}}{T_s}\right) \cdot \frac{1}{L}$$

where L is taken to be equal to the mean linear diameter.

The results of these calculations for Sgr A, components I and II, and for the fifteen clouds of Sgr B2 are summarized in Table 5-1. The linear diameter is computed for the half-maximum optical depth contour; if the cloud shape is elliptical, the mean diameter is used. The quoted errors on (N_{OH}/T_s) are estimated from the uncertainties in $\Delta V_{1/2}$ (Table 3-8) and in the peak optical depths of the cloud centers (Table 3-11). It is difficult to estimate uncertainties on the space densities, (n_{OH}/T_s) , because of the assumptions on cloud thickness. The linear diameters quoted here are almost certainly not too small--they may in fact be slightly too large. In that case, the values for (n_{OH}/T_s) represent lower limits to the density. Note also that clouds 9 and 10 lie so close to the edge of the continuum that the diameter cannot be measured with any certainty.

Table 5-1 shows that the Sgr B2 clouds are divided into two distinct groups, depending on the value of their velocity dispersions. For positive-velocity clouds (1 through 7), the mean dispersion is 23.1 ± 4.0 km/s, while for the negative-velocity clouds (9 through 15), the mean dispersion is 12.9 ± 1.6 km/s. (Cloud 8 has been excluded because of its low optical depth.) We also see that the positive-velocity optical depths tend to be larger than those of the negative-velocity clouds, although there is a large intrinsic spread, especially for positive velocities. In the discussion of the Sgr B2 kinematics we distinguished two major velocity features: that near +60 km/s, consisting of clouds 1 through 4; and that near -100 km/s,

which includes clouds 11 through 15. It would be of interest, then, to characterize each of these two kinematic features by typical parameters of the individual molecular condensations found within them. We average the quantities of Table 5-1 for clouds 1 through 4 and for clouds 11 through 14. (Cloud 15 is very weak and is not included in the average.) The results are summarized in Table 5-2.

Table 5-1

Derived Properties of OH Absorption Clouds--Sgr A and Sgr B2

Cloud No.	V_o (km/s)	σ_V (km/s)	τ_{max}	N_{OH}/T_s (10^{15} cm^{-2}K^{-1})	Linear Diam. (pc)	n_{OH}/T_s (10^{-4} cm^{-3}K^{-1})
Sgr A-1	+45	23	1.2	11.0 ± 1.7	17	2.1
II	+25	18	0.8	6 ± 3	12	1.5
Sgr B2-1	+62	15	2.2	13 ± 2	16	2.7
2	+55	24	>3	>29 ± 9	12	>7.8
3	+55	27	1.5	16 ± 5	16	3.3
4	+55	24	0.6	5.7 ± 1.1	15	1.2
5	+15	21	0.8	6.7 ± 1.7	23	0.9
6	+25	27	>3	>32 ± 10	15	>7.0
7	+ 5	24	0.8	7.6 ± 2.3	12	2.1
8	-15	18	0.2	1.4 ± 0.7	12	0.4
9	-36	15	1.4	8 ± 4	?	?
10	-75	15	0.7	4 ± 2	?	?
11	-96	12	0.7	3.3 ± 1.0	17	0.6
12	-100	13	1.2	6 ± 3	26	0.8
13	-98	13	0.9	4.7 ± 1.4	15	1.0
14	-100	13	0.65	3.4 ± 1.0	15	0.7
15	-107	9	0.25	0.9 ± 0.5	9	0.3

Table 5-2

Mean Parameters for "Typical" Sgr B2 OH Clouds

Approximate Velocity (km/s)	+60	-100
Mean Velocity Dispersion (km/s)	22.5	12.9
Mean Peak Optical Depth	1.6	0.9
$\langle N_{OH}/T_s \rangle$ ($10^{15} cm^{-2} K^{-1}$)	16.	4.4
Mean Linear Diameter (pc)	15.	18.
$\langle n_{OH}/T_s \rangle$ ($10^{-4} cm^{-3} K^{-1}$)	3.8	0.8

The cloud sizes are approximately the same, but the velocity dispersion of the +60 clouds is nearly twice as large as for the -100 clouds. The mean optical depth for the +60 clouds is also greater, which two facts account for the large difference in column and space densities of OH between the two groups. In comparison, the Sgr A component I cloud resembles the Sgr B2 +60 features, while component II appears to be intermediate between the +60 and -100 values. The uncertainties in the component II parameters are substantial, however. The Sgr B2 clouds at velocities between these groups show a range of values for the tabulated parameters, so that classification is unclear. The most certain distinction is the correlation between algebraic sign of the velocity and the magnitude of the velocity dispersion, which we discussed above.

Excitation Temperature of the 1667 MHz Transition

The excitation temperature, T_s, of the 1667 MHz transition is an important quantity for two reasons. First, it is undoubtedly related

to the kinetic temperature of the gas itself. Secondly, if we can determine the value (or limits on the value) of T_s , then we can calculate the column and space densities of OH molecules from the quantities in Table 5-1. The relationship between the excitation temperature and the physical conditions (kinetic temperature, density, composition, and state of ionization) in the gas clouds, is a difficult problem. A detailed examination of this question is beyond the scope of this work; the reader is referred to papers by Rogers and Barrett (1968), Goss and Field (1968), and Goss (1968). We will, however, consider the basic constraints on the several processes which determine the ratio of populations in the upper and lower states.

The 1667 MHz OH transition is long-lived, with $A_{22}^{-1} = 1.30 \times 10^{10}$s. It would be expected that collisional deexcitation dominates the radiative process for fairly modest particle densities. If we denote by C_{22} the collisional deexcitation rate, then the excitation temperature of the line should equal the gas kinetic temperature provided

$$C_{22} >> A_{22} .$$

Calculation of C_{22} requires a knowledge of the important collision processes. Rogers and Barrett (1968) find that collision with ions is the most important process for HI regions with a neutral hydrogen atom density of 10 cm^{-3}. The clouds we are concerned with here have very much higher densities and consist mostly of molecular hydrogen, however. Solomon and Werner (1971) have shown that the fractional abundance of ions and electrons is very low for the probable density ranges within

these clouds. Assuming carbon is not ionized, they find that the fractional ionization of the gas at a density of $10^4 cm^{-3}$ and cosmic-ray ionization rate of $10^{-15} s^{-1}$ (Field, Goldsmith, and Habing 1969) is 10^{-5}. Thus, although OH-ion collisions have a large transition cross-section, the low abundance of charged particles makes the process negligible compared to collisions with neutrals. The neutral particles are almost all molecular hydrogen. Cross-sections for OH-H_2 collisions are not well known; if we assume a typical cross-section of $\sigma = 2 \times 10^{-15} cm^2$ (Solomon 1973), the condition for thermalizing the λ18 cm OH transition by collisions is

$$n_{H_2} >> \frac{A_{22}}{\sigma v} \quad .$$

At a kinetic temperature of 10K , this condition becomes $n_{H_2} >> 3\ cm^{-3}$. (Note that the next rotational level for OH is 84 cm^{-1} above the ground state, so at 10K , collisions to higher rotational levels are negligible.) For dense clouds, then, we should expect that the levels are in thermodynamic equilibrium with the gas.

This calculation assumes that the extinction due to the grains in the cloud is sufficiently large that radiative excitation by starlight is negligible. Goss (1968) has shown that excitation by multiple transitions between rotational levels is negligible compared to collisional transitions between the lambda-doublet levels and to radiative (λ18 cm) transitions. If the λ18 cm photons are trapped within the dense clouds, the excitation temperature will tend to approach the temperature of the radiation field. However, in the

clouds near the galactic center, optical depths in the 1667 MHz line are typically of order unity, and are probably not much larger than 3. Trapping of 18 cm photons is therefore not a significant process. Also, the large observed linewidths indicate mass motions within the clouds which will shift the OH transition frequency in one region with respect to photons emitted in other parts of the cloud, greatly reducing the size of the region in which trapping could occur.

The dust grains will have an important influence on the temperature of the gas, and hence on the excitation of the OH lines. Werner and Salpeter (1969) have solved equations of transfer for spherical dust and gas clouds, and obtain equilibrium values of $T \simeq 9 - 15K$. The grains provide effective shielding against photodissociation by visible and UV photons. Solomon and Wickramasinghe (1969) show that molecular hydrogen will be destroyed only in a thin outer shell around the dense cloud. Interior to this shell, the grains will cool to temperatures in the range of $4 - 6K$, sufficiently low to allow formation of H_2 on the grain surfaces. This temperature range is comparable to the kinetic temperature of dark clouds, as determined from OH line intensity ratios (Heiles 1969) and from CO emission observations by Solomon (1973), who argues that the similarity of the observed gas kinetic temperatures and the predicted grain temperatures means the two are in equilibrium. The presence of diatomic and polyatomic molecules will efficiently cool the gas, because such molecules radiate very effectively in the far infrared. Similarly, impurities in the grains will cause them to radiate well in that wavelength band (Hoyle and Wickramasinghe 1967). Since the heating rates of these dense clouds

are small because of shielding by the dust, while cooling rates of both gas and grains are large, temperatures in the range of 5 to 10K are entirely plausible. If the excitation temperature of the 1667 MHz OH line is in fact determined by collisions, then the value of T_s will be equal to the kinetic temperature of the gas, and so of the dust, too.

The observational results of this work indicate that the excitation temperature for most of the clouds is less than 10K . In spectra 19 through 22 of Figure 3-9, there is no evidence for strong emission features. These spectra are at positions well away from the bright continuum sources, but in the region where McGee (1970a) finds a large concentration of OH clouds. The presence of spectral features seems to indicate that there are indeed molecular clouds at these positions, although it is possible that the features are due to residual sidelobes. Interpreting the spectra in terms of absorption and emission, then, must be done with great caution. The broad galactic and isotropic background components, which are resolved out in these synthesis maps, contribute an estimated 7K brightness temperature, which should be added to the zero level of the spectra. The highest temperature of (apparent) emission is no greater than 3K . If we assume, as is likely that the clouds are optically thick, then the excitation temperature of the clouds is less than 10K, including the zero offset. This is a firm upper limit for T_s in the clouds in this region.

There are also what appear to be absorption lines in the spectrum which, for an assumed zero offset of 7K, sometimes have minimum

brightness temperatures of only 1 or 2K. (For example, consider spectrum 21 at -50 and +90 km/s.) The noise level and uncertainties in zero offset make the minimum temperatures very uncertain. The excitation temperature indicated by these apparent absorption lines must be less than the background continuum, so that $T_s(\text{min}) < 7K$ from our previous estimate. This temperature is comparable to those deduced by Heiles (1969) for several dark clouds. The apparent absorption lines could even be interpreted as "anomalous" absorption, similar to that found in the $\lambda 6$ cm line of formaldehyde. The uncertainty in the background brightness temperature and the possibility of systematic effects due to residual sidelobes make such a hypothesis very questionable, though. We can state with some confidence that the largest observed brightness temperatures in spectra 19 through 22 of Figure 3-9 set an upper limit of 10K on the value of T_s for this region.

The region of extended emission in the brightness temperature maps near +50 km/s for Sgr B2 may have a larger excitation temperature than this limit. Spectrum 23 of Figure 3-9 shows clear evidence of a broad emission feature with the peak at (45 ± 10) km/s and with a velocity half-width of (55 ± 10) km/s. The brightness maps show the feature as an extended object, at least 12 arcminutes long, lying between the sources G0.7-0.0 and G0.9+0.0. The peak velocity and linewidth are similar to those of the deep absorption line in the G0.7-0.0 spectra. In view of the large optical depths found for the Sgr B2 clouds, it is likely that the cloud in emission is also optically thick. Then the observed brightness temperature gives the excitation

temperature directly. We distinguish two extreme cases: either the cloud is in front of the continuum source, or the cloud is behind it. The continuum level is (50 ± 10)K. Then, for large optical depth, we have these limits:

$$(30 \pm 10)K < T_s < (80 \pm 10)K \ .$$

The fact that the emission appears in an extended region and in a large range of velocities shows that it is not due to a maser effect. The emission is apparently "normal", that is, thermal, although the population of the lambda-doublet levels may be disturbed from LTE, as is sometimes the case in dust clouds (Crutcher 1972). This observation is the first detection of normal OH emission in the galactic center region.

The values for the range of excitation temperature are large, but by no means unreasonable. Goss (1968) finds that for hydrogen densities greater than 100 cm^{-3}, the value of T_s depends only on kinetic temperature, since the transition is thermalized. Thus, the estimated limits on T_s imply that the gas temperature is between 30 and 80K, if the OH is optically thick. These temperatures are slightly higher than usually assumed for dense clouds, suggesting that the emission region may be more rarified than other molecular regions, and so more likely to be heated by either photons or energetic particles.

Evidence Relating to the Formation of Molecules

We can now combine the information in Tables 5-1 and 5-2 with the estimates for the value of T_s to obtain true column and space densities. If the upper limit of 10K for T_s is assumed, the values in Table 5-2 for "typical" clouds, yield:

$$\left.\begin{aligned} N_{OH} &= 1.6 \times 10^{17} cm^{-2} \\ n_{OH} &= 3.8 \times 10^{-3} cm^{-3} \end{aligned}\right\} \quad \text{for positive velocities}$$

$$\left.\begin{aligned} N_{OH} &= 4.4 \times 10^{16} cm^{-2} \\ n_{OH} &= 8 \times 10^{-4} cm^{-3} \end{aligned}\right\} \quad \text{for negative velocities}$$

The value of T_s is almost certainly not lower than 5K, so these densities could not be overestimated by more than a factor of two, though they are probably better than that. We want to compare these densities with theoretical predictions for the rate of formation of molecules.

The most detailed and thorough calculation of molecular formation rates to date is that by Herbst and Klemperer (1973). They have solved simultaneously the kinetic equations for 31 species of atoms and molecules using reactions and rates selected from a total of 100 possible reaction equations, of which only those believed to be most important in interstellar conditions were chosen. They argue that ion-molecule reactions are most important; their calculations are based on an ionization rate of $10^{-17} s^{-1}$ per hydrogen molecule, with the ionization produced by 100 MeV protons.

The solution of the reaction equations yields a value for the expected number density of OH as a function of molecular hydrogen density and of ionization rate. Herbst and Klemperer find that the OH density is completely independent of the H_2 density over a range $n_{H_2} = 10^4$ to $10^6 cm^{-3}$. However, the density of OH is strongly dependent

on the ionization rate. Their calculated concentrations of OH have these values:

Ionization rate (s^{-1})	10^{-17}	10^{-18}
$n_{OH}(cm^{-3})$	7×10^{-5}	7×10^{-6}

These results assume an oxygen-hydrogen abundance ratio of 4.4×10^{-4} by number (Dalgarno and McCray 1972). Herbst and Klemperer find, however, that increasing the value of O/H to 6.8×10^{-4} (Allen 1963) also increases the abundance of OH by approximately the same factor. In this case, for an ionization rate of $10^{-17}s^{-1}$, n_{OH} is $1 \times 10^{-4}cm^{-3}$, again independent of the molecular hydrogen density.

These predicted values are considerably lower than our estimated densities from the observations. For the positive-velocity clouds, the observed density is a factor of 50 larger than predicted by Herbst and Klemperer. For negative-velocity clouds, the theoretical value is a factor of ten too low. We emphasize that our observed values for n_{OH} are averages. Individual clouds show even higher densities.

The theoretical model, then, is in serious disagreement with observations. One cannot force agreement by reducing the value of T_s, since a factor of between 10 and 50 is required. The excitation temperature would have to be between 1.0 and 0.2K, an impossibly low value. The parameters of the model might be altered to fit the observations. Herbst and Klemperer have calculated only a few models but it appears that by substantially increasing the abundance of oxygen

and increasing the ionization rate, a better fit would result. One could argue that the rate of supernova explosions near the galactic center is larger than in the rest of the galaxy, so that heavy-element enrichment of the molecular clouds occurs through recycling of the remnant matter. The flux of 100 MeV cosmic rays near the galactic center could also be greater than in the solar neighborhood, thus increasing the ionization rate over the value used by Herbst and Klemperer. The set of equations they solve is coupled and nonlinear, though, so it is risky to predict the results of making large changes in these parameters without actually doing the calculation. The effects on concentrations of other molecular species must also be considered.

In summary, we have found that the molecular clouds are at least partly resolved by the synthesized beam. The observed large optical depths show that the angular sizes of those clouds cannot be significantly smaller than the beam area. The peak column densities, divided by T_s, of the Sgr A and Sgr B2 clouds have been calculated. The column densities are converted to spatial densities by assuming the cloud thickness is equal to its mean transverse diameter. The results for typical molecular clouds in Sgr B2 are summarized in Table 5-2.

The excitation temperature of the OH 1667 MHz transition is probably less than 10K, based on the data for a region away from the bright continuum sources. We also find, however, that there is an extended region of emission lying north of G0.7-0.0. The emission line implies that in this region the excitation temperature lies

between 30 and 80K, if the OH is optically thick. It is suggested that the molecular cloud is less dense than more typical clouds nearby.

If the value of T_s is assumed to be 10K, we find that the column and space densities of OH for the several clouds are much larger than predicted by the detailed theory of molecular formation proposed by Herbst and Klemperer (1973). It is suggested that their assumptions about physical conditions and elemental abundances may not be appropriate for clouds near the galactic center.

SUMMARY AND SUGGESTIONS FOR FUTURE WORK

We summarize briefly the principal results of this investigation, and suggest topics for future research.

The +40 km/s absorption in Sgr A arises from two separate components, both of which are interpreted to be molecular clouds in rapid rotation, based on the longitude-velocity dependence of the cloud centers. If the model of rigid-body rotation is assumed, the mass density required to bind each cloud is 1.0×10^{-19} g cm^{-3} for component I and 3×10^{-20} g cm^{-3} for the lower-velocity component II. Assuming diameters of 10 pc and 5 pc, respectively, the components have total masses of $4.6 \times 10^{6} M_{\odot}$ and $2 \times 10^{5} M_{\odot}$, if they are gravitationally bound. If they are not bound, the mass estimate is invalid, but the observed velocity gradient implies that the cloud lifetimes are short--on the order of a few million years or less. Observations of CO emission (Solomon, et al. (1972) also indicate that the clouds are very massive, favoring the interpretation that they are gravitationally bound. The observed linewidths imply turbulent motions on the order of 20 km/s within the clouds. The origin of these objects and their large radial velocity toward the galactic nucleus are not understood.

The negative-velocity absorption features in Sgr A agree, as far as comparison can be made, with the results of McGee (1970a). However, the clouds lie mostly away from the continuum source, so very little can be deduced about their sizes and other properties.

Some of the observed molecular features are explained by the simple kinematical models of Scoville (1972) and of Kaifu, et al. (1972);

additional intermediate-velocity clouds are also important, but not predicted by these models. The lower-velocity component II of the Sgr A +40 km/s feature, and cloud 5 seen against G0.5-0.0, are found at velocities not explained by one or two expanding and rotating rings. It appears that these models will not account for the detailed velocity structure of the gas clouds as determined by the present work. The more recent kinematical models involving a two-armed spiral structure may provide a more coherent picture of the gas motions. The data in this study, however, are too limited in galactic longitude to allow an adequate test.

The deep absorption line at +60 km/s in the spectrum of G0.7-0.0 is due to a group of at least four separate clouds, which form a ring about the continuum maximum. The deepest absorption peaks are not coincident with the continuum peak, but lie from 2 to 5 arcminutes to the side. We find that the cloud nearest the G0.7-0.0 continuum peak (cloud 1) agrees well in velocity with that of the HII region as determined by the H109α recombination line. The other three OH clouds, however, are at systematically lower velocities and have larger linewidths than cloud 1. The molecular clouds are almost certainly closely associated with the G0.7-0.0 HII region. It is suggested that the difference in velocities between the ionized gas and the molecular clouds is due to the pressure differences between the hot HII region and the cold, dense molecular clouds. The observed fragmentation of the molecular region into four clouds may be due to, or at least enhanced by, a Rayleigh-Taylor instability produced by the interaction of the two gas regions. This explanation is similar to that

proposed by Zuckerman (1973) to explain the velocity difference between the ionized and molecular regions of the Orion Nebula. The data are insufficient to construct a detailed model for Sgr B2, however.

The excitation temperature, T_s , is probably very low for most of the molecular clouds detected near the galactic center. We have set an upper limit, based on the maximum line temperature in regions away from the bright continuum sources, such that $T_s \leq 10K$ (if the OH is optically thick). This value is in agreement with theoretical expectations for the grain and gas temperatures of dense molecular regions. However, there is evidence for normal (i.e., non-maser) emission from an extended region north in declination from G0.7-0.0 at a velocity comparable to that of the deep +60 km/s absorption features. From the observed line temperature, and assuming that the OH is optically thick, we find that the limits on the excitation temperature are $30K \leq T_s \leq 80K$. If the 1667 MHz transition is thermalized, then these limits are not unreasonably large for the gas temperature. It is also possible that the levels may be disturbed from thermodynamic equilibrium, so that $T_{gas} \neq T_s$. The large angular size (12 arcminutes) of the emission region would then imply that the mechanism by which the level populations are disturbed is operative through a large volume of space.

In analyzing the physical properties of the 15 discrete Sgr B2 clouds and the two components of the Sgr A +40 km/s feature, we find that there is a clear division into two groups. Those clouds with

positive radial velocities have linewidths which are, on the average, about a factor of two larger than the clouds at negative velocities. The positive-velocity clouds also tend to have larger optical depths, and so also larger column densities. The mean value of N_{OH}/T_s for the four +60 km/s clouds in Sgr B2 is $1.6 \times 10^{16} cm^{-2} K^{-1}$, while for four -100 km/s clouds, the mean is $4.4 \times 10^{15} cm^{-2} K^{-1}$. If we assume that the excitation temperature is 10K, which is the upper limit estimated for regions well away from the continuum sources, then the derived space densities of OH molecules are $3.8 \times 10^{-3} cm^{-3}$ for positive-velocity clouds, and $8 \times 10^{-4} cm^{-3}$ for negative-velocity clouds. These values are much larger than predicted in the detailed calculations of Herbst and Klemperer (1973). We also note that the density of OH is not dependent on the H_2 density (most of the oxygen being in the form of carbon monoxide), so it is not possible to relate the derived OH densities to the total gas density. The density of OH is very sensitive to both the O/H abundance ratio and the ionization rate in the gas. It seems possible that the ionization rates and elemental abundances assumed by Herbst and Klemperer are not appropriate for the galactic center region.

The study of molecules at the galactic center has only just begun. Extensive investigation of other molecular lines with various techniques will be necessary to understand the kinematics, physical conditions, and chemical reactions. We suggest here a few possibly fruitful areas for further research.

(1) More extensive high-resolution mapping by single antennas. The λ2.6 mm CO survey work begun by Solomon, et al. (1972) has good

angular resolution, although so far the sampling of the galactic plane has been sparse (only 10 arcminutes). A detailed mapping of the dense clouds found in the present work would be useful. The ammonia inversion transition at λ12.5 mm also permits good angular resolution with a large telescope. The λ6 cm formaldehyde line could be studied with resolution comparable to the present work on a large instrument, such as the 210-foot antenna at Parkes or the 100-meter dish at Bonn. Observations such as these will allow a direct comparison of molecular abundances in the various dense clouds.

(2) It would be of interest to measure the spectrum of OH excited rotational states, such as the $^2\Pi_{3/2}$, J = 5/2, and the $^2\Pi_{1/2}$, J = 1/2 states. These lie at energies, E/k , of about 120K and 180K, respectively, above the ground state. Detections or limits on the optical depths of these lines would provide valuable information on the gas temperature. In particular, the J = 5/2 state will be rather well populated if the gas temperature is actually as large as 80K in the region of anomalous emission north of G0.7-0.0. Thus it would be of interest to search for excited-state OH emission away from the bright continuum sources.

(3) An absorption line study, similar to this work, in the λ21 cm hydrogen line is also important. Some unpublished results by the author indicate that the Sgr A +40 km/s absorption has a much greater HI optical depth than low-resolution single dish spectra show. The true abundance of HI is obviously an important parameter for theories of the formation of molecular hydrogen, and bears on the

question of grain and gas temperatures.

(4) If a multichannel cross-correlation receiver becomes available at OVRO, it would be possible to extend this study in both the 1665 and 1667 MHz lines in much less observing time than is necessary when the spectrum must be constructed from five settings of the IF filters. One could obtain improved resolution without a prohibitive amount of observation. The ratio of the line opacities could be studied in detail, allowing a more direct calculation of OH densities and hyperfine state populations.

These are only a few of the possibilities for further investigation. The galactic center is a region of such complexity that the scope of research into its nature appears to be almost unlimited.

REFERENCES

Allen, C. W. 1963, Astrophysical Quantities (London: Athlone Press).

Bolton, J. G., van Damme, K. J., Gardner, F. F., and Robinson, B. J. 1964, Nature, 201, 279.

Bracewell, R. N. 1958, Proc. I. R. E., 46, 97.

Cheung, A. C., Rank, D. M., Townes, C. H., Thornton, D. D., and Welch, W. J. 1968, Phys. Rev. Letters, 21, 1701.

Cheung, A. C., Rank, D. M., Townes, C. H., Knowles, S. H., and Sullivan, W. T., III 1969, Ap. J., 157, L13.

Christiansen, W. N., and Högbom, J. A. 1969, Radiotelescopes (Cambridge: University Press).

Crutcher, R. M. 1972, unpublished Ph.D. dissertation, University of California, Los Angeles.

Dalgarno, A., and McCray, R. A. 1972, Ann. Rev. Astr. and Ap., 10, 375.

Downes, D., and Maxwell, A. 1966, Ap. J., 146, 653.

Field, G. B., Goldsmith, D. W., and Habing, H. J. 1969, Ap. J., 155, L149.

Fomalont, E. B. 1973, Proc. IEEE, 61, 1211.

Fomalont, E. B., Wyndham, J. D., and Bartlett, J. F. 1967, A. J., 72, 445.

Fomalont, E. B., and Weliachew, L. 1973, Ap. J., 181, 781.

Gardner, F. F., and Whiteoak, J. B. 1972, Ap. Lett., 10, 171.

Goldreich, P., and Lynden-Bell, D. 1965, M.N.R.A.S., 130, 125.

Goldstein, S. J., Gundermann, E. J., Penzias, A. A., and Lilley, A. E. 1964, Nature, 203, 65.

Goss, W. M. 1968, Ap. J. Suppl., 15, 131.

Goss, W. M., and Field, G. B. 1968, Ap. J., 151, 177.

Greisen, E. W. 1973, unpublished Ph.D. dissertation, California Inst of Technology.

Heiles, C. 1969, Ap. J., 157, 123.

Herbst, E., and Klemperer, W. 1973, Ap. J., 185, 505.

Högbom, J. A. 1973, Astron. and Astrophys. Suppl., in press.

Hollenbach, D., and Salpeter, E. E. 1971, Ap. J., 163, 155.

Hoyle, F., and Wickramasinghe, N. C. 1967, Nature, 214, 969.

Kaifu, N., Kato, T., and Iguchi, T. 1972, Nature, 238, 105.

Keen, N. J. 1971, The Radio and Electronic Engineer, 41, 133.

Kerr, F. J., and Sandqvist, A. 1968, Ap. Lett., 2, 195.

Kerr, F. J., and Sandqvist, A. 1970, Ap. Lett., 5, 59.

Kellerman, K. I., and Pauliny-Toth, I. I. K. 1968, Ann. Rev. Astron. and Astrophys., 6, 417.

Kellerman, K. I., Pauliny-Toth, I. I. K., and Williams, P. J. S. 1969, Ap. J., 157, 1.

Kristian, J., and Sandage, A. 1970, Ap. J., 162, 391.

Kruit, P. C. van der 1970, Astron. and Astrophys., 4, 462.

Kruit, P. C. van der 1971, Astron. and Astrophys., 13, 405.

Lequeux, J. 1967, in Radio Astronomy and the Galactic System (I.A.U. Symposium No. 31), ed. H. van Woerden (London: Academic Press), p. 393.

McGee, R. X. 1970a, Austral. J. Phys., 23, 541.

McGee, R. X. 1970b, Austral. J. Phys. Ap. Suppl., No. 17.

Manchester, R. N., Goss, W. M., and Robinson, B. J. 1969, Ap. Lett., 4, 93.

Maxwell, A., and Taylor, J. H. 1968, Ap. Lett., 2, 191.

Moffet, A. T. 1962, Ap. J. Suppl., 7, 93.

Oort, J. H. 1968, in Galaxies and the Universe, ed. L. Woltjer (New York: Columbia University Press), p. 1.

Oort, J. H. 1971, in Nuclei of Galaxies, ed. D. J. K. O'Connell (Amsterdam: North-Holland Publishing Company), p. 321.

Palmer, P., and Zuckerman, B. 1967, Ap. J., 148, 727.

Penzias, A. A., Jefferts, K. B., and Wilson, R. W. 1971, Ap. J., 165, 229.

Radford, H. E. 1964, Phys. Rev. Letters, 13, 534.

Raimond, E., and Eliasson, B. 1969, Ap. J., 155, 817.

Rank, D. M., Townes, C. H., and Welch, W. J. 1971, Science, 174, 1083.

Read, R. B. 1963, Ap. J., 138, 1.

Reifenstein, E. C., III. Wilson, T. L., Burke, B. F., Mezger, P. G., and Altenhoff, W. J. 1970, Astron. and Astrophys., 4, 357.

Riegel, K. W. 1966, unpublished Ph.D. dissertation, University of Maryland.

Robinson, B. J., Gardner, F. F., van Damme, K. J., and Bolton, J. G. 1964, Nature, 202, 989.

Robinson, B. J., and McGee, R. X. 1970, Austral. J. Phys., 23, 405.

Rogers, A. E., and Barrett, A. H. 1968, Ap. J., 151, 163.

Rougoor, G. W. 1964, B. A. N., 17, 381.

Sanders, R. H., Scoville, N. Z., and Spiegel, E. A. 1972, Comments on Ap. and Space Sci., 4, 15.

Sandqvist, A. 1970, A. J., 75, 135.

Sandqvist, A. 1971, unpublished Ph.D. dissertation, University of Maryland.

Sandqvist, A. 1973, Astron. and Astrophys. Suppl., 9, 391.

Scoville, N. Z. 1972, Ap. J., 175, L127.

Scoville, N. Z. 1973, in preparation.

Scoville, N. Z., Solomon, P. M., and Thaddeus, P. 1972, Ap. J., 172, 335.

Scoville, N. Z., Solomon, P. M., and Jefferts, K. B. 1973, in preparation.

Shostak, G. S. 1972, unpublished Ph.D. dissertation, California Institute of Technology.

Simonson, S. C., III, and Mader, G. L. 1973, Astron. and Astrophys., 27, 337.

Solomon, P. M. 1973, in Molecules in the Galactic Environment, ed. M. A. Gordon and L. E. Snyder (New York: John Wiley and Sons), p. 156.

Solomon, P. M., and Wickramasinghe, N. C. 1969, Ap. J., 158, 449.

Solomon, P. M., and Werner, M. W. 1971, Ap. J., 165, 41.

Solomon, P. M., Scoville, N. Z., Penzias, A. A., Wilson, R. W., and Jefferts, K. B. 1972, Ap. J., 178, 125.

Spitzer, L. 1968, Diffuse Matter in Space (New York: Interscience Publishers).

Swenson, G. W., Jr. 1969, Ann. Rev. Astron. and Astrophys., 7, 353.

Turner, B. E. 1966, Nature, 212, 184.

Turner, B. E. 1972, Ap. J., 171, 503.

Turner, B. E., and Heiles, C. 1971, Ap. J., 170, 453.

Wade, C. M. 1970, Ap. J., 162, 381.

Weinreb, S., Barrett, A. H., Meeks, M. L., and Henry, J. C. 1963, Nature, 200, 829.

Werner, M. W., and Salpeter, E. E. 1969, M.N.R.A.S., 145, 249.

Wilson, O. C., Munch, G., Flather, E. M., and Coffeen, M. F. 1959, Ap. J. Suppl., 4, 199.

Zuckerman, B. 1973, Ap. J., 183, 863.

Zuckerman, B., Buhl, D., Palmer, P., and Snyder, L. 1970, Ap. J., 160, 485.